Relative roles of plume and coastal forcing on exchange flow variability of a glacial fjord

Robert Manuel Sanchez[1], Fiamma Straneo[2], Kenneth G. Hughes[3], Philip Barbour[3], and Emily L. Shroyer[3]

[1]UC San Diego
[2]UCSD
[3]Oregon State University

November 8, 2023

Abstract

Glacial fjord circulation determines the import of oceanic heat to the Greenland Ice Sheet and the export of ice sheet meltwater to the ocean. However, limited observations and the presence of both glacial and coastal forcing - such as coastal-trapped waves - make uncovering the physical mechanisms controlling fjord-shelf exchange difficult. Here we use multi-year, high-resolution, realistically forced numerical simulations of Sermilik Fjord in southeast Greenland to evaluate the exchange flow. We compare models, with and without a plume, to differentiate between the exchange flow driven by shelf variability and that driven by subglacial discharge. We use the Total Exchange Flow framework to quantify the exchange volume fluxes. We find that a decline in offshore wind stress from January through July drives a seasonal reversal in the exchange flow increasing the presence of warm Atlantic Water at depth, that the exchange flux in the summer doubles with the inclusion of glacial plumes, and that the plume-driven circulation is more effective at renewal with a flushing time 1/3 that of the shelf-driven circulation near the fjord head.

The views presented herein are those of the writer and do not necessarily represent the views of DoD or its components.

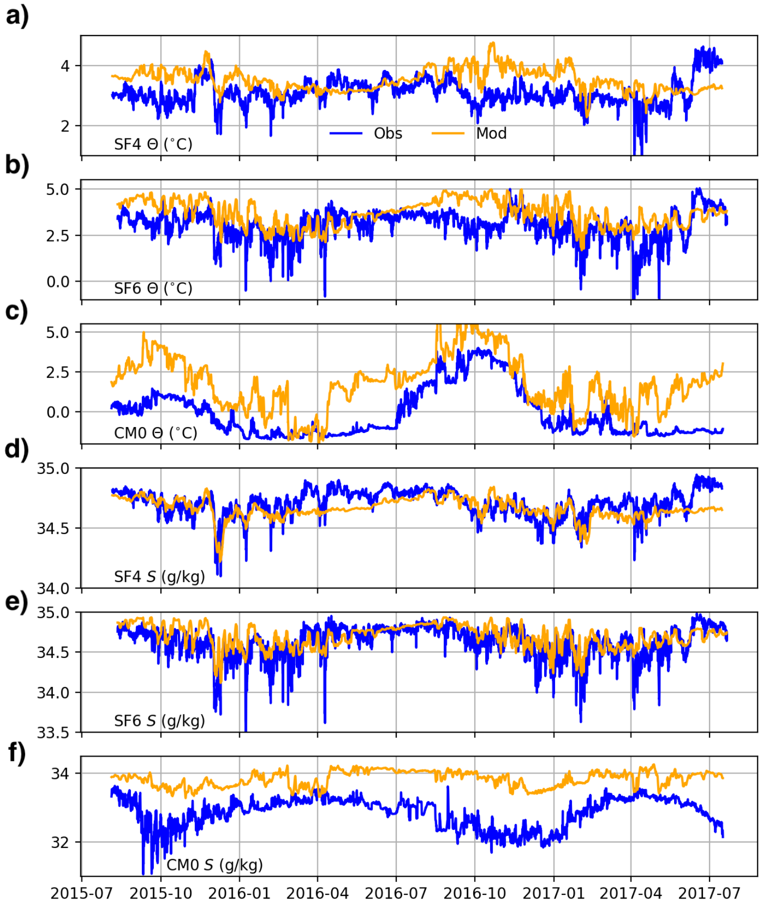
a)
b)
c)
d)
e)
f)
SF4 Θ (°C)
Obs
Mod
SF6 Θ (°C)
CM0 Θ (°C)
SF4 S (g/kg)
SF6 S (g/kg)
CM0 S (g/kg)
2015-07
2015-10
2016-01
2016-04
2016-07
2016-10
2017-01
2017-04
2017-07

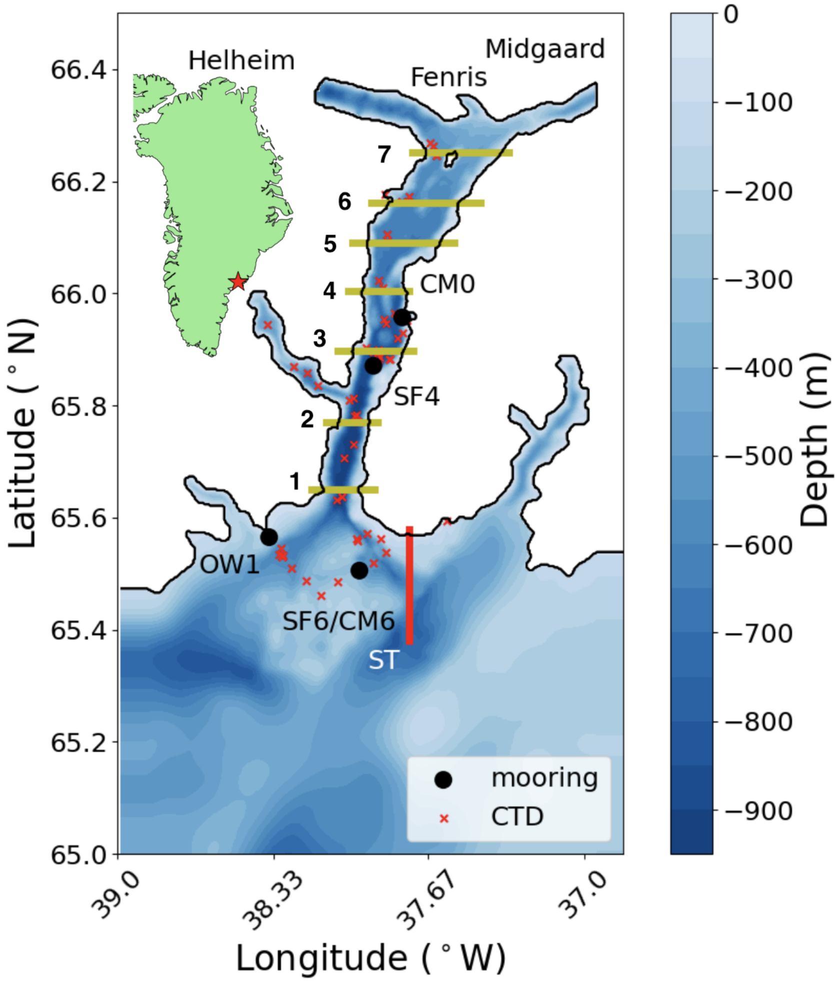

Helheim
Midgaard
Fenris
66.4
66.2
66.0
65.8
65.6
65.4
65.2
65.0
Latitude (° N)
7
6
5
4
3
2
1
CM0
SF4
OW1
SF6/CM6
ST
mooring
CTD
39.0
38.33
37.67
37.0
Longitude (° W)
0
−100
−200
−300
−400
−500
−600
−700
−800
−900
Depth (m)

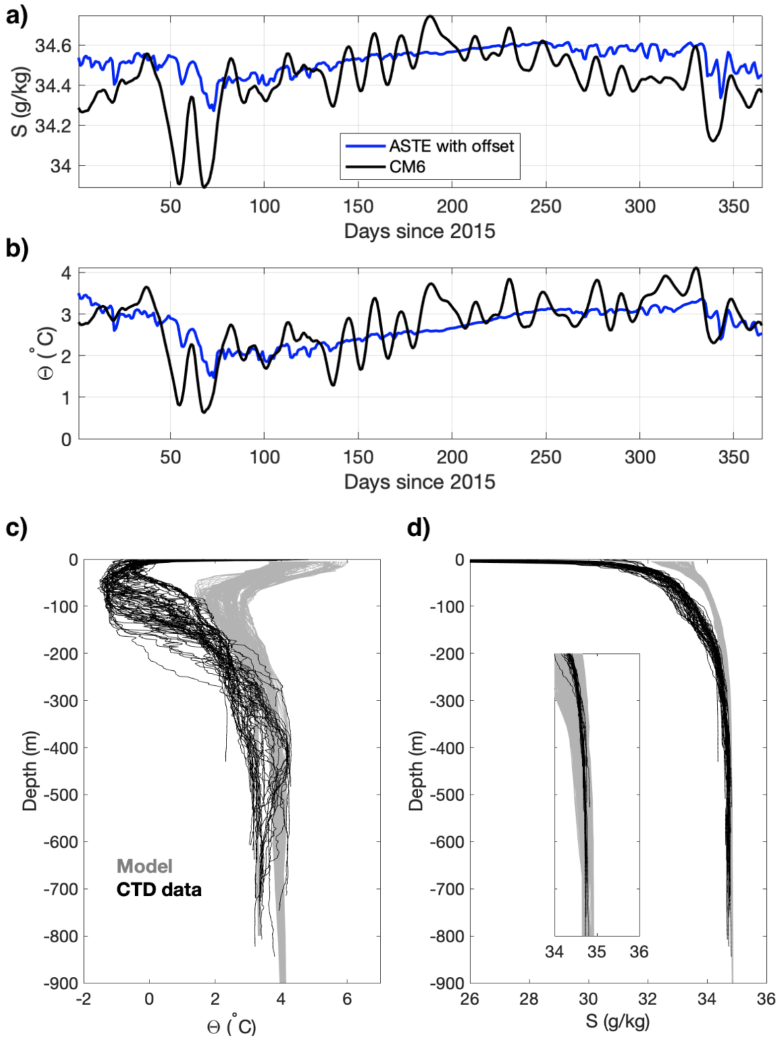
a)
S (g/kg)
ASTE with offset
CM6
Days since 2015
b)
Θ (°C)
Days since 2015
c)
Depth (m)
Model
CTD data
Θ (°C)
d)
Depth (m)
S (g/kg)

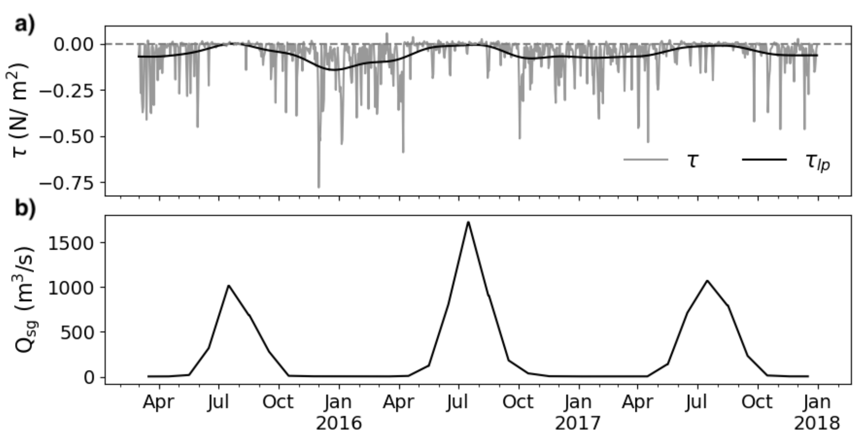
a)
τ (N/ m²)
τ
τ_lp
b)
Q_sg (m³/s)
Apr
Jul
Oct
Jan
2016
Apr
Jul
Oct
Jan
2017
Apr
Jul
Oct
Jan
2018

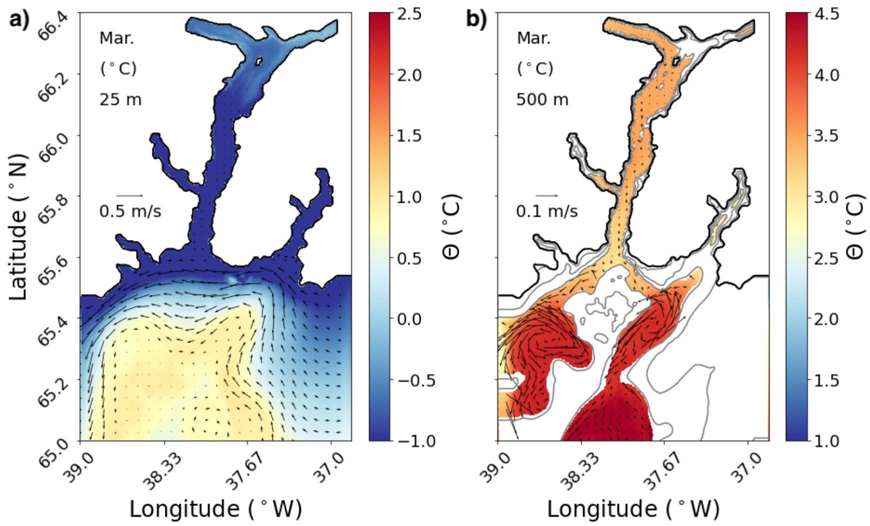

a)
Mar.
(°C)
25 m
0.5 m/s
Latitude (°N)
Longitude (°W)
Θ (°C)
b)
Mar.
(°C)
500 m
0.1 m/s
Longitude (°W)
Θ (°C)

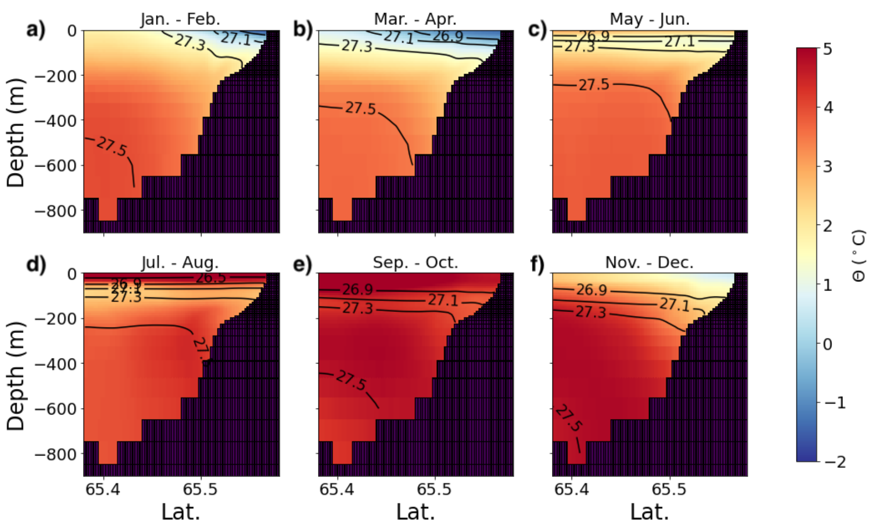

a) Jan. - Feb.
b) Mar. - Apr.
c) May - Jun.
d) Jul. - Aug.
e) Sep. - Oct.
f) Nov. - Dec.
Depth (m)
Lat.
Θ (°C)

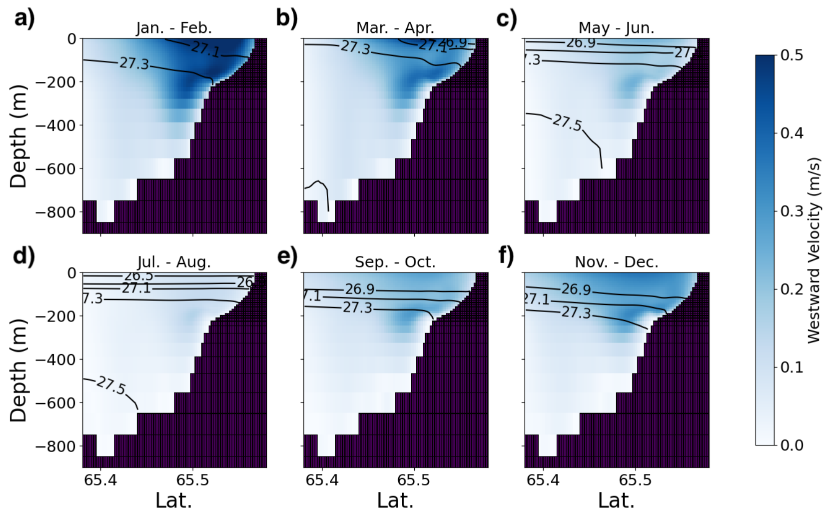
a)
Jan. - Feb.
b)
Mar. - Apr.
c)
May - Jun.
d)
Jul. - Aug.
e)
Sep. - Oct.
f)
Nov. - Dec.
Depth (m)
Lat.
Westward Velocity (m/s)

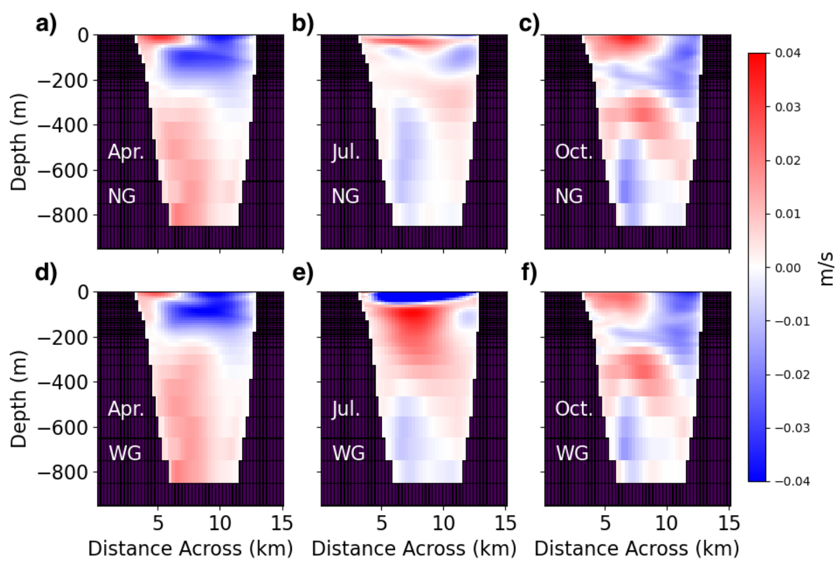
a)
b)
c)
d)
e)
f)
Apr.
NG
Jul.
NG
Oct.
NG
Apr.
WG
Jul.
WG
Oct.
WG
Depth (m)
Distance Across (km)
m/s

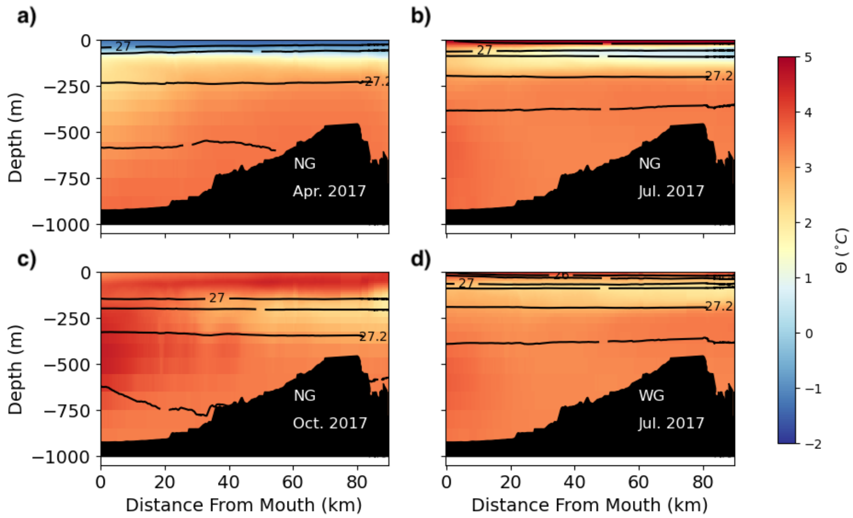
a)
b)
c)
d)
Depth (m)
Distance From Mouth (km)
NG
Apr. 2017
NG
Jul. 2017
NG
Oct. 2017
WG
Jul. 2017
27
27.2
θ (°C)

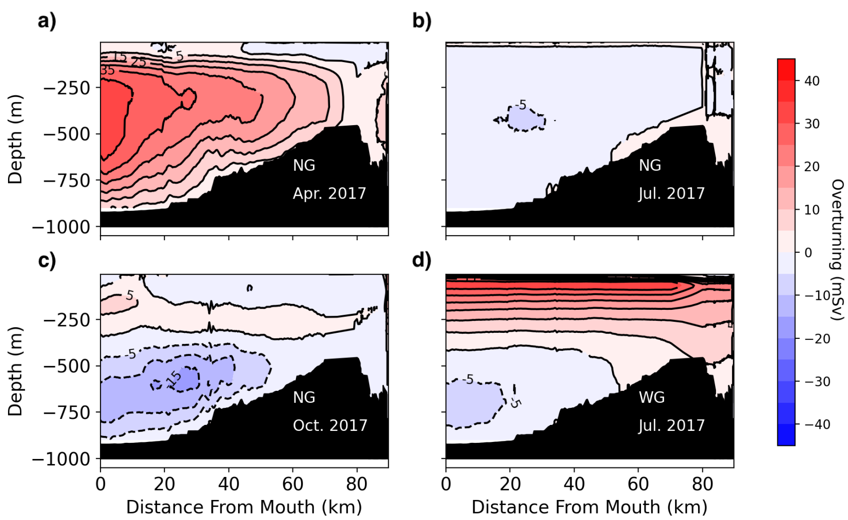
a)
b)
c)
d)
Depth (m)
Distance From Mouth (km)
NG
Apr. 2017
NG
Jul. 2017
NG
Oct. 2017
WG
Jul. 2017
Overturning (mSv)

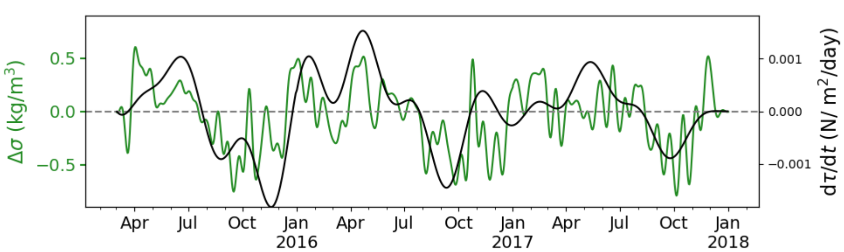
Δσ (kg/m³)
dτ/dt (N/ m²/day)
Apr
Jul
Oct
Jan
2016
2017
2018

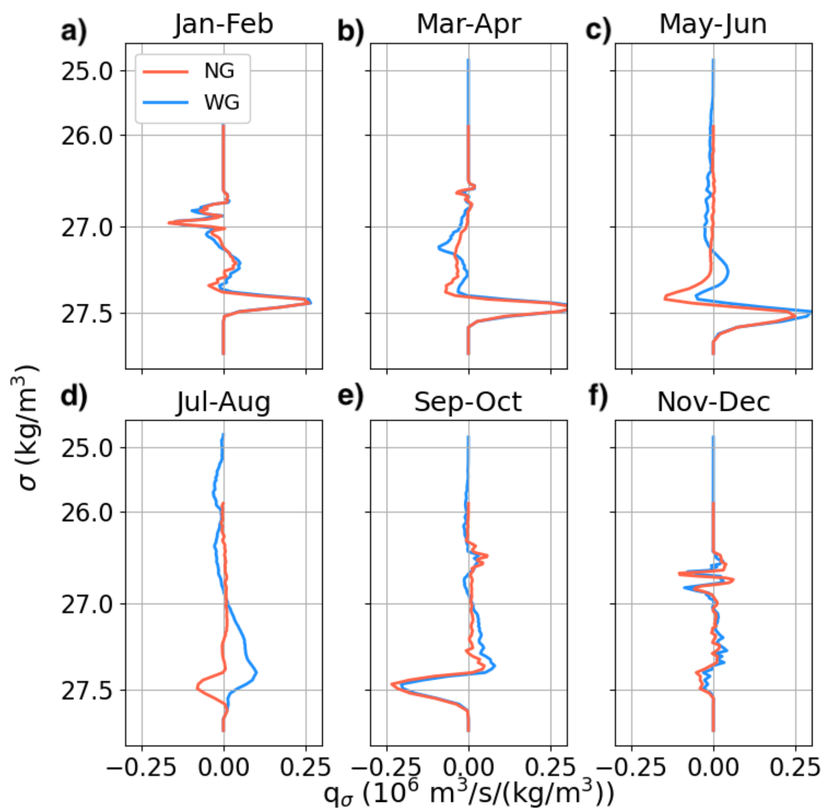
a)
Jan-Feb
b)
Mar-Apr
c)
May-Jun
d)
Jul-Aug
e)
Sep-Oct
f)
Nov-Dec
NG
WG
σ (kg/m3)
qσ (10^6 m3/s/(kg/m3))

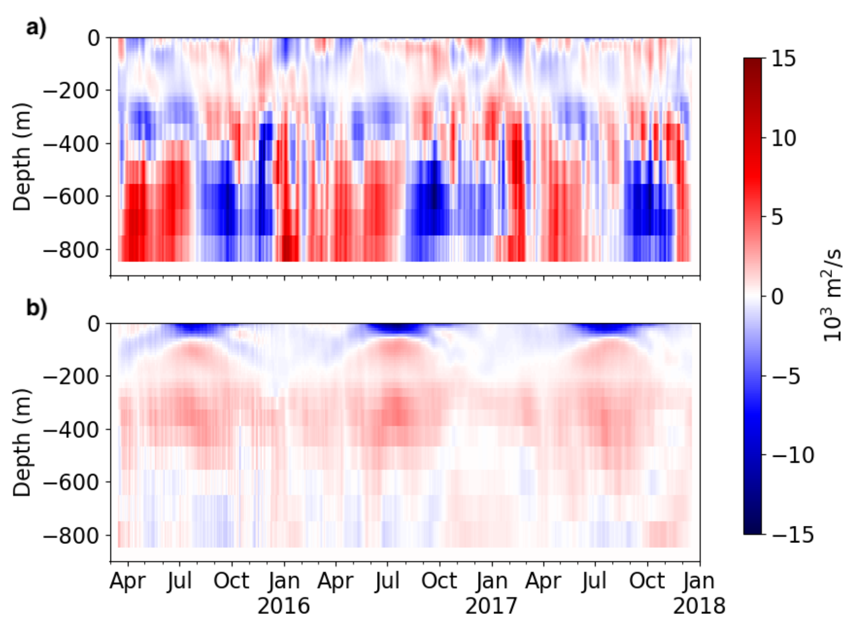
a)
b)
Depth (m)
10^3 m^2/s
Apr Jul Oct Jan Apr Jul Oct Jan Apr Jul Oct Jan
2016
2017
2018

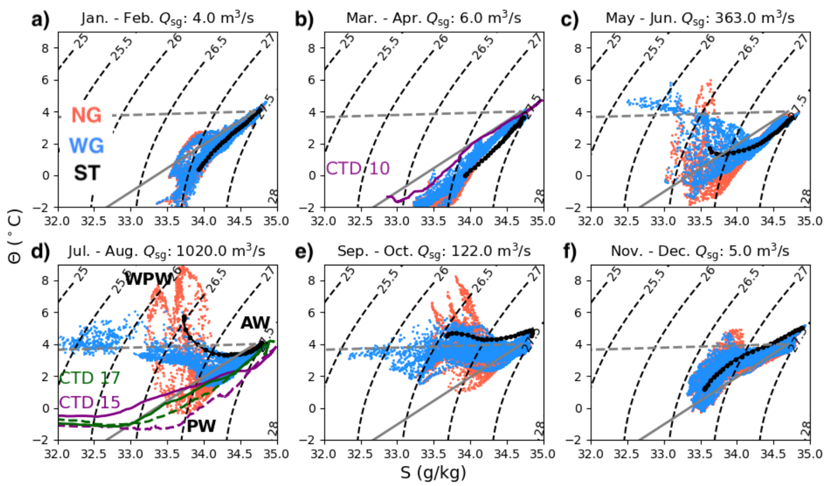
a)
Jan. - Feb. Q_{sg}: 4.0 m^3/s
NG
WG
ST
b)
Mar. - Apr. Q_{sg}: 6.0 m^3/s
CTD 10
c)
May - Jun. Q_{sg}: 363.0 m^3/s
d)
Jul. - Aug. Q_{sg}: 1020.0 m^3/s
WPW
AW
CTD 17
CTD 15
PW
e)
Sep. - Oct. Q_{sg}: 122.0 m^3/s
f)
Nov. - Dec. Q_{sg}: 5.0 m^3/s
Θ ($^\circ$C)
S (g/kg)

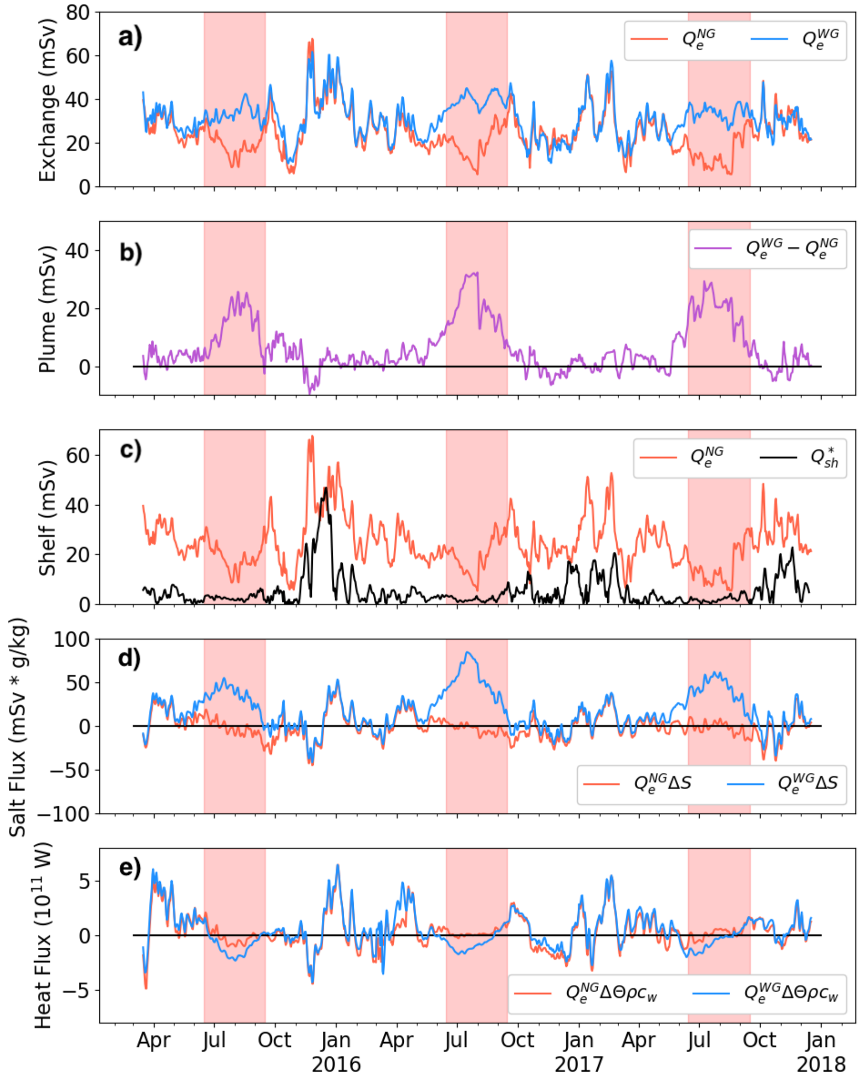
a)
Exchange (mSv)
Q_e^{NG}
Q_e^{WG}
b)
Plume (mSv)
$Q_e^{WG} - Q_e^{NG}$
c)
Shelf (mSv)
Q_e^{NG}
Q_{sh}^*
d)
Salt Flux (mSv * g/kg)
$Q_e^{NG}\Delta S$
$Q_e^{WG}\Delta S$
e)
Heat Flux (10^{11} W)
$Q_e^{NG}\Delta\Theta\rho c_w$
$Q_e^{WG}\Delta\Theta\rho c_w$
Apr Jul Oct Jan Apr Jul Oct Jan Apr Jul Oct Jan
2016
2017
2018

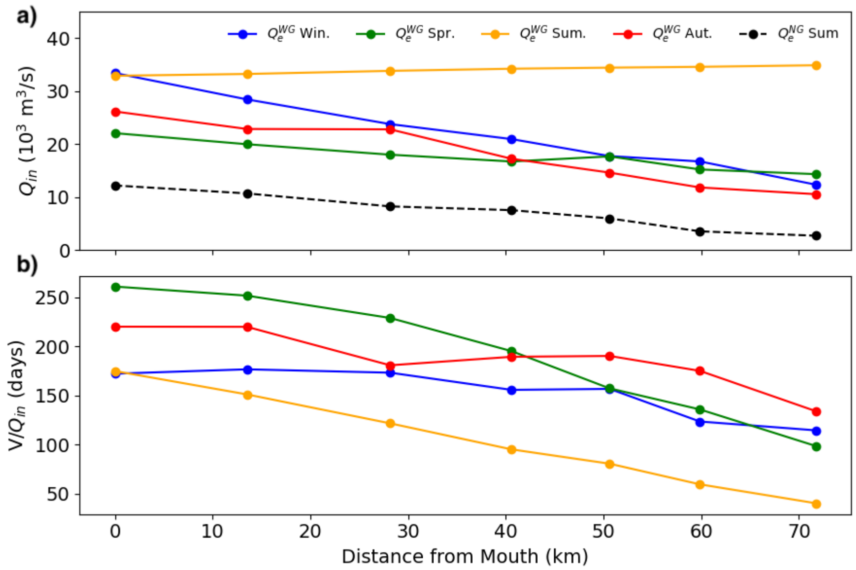
a)
b)
Q_e^{WG} Win.
Q_e^{WG} Spr.
Q_e^{WG} Sum.
Q_e^{WG} Aut.
Q_e^{NG} Sum
Q_{in} (10^3 m^3/s)
V/Q_{in} (days)
Distance from Mouth (km)
0
10
20
30
40
50
60
70
100
150
200
250

Relative roles of plume and coastal forcing on exchange flow variability of a glacial fjord

Robert Sanchez[1], Fiammetta Straneo[1], Kenneth Hughes[2], Philip Barbour[2], Emily Shroyer[2,3]

[1]Scripps Institution of Oceanography, UC San Diego, San Diego, CA, USA
[2]College of Earth, Ocean, and Atmospheric Sciences, Oregon State University, Corvallis, OR, USA
[3]Office of Naval Research

Key Points:

- We present a set of realistically forced, multi-year numerical simulations of Sermilik Fjord in Greenland.
- The shelf-driven circulation is tied to along-shelf wind stress and drives a reversal in the exchange flow as winds intensify in September.
- The plume-driven circulation is more effective at renewal with a flushing time 1/3 that of the shelf-driven circulation near the fjord head.

Corresponding author: R. Sanchez, `rmsanche@ucsd.edu`

Abstract

Glacial fjord circulation determines the import of oceanic heat to the Greenland Ice Sheet and the export of ice sheet meltwater to the ocean. However, limited observations and the presence of both glacial and coastal forcing - such as coastal-trapped waves - make uncovering the physical mechanisms controlling fjord-shelf exchange difficult. Here we use multi-year, high-resolution, realistically forced numerical simulations of Sermilik Fjord in southeast Greenland to evaluate the exchange flow. We compare models, with and without a plume, to differentiate between the exchange flow driven by shelf variability and that driven by subglacial discharge. We use the Total Exchange Flow framework to quantify the exchange volume fluxes. We find that a decline in offshore wind stress from January through July drives a seasonal reversal in the exchange flow increasing the presence of warm Atlantic Water at depth, that the exchange flux in the summer doubles with the inclusion of glacial plumes, and that the plume-driven circulation is more effective at renewal with a flushing time 1/3 that of the shelf-driven circulation near the fjord head.

Plain Language Summary

Glacial fjords connect the Greenland Ice Sheet and the ocean, and the circulation within fjords plays a crucial role in the exchange of heat and freshwater between the two. Glacial fjord circulation is driven, in part, by ice sheet surface melt which enters the fjord at the sea bed after falling through cracks in the ice. The meltwater's buoyancy causes it to rise as a plume, growing in volume through mixing with ocean water, before leaving the fjord closer to the surface. Fjord circulation is also influenced by the passing of storms close to the coast which can trigger pressure disturbances that propagate into the fjord as waves with periods of several days. We conducted two simulations of Sermilik Fjord in southeast Greenland to isolate and study the effects of coastal winds and plumes on fjord circulation. Our simulations reveal that as winds along the east coast of Greenland weaken, more warm water of subtropical origin can enter the fjord. We also find that in the summer the strength of the fjord circulation doubles in a model run with plumes versus a run without. These results increase our understanding of how fjord circulation responds to competing and time-varying external forcing.

1 Introduction

Glacial fjords connect the Greenland Ice Sheet (GrIS) with the continental shelf, and fjord dynamics are responsible for the import of oceanic heat to the GrIS and the export of ice sheet meltwater to the ocean. The fjord exchange of heat and salt at the fjord mouth, along with vertical mixing within the fjord, modifies water properties including ocean heat content and stratification, and ultimately sets the boundary conditions for ice-ocean interactions (Straneo & Cenedese, 2015; Holland et al., 2008; Straneo et al., 2011; Shroyer et al., 2017; Mortensen et al., 2018; Hager et al., 2022). Understanding fjord-shelf exchange is therefore crucial to predicting the impact of the ocean on marine-terminating glaciers and the consequences of exported freshwater on regional circulation and ecosystems (Hopwood et al., 2020; Straneo & Heimbach, 2013; Rysgaard et al., 2003).

Numerous drivers influence glacial fjord exchange on hourly to seasonal timescales. At the fjord mouth, circulation can be influenced by tides (Mortensen et al., 2011), external water mass variability (Schaffer et al., 2020), continental shelf wind variability (Jackson et al., 2014) and coastal-trapped waves (Gelderloos et al., 2021). Within the fjord, circulation is modified by mixing (Hager et al., 2022), internal waves (Inall et al., 2015), surface heat fluxes (Mortensen et al., 2011), local winds (Moffat, 2014), and iceberg melt (Davison et al., 2020). At the glacial boundary, or fjord head, additional forcing comes from surface runoff (Stuart-Lee et al., 2021), subglacial discharge (Carroll et al., 2015), and submarine melting of the terminus (Zhao, Stewart, & McWilliams, 2022). However, untangling the individual role of these drivers is challenging because many of the effects are cumulative and difficult to isolate with limited observations (Straneo et al., 2019). In this study, we will focus on the relative roles of plume forcing and shelf forcing (e.g., winds, coastal-trapped waves) on fjord circulation, as these are the two dominant forcing mechanisms of fjords in southeast Greenland (Jackson et al., 2014; Jackson & Straneo, 2016; Fraser & Inall, 2018; Gelderloos et al., 2022).

Glacial fjords undergo substantial seasonal variability in both shelf and glacial forcing that complicates diagnosing drivers of fjord circulation (Mortensen et al., 2014; Jackson & Straneo, 2016; Hager et al., 2022). Glacial forcing from submarine melting and ice sheet meltwater runoff is strongest in summer, but shelf-forcing seasonality is dependent on factors such as sea ice, boundary currents and wind forcing which can vary regionally (Carroll et al., 2018; Gelderloos et al., 2017; Gladish, Holland, & Lee, 2014). Observations are biased towards the summer and away from ice-congested areas, limiting comparisons between glacial-driven circulation and shelf-driven circulation. Consequently, we lack a deep understanding of the relative role of the shelf-driven circulation vs. plume-driven circulation in setting fjord properties seasonally and how these circulation modes vary along fjord.

Models of glacial fjords have been a useful tool in isolating different forcing mechanisms and overcoming data limitations. Very high-resolution (< 10 m) models have brought insight into the dynamics of subglacial discharge plumes (e.g., Xu et al., 2012; Sciascia et al., 2013; Kimura et al., 2014; Carroll et al., 2015; Ezhova et al., 2017) and led to plume representation into larger fjord models (T. Cowton et al., 2015; Jenkins, 2011). Fjord-scale models have allowed for an assessment of the impact of along-fjord winds, along-shelf winds and shelf forcing on fjord dynamics (Sundfjord et al., 2017; Jackson et al., 2018; Fraser & Inall, 2018), of iceberg melt on water mass transformation (Davison et al., 2020; Kajanto et al., 2023), of sea ice retreat on fjord circulation (Shroyer et al., 2017), and of fjord geometry, including ice mélange, on fjord renewal (Gladish, Holland, Rosing-Asvid, et al., 2014; Carroll et al., 2017; Zhao et al., 2021; Hughes, 2022). While these models have significantly improved our understanding of glacial fjord processes, they are usually run on idealized bathymetry or with idealized forcing limiting any comparison with observations. Realistic models, evaluated against observations, are needed to identify the time-integrated response of fjords to seasonally-varying forcing and to generate the complex circulation patterns seen in observations.

We use a high-resolution, realistic model of Sermilik Fjord, in southeast Greenland, forced by a wind-reanalysis product and boundary conditions from a larger pan-Arctic state estimate, to differentiate between the shelf-driven and subglacial discharge-driven exchange flow. Comparison with observations shows that the model reproduces the relevant dynamics over multiple years and through seasonal transitions. We split the results into three sections focused on the seasonality of the shelf-driven circulation (Section 4), the plume-driven circulation (Section 5) and a comparison between the two in the context of the exchange flow (Section 6). We find the seasonality of the along-shelf winds drives reversals in the circulation, the exchange flow is primarily plume-driven during the summer, and the plume-driven circulation is more effective at renewal than the shelf-driven circulation. Understanding the response of fjord-shelf exchange to simultaneous external and internal forcing is a critical step towards improved representation of ice-ocean interactions in climate models.

2 Background on Sermilik Fjord System

Sermilik Fjord (SF) is part of a large glacial fjord system in southeast Greenland (Fig. 1, inset map). The fjord varies in width from 5 – 10 km, is 550 – 900 m deep, and is about 80 km long before branching into three fjords connecting to Helheim, Fenris and

Midgaard glacier from west to east (Fig. 1). Midgaard Glacier has experienced the greatest cumulative loss of the three glaciers over the past 40 years (138 ± 5 Gt, Mouginot et al., 2019). However, Helheim Glacier is currently one of the largest outlet glaciers in Greenland (35 Gt/yr, Mankoff et al., 2020; Enderlin et al., 2014) and saw a rapid acceleration and thinning in the 2000s (Howat et al., 2005; Luckman et al., 2006). Increased submarine melting due to relatively warm water at depth and circulation enhanced by ice sheet runoff has been proposed as a likely trigger for retreat (Straneo et al., 2011; Holland et al., 2008; Wood et al., 2018, 2021; Khazendar et al., 2019; Slater & Straneo, 2022; Jackson et al., 2022).

The water masses present in the fjord determine the heat available for melting. SF has a deep sill (500 m) that is far from the mouth allowing significant water column exchange with the shelf (Straneo et al., 2010; Jackson et al., 2014). As a result, the water masses in the fjord broadly match those found on the adjacent shelf and are steered into SF through Sermilik Trough, a deep trough that cuts across the eastern part of shelf before running parallel to the coastline (Fig 1; Straneo et al., 2011; Harden et al., 2014; Snow et al., 2021). During the winter, SF is dominated by two water masses: cold and fresh Polar Water (PW) of Arctic origin and a deep, relatively warm and salty water of Atlantic origin (AW) (Sup. Fig. 1). During the summer, a third water mass, Warm Polar Water (WPW), is formed on the shelf from surface warming of PW and intrudes into fjords. Mixing across the shelf and trough determine the relative volumes of these water masses within the fjord (Snow et al., 2021; Harden et al., 2014).

In addition to shelf water masses, two types of meltwater are released into the fjord and affect fjord circulation and water properties. Submarine meltwater forms locally when icebergs and glaciers melt in the ocean, and subglacial discharge forms through surface melting of the ice sheet and enters the fjord at depth. Subglacial discharge generates a turbulent buoyant plume which drives an overturning circulation, upwells warm and salty AW into shallower depths and enhances submarine melting (Carroll et al., 2015; Beaird et al., 2018; Jackson et al., 2022; Slater et al., 2022; Slater & Straneo, 2022). The upwelled AW is many times the volume of the original subglacial discharge flux and can displace PW that was previously near the head of the fjord (Mankoff et al., 2016; Beaird et al., 2018). Therefore, both glacial and shelf processes influence the amount of AW (and heat) within the fjord.

Observations have shown that the circulation in SF is strongly influenced by shelf forcing (Straneo et al., 2010; Jackson et al., 2014; Snow et al., 2021). Shelf winds primarily flow southwestward and parallel to the coast resulting in downwelling conditions that generate large pycnocline displacements. These displacements create a density gradient within the fjord initiating baroclinic circulation with shallow inflow and deep outflow (Klinck et al., 1981; Aure et al., 1996; Jackson et al., 2014). As the pycnocline relaxes, the circulation reverses. Many of these events are correlated with observable pulses within Sermilik Fjord and are associated with 3–7 day periods, 40 cm/s speed and large heat and salt fluxes (Straneo et al., 2010; Jackson et al., 2014). The fjord heat content is dominated by pycnocline fluctuations which change the relative abundance of AW and PW and can obscure the influence of glacial forcing (Jackson & Straneo, 2016; Sanchez et al., 2021). These fluctuations have been linked with coastal-trapped waves (Fraser & Inall, 2018; Jackson et al., 2018).

As described above, subglacial discharge can initiate plumes at the heads of glacial fjords. Plumes drive an overturning circulation which enhances background melting (Slater et al., 2018; Jackson et al., 2020; Zhao, Stewart, & McWilliams, 2022; Zhao, Stewart, McWilliams, Fenty, & Rignot, 2022). The outflowing plume volume flux is primarily composed of ambient water entrained within the plume as it rises (Mankoff et al., 2016), and the plume is a significant source of water mass transformation. The outflowing plumes can interact with nearby bathymetry and drive recirculation in the fjord (Slater et al., 2018; Zhao, Stewart, & McWilliams, 2022). Thus, the influence of the plume-driven circulation on fjord-shelf exchange is a function of both subglacial discharge flux and fjord geometry.

Previous simulations of Sermilik Fjord (or idealized versions) have focused on coastal-trapped waves (Jackson et al., 2018; Gelderloos et al., 2022), subglacial discharge plumes (Sciascia et al., 2013), the impact of icebergs (Davison et al., 2020) and standing eddies (Zhao, Stewart, McWilliams, Fenty, & Rignot, 2022). However none of these studies involved the use of a full 3-dimensional model with realistic bathymetry and time-varying realistic forcing. Most of the previous models were run to steady-state and examined the fjord response to the input of glacial meltwater. Therefore, they could not capture seasonal transitions and the time-integrated response of fjord properties to external forcing.

3 Model Setup and Forcing

We ran nearly three-year simulations (2015 – 2017) of a regional model of Sermilik Fjord and its adjacent shelf (Fig. 1) using the hydrostatic-configuration of the MITgcm (Marshall et al., 1997; Adcroft et al., 2004). The model domain is 360 by 640 cells with an isotropic horizontal resolution of 280 m by 280 m. The model was configured with 32 vertical levels varying from 10-m resolution in the upper 200 m to 100-m resolution at 950 m depth. Model bathymetry is based on BedMachine v3 (Morlighem et al., 2017). The maximum depth within SF was 920 m (Fig. 1). Advection of temperature and salinity uses a third-order flux limiter scheme. The standard time step for the model was 60 s but reduced occasionally for model stability. Output snapshots are saved every three hours.

The model was configured with a nonlinear equation of state following Jackett and Mcdougall (1995). Mixing is parameterized using the KPP vertical mixing scheme (Large et al., 1994) with a background viscosity of 10^{-4} m^2 s^{-1} and diffusivity for temperature and salinity of 10^{-5} m^2 s^{-1} in the vertical. In the horizontal, the set-up used a non-dimensional harmonic viscosity of 0.01, which equates to approximately 3 m^2 s^{-1} for the isotropic configuration, modified by a non-dimensional Smagnoinsky scheme with coefficient 3 following Griffies and Hallberg (2000). A quadratic drag with coefficient 2×10^{-3} was applied at the bottom.

Simulation initialization and boundary forcing is taken from the Arctic Subpolar Gyre State Estimate "ASTE" (Nguyen et al., 2021). Initial temperature, salinity and velocity fields were generated from a spin-up simulation of three months in which the boundary forcing was held steady and no surface forcing was applied. On each of the three boundaries on the shelf, there are sponge regions that are 20 grid cells wide in which T, S, U, and V are relaxed to the ASTE values with time scales of 3 hours on the outer edges and 30 hours on the inner edges. Boundary fields are updated daily and linearly interpolated onto each model time step. A constant offset in temperature (-1.5°C) and salinity (-0.3) was applied to the ASTE fields to tune to available mooring and profile records near the mouth of Sermilik fjord (Fig. 2).

Model surface forcing was taken from ERA5 (Hersbach et al., 2020). Surface fluxes were generated within MITgcm external forcing module using 10-m winds, humidity, air temperature, and downward shortwave and longwave radiative fields. Surface forcing fields were updated hourly with a linear interpolation to simulation time steps. While ERA5 realistically simulates shelf forcing, the fjord is largely unresolved. No sea ice was included in the model.

For a brief description of the wind forcing, we plot the wind stress on the shelf at the southern edge of the coastal transect (Fig. 1).The along-shelf wind stress (oriented such that northeasterly wind is negative) is almost always downwelling favorable (Fig. 3). Individual wind events can be intense reaching magnitudes as high as 0.8 N/m^2. A

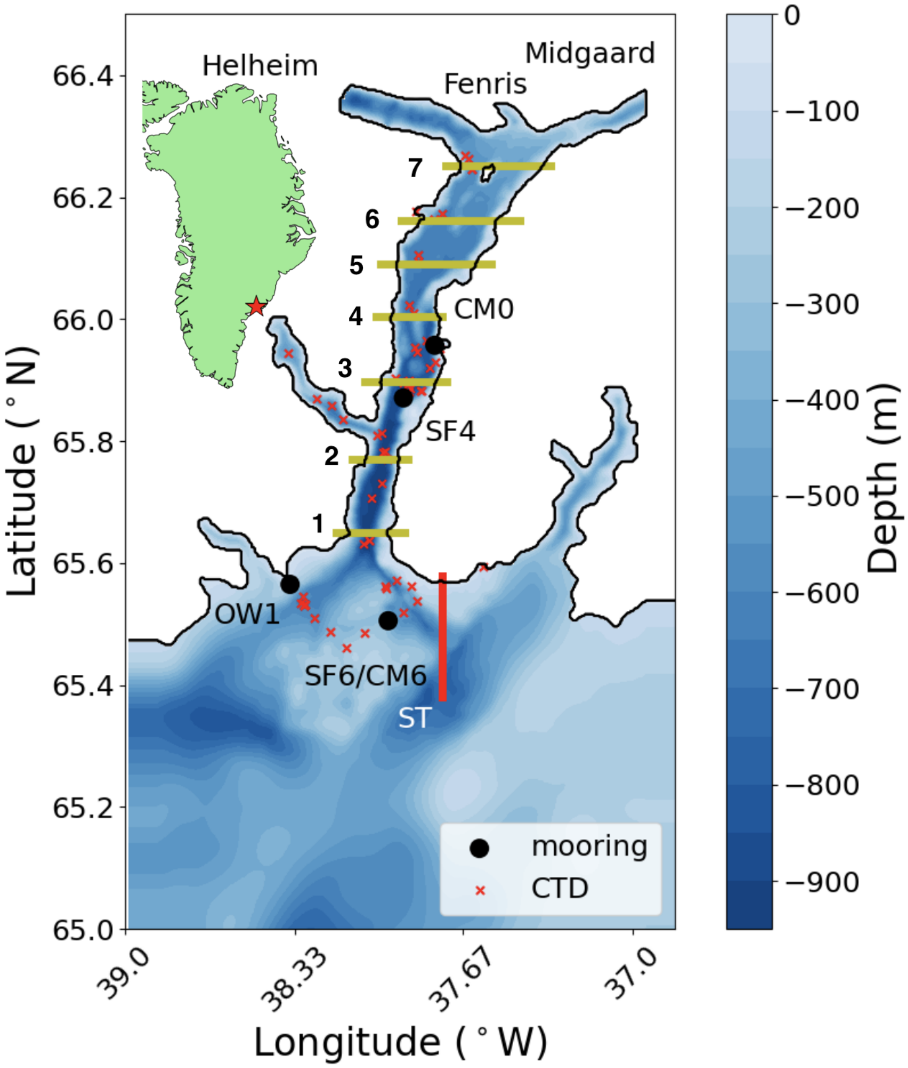

Figure 1. Model domain and bathymetry. In yellow are the gates used for the calculation of TEF fluxes in Sermilik Fjord. The red line is the coastal section used for the shelf seasonality analysis. The locations of observations used in the model comparison are given in black circles (moorings) and red crosses (CTD). The glacier names are given at the top. Sermilik Trough (ST) is shown in white text. The inset map shows the location of Sermilik Fjord in the context of Greenland.

low-pass wind stress representative of seasonal wind patterns, τ_{lp} is calculated using a 90 day, 6th order Butterworth filter. τ_{lp} shows the winds are strongest from November to May and weakest from June to August (Fig. 3a).

We compare two three-year simulations in this manuscript. The first is configured as described above without representation of the glacial runoff and melt. This run is referred to as the 'No Glacier' (NG) run. The second is referred to as the 'With Glacier' (WG) run. Within the WG run, subglacial discharge plumes and glaciers were added to the three glaciers at the north end of SF (those named in Fig. 1). This cold, fresh water originates as surface melt of the glacier, and peaks in summer. It makes its way through

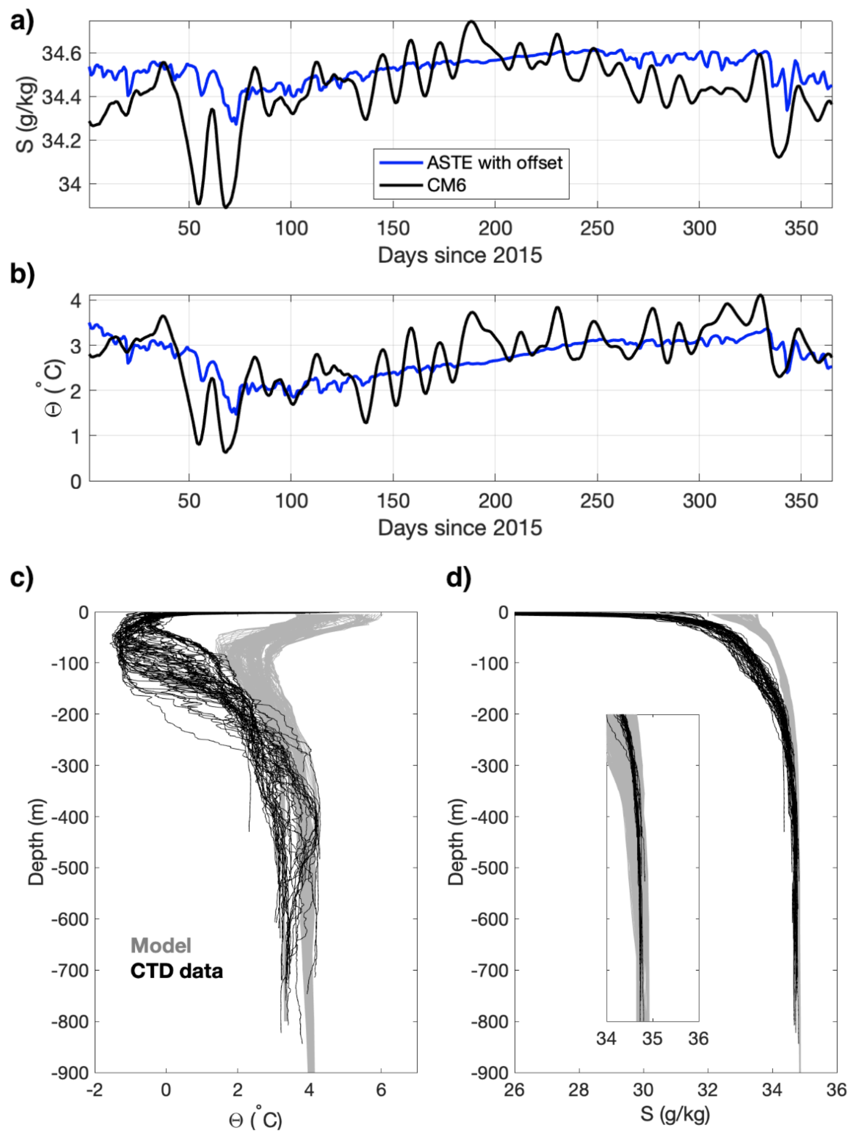

Figure 2. a-b) Comparison of ASTE boundary conditions with shelf mooring located at CM6 (Fig. 1).c-d) comparison of model output from Sermilik Fjord over the months of July and August 2015 against CTD profiles taken in August 2015. The inset in panel d is a zoom on the region between 34 and 36 g/kg. The y-axis is shared with the larger figure.

to the base of the ice sheet and enters the ocean at depth at the grounding line to become a buoyant, turbulent plume. Within the WG run, plume dynamics are parameterized following T. Cowton et al. (2015). Discharge values come from regional climate simulations compiled by Slater et al. (2020). A constant discharge is used for each month. Subglacial discharge is applied to all months and varies interannually (Fig. 3). Peak discharge in the summer at each glacier is 300-600 $\mathrm{m^3\,s^{-1}}$. Discharge in the winter is 2–5 $\mathrm{m^3\,s^{-1}}$. Although this run includes a melting iceface, the input from the glacier is negligible and the main difference between NG and WG are the effects of the subglacial discharge plume. Therefore, we will refer to circulation initiated by glacial forcing as the "plume-driven"

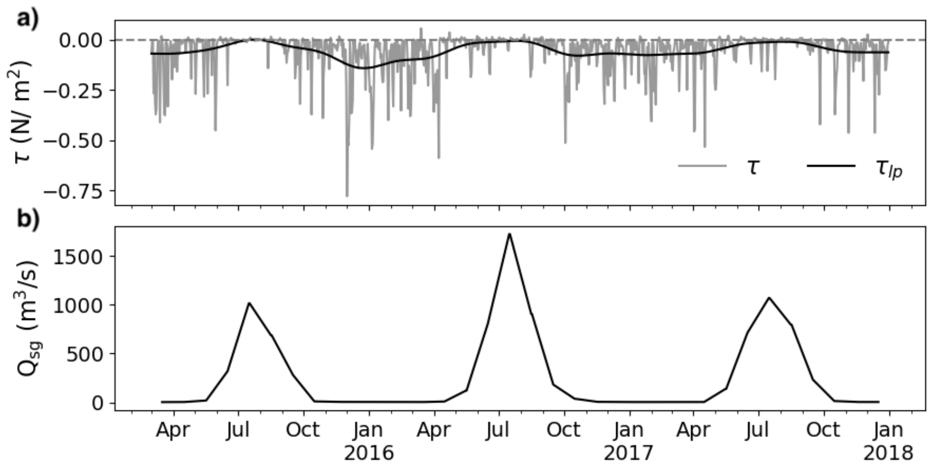

Figure 3. a) Along-shelf wind stress peaks in winter. The daily along-shelf wind stress is in gray and τ_{lp} is in black. Negative is towards the southwest. b) The total subglacial discharge (Q_{sg}) flux in the WG run.

circulation. The NG and WG simulations were identical apart from the addition of glacial plumes.

A full comparison of the model output against observational data is given in Appendix A, but is briefly described here. Both visually (Fig. 2 and Fig. A1) and quantitatively, the model does a reasonable job of recreating the temperature and salinity variability seen in the observations. The mooring data on the shelf is significantly correlated (r = 0.75) in salinity and temperature (r = 0.51) over 30-day timescales. Additionally, both the salinity and temperature were significantly correlated on higher-frequency timescales (< 30 days) giving confidence that higher shelf-forcing is reasonably represented (Table A1). The volume transport in the model does not deviate substantially from the estimates of the transport from the observations, although it does underestimate the summer transport (Sup. Fig. 1). However, we recognize that the model cannot reproduce the shallower properties such as PW salinity and stratification because it is missing freshwater sources such as icebergs, sea ice and surface runoff (Fig. 2). Other models (Davison et al., 2020; Kajanto et al., 2023) and observations (Moon et al., 2018) suggest the freshwater flux from icebergs can increase the strength of circulation and significantly modify (cool and freshen) shallow fjord properties increasing stratification. Recently, Kajanto et al. (2023) showed, for a similar large fjord in west Greenland, that without icebergs the model could not reproduce the observed properties. Therefore, our results are focused on shelf-forcing and plume transport, both of which appear reasonably well represented, and we leave iceberg forcing to be implemented in a future study.

4 Total Exchange Flow Method

The transport of heat, salt, nutrients and other tracers out of the fjord is set by the exchange flow. In traditional estuaries, the exchange flow describes the sub-tidal mean circulation, typically with inflowing salty water at depth and outflowing fresher water near the surface (MacCready & Geyer, 2010). A key characteristic of the classic exchange flow is that the circulation, set up by river input and mixing, drives a volume flux out of the estuary many times greater than the initial freshwater volume flux. Applying the exchange flow concept to deep glacial fjords, we let wind-driven variability (1–10 days) play the role of tides (high-frequency oceanic variability) and glacial freshwater to play the role of river input (buoyancy) in setting up a low-frequency exchange flow (Jackson & Straneo, 2016). Using the exchange flow framework, we can analyze the role of shelf and glacial forcing in setting fjord properties.

We use the Total Exchange Flow (TEF) method (MacCready, 2011; MacCready et al., 2018; Burchard et al., 2018; Lorenz et al., 2019) to evaluate bulk properties of the model exchange flow, such as incoming/outgoing volume flux $Q_{\text{in}}, Q_{\text{out}}$, incoming/outgoing Salinity $S_{\text{in}}, S_{\text{out}}$, and incoming/outgoing Temperature $\Theta_{\text{in}}, \Theta_{\text{out}}$. TEF allows a calculation of exchange flow properties consistent with the Knudsen relation in salinity space (Burchard et al., 2018). Typically, TEF averages are calculated in salinity coordinates rather than spatial coordinates allowing both tidal and sub-tidal fluxes to contribute to the exchange flow. For SF, temperature gradients are non-negligible to the overall pressure gradient and partially compensate salinity, therefore, we use density coordinates rather than salinity coordinates to evaluate the changes in volume (mass) transport (Lorenz et al., 2020). While density coordinates are used for volume transport, when considering salt or heat budgets, salinity and temperature coordinates are necessary (Lorenz et al., 2020). Therefore for salt and heat fluxes, we use salinity and temperature coordinates respectively.

The TEF transport (Q_i^b) of a tracer b in coordinates i is (Lorenz et al., 2020)

$$Q_i^b = \left\langle \int_{A(i)} bu\mathrm{d}A \right\rangle, \tag{1}$$

where $A(i)$ is the area of a cross section with coordinates greater than i, u is the velocity normal to the cross section defined to be positive inwards, and $\langle\rangle$ denotes temporal averaging. For example if $b = 1$, and $i = \sigma$, then Eq. 1 calculates the net volume transport with $Q_\sigma(0) = -Q_{\text{BT}}$, the total barotropic flux, and $Q_\sigma(\sigma_{max}) = 0$. We sort the data into 1000 discrete bins and use a 30-day rolling mean in place of a Godin (tidal) filter, to average over the wind variability (Jackson & Straneo, 2016). The derivative of Eq. 1 gives a tracer flux

$$q_i^b(i) = -\frac{\partial Q_i^b(i)}{\partial i}, \tag{2}$$

as a function of coordinate choice. To get the total incoming (outgoing) tracer flux we then integrate Eq. 2 over the portions that are inflowing (outflowing). We use the dividing salinities method (Lorenz et al., 2019) which identifies the extremum in Q_i^b as the dividing coordinate class i_{div} to define inflowing and outflowing regions. The bulk tracer values are $b_{\text{in}} = Q_{\text{in}}^b/Q_{\text{in}}$ and $b_{\text{out}} = Q_{\text{out}}^b/Q_{\text{out}}$ where b can be salinty S, Potential Temperature Θ or Potential Density anomaly σ. Note that Q_{in} calculated in σ space is not the same as Q_{in} calculated in S or Θ space, and the appropriate volume flux choice depends on the tracer budget being considered. Additional details for calculating TEF from a numerical model are given in Lorenz et al. (2019). All TEF ouput is calculated here using the pyTEF library (Lorenz et al., 2020). We calculate TEF values on 7 transects along SF fjord (Fig. 1). For the time series of TEF transport, we show the transport at the 3rd line (SF Line 3).

5 Shelf-Forced Circulation

5.1 Contribution of CTWs to Shelf-driven Circulation

Both Fraser et al. (2018) and Jackson et al. (2018) have identified coastal-trapped waves (CTWs) as the primary mechanism through which the wind-driven forcing is communicated to southeast glacial fjords, and CTWs have been observed in other dynamically-wide Arctic Fjords (Inall et al., 2015). We evaluate the contribution of CTWs to the shelf-driven circulation by comparing the model output with an analytical model of CTWs. While the theory is described here alongside the background on CTWs, the analysis is carried out in Section 7.3. For our analysis, we use the Kelvin-wave model from Jackson et al. (2018) who showed that Kelvin waves were a good representation of coastal-trapped waves in Greenland's fjords due to their steep sides. The Kelvin-wave model uses a two-layer approximation with the volume flux in the top layer given by

$$Q_{\mathrm{ctw}} = 2cR_{\mathrm{d}}\left(1 - \mathrm{e}^{-W/R_{\mathrm{d}}}\right)\sin\left(\frac{\omega}{c}(L + W/2 - y)\right)\eta(t), \tag{3}$$

where η is the amplitude of the pycnocline fluctuation at the mouth, y is the distance from the mouth, ω is the forcing frequency, c is the baroclinic wave speed, L is the fjord length, W is the fjord width and R_{d} is the deformation radius $R_{\mathrm{d}} = c/f$ where f is the Coriolis frequency. For our application, $c = \sqrt{g'h'}$ where g' is the reduced gravity between the upper layer h_1 and the bottom layer h_2, and $h' = h_1 * h_2/(h_1 + h_2)$ is the effective height. The layer heights were calculated by solving for the depth of the zero crossing of the first horizontal normal mode at the fjord mouth (Hughes et al., 2018). On average, $c = 0.68$ m/s, but it varies between 0.5 and 0.9 m/s from winter to summer respectively. This speed is lower than observations (Jackson et al., 2014, $c = 1.1$ m/s). This difference is most likely attributable to weak model stratification compared to observations. We define pycnocline fluctuations as

$$\eta_{\mathrm{M}} = \frac{\Delta\sigma}{\overline{\sigma_z}}, \tag{4}$$

where σ is the potential density anomaly at the mouth of the fjord and $\overline{\sigma_z}$ is a 30-day rolling mean of the section-averaged vertical density gradient at the mouth.

Since the fjord experiences broadband forcing rather than a single forcing period, we Fourier transform η to a function of frequency $\hat{\eta}(\omega)$ and use Eq. 3 to solve for $\hat{Q}_{\mathrm{ctw}}(\omega)$, and then inverse Fourier transform to get $Q_{\mathrm{ctw}}(t)$. However, a challenge arises because c is a function of t and is inside of the sine term which is a function of ω. Therefore, we instead calculate a 2D matrix of $\hat{Q}(c,\omega)_{\mathrm{ctw}}$ using constant values of $c = [0.4, 0.5, \ldots, 1.1]$ m/s. We then inverse Fourier $\hat{Q}$ and use a timeseries of $c(t)$ to interpolate across $Q(c,t)_{\mathrm{ctw}}$ and recover a 1D time series. The calculated CTW volume flux is about 66% the magnitude of the high-frequency (< 15 days) incoming volume flux (Sup. Fig. 9) suggesting the CTW theory is slightly underestimating CTW flux or additional high-frequency variability is present.

We apply a 30-day rolling mean to average over synoptic variability. The resulting flux is the net volume flux in the top layer. If we treat the fjord as two layers, then we can assume this flux is balanced by an opposite flux in the other layer. Therefore, the incoming flux will switch between the top and bottom layers as the pycnocline fluctuates, and so the total incoming flux can be written as $Q^*_{\mathrm{sh}} = |Q_{\mathrm{ctw}}|$, where the star indicates this is an analytical model and the subscript sh represents shelf forcing.

5.2 Model Shelf Circulation and Variability

On its ocean boundary, SF is externally forced by the circulation and variability on the continental shelf. The shelf outside SF is characterized by the confluence of PW carried in from the coastal current (East Greenland Coastal Current, EGCC) and AW transported along Sermilik Trough (ST, Fig. 4). Closer to the surface, the EGCC can be seen as a westward flowing current carrying relatively cold water (Fig. 4a). The gradient between these two water masses is relatively diffuse indicating lateral mixing over the shelf and trough. At greater depths, relatively warm AW is steered into the fjord along ST, although there are recirculation cells within the trough system (Fig. 4b). The across-shelf isopycnal gradient (discussed later this section) sinks towards the coast resulting in lighter, cooler water closer to the fjord at a fixed depth.

The shelf properties upstream (east) of SF (Fig. 1, red line) vary in response to both wind forcing and external water mass variability. Two month averages of temperature in the NG run are highest in the fall (Sep. – Oct.) and coolest in the spring (Mar.

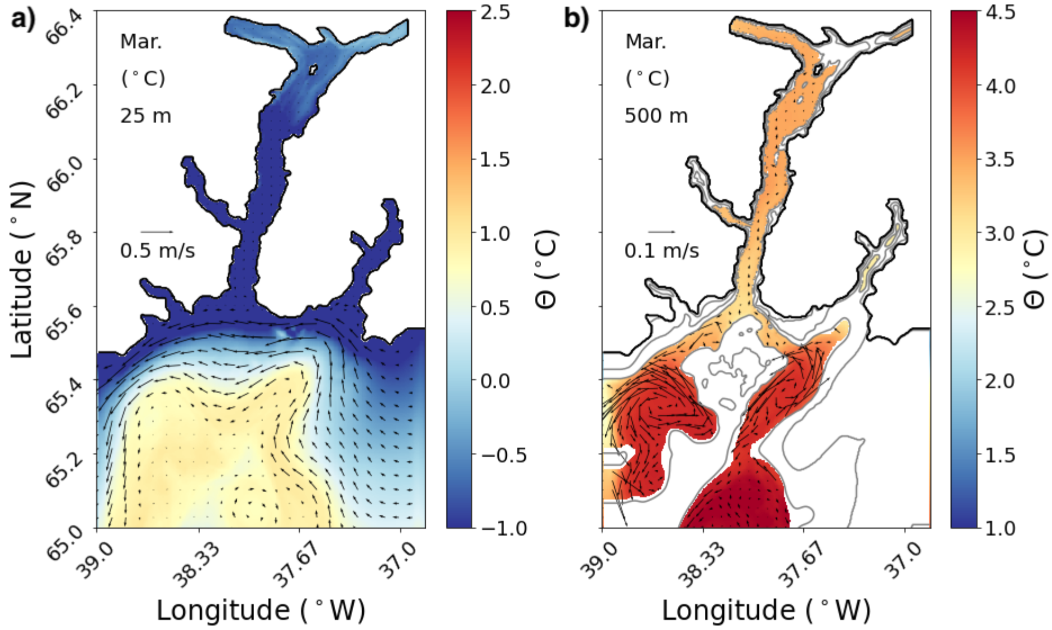

Figure 4. Plan view of temperature (color) and velocity (vectors) showing the coastal current at 25 m and the inflowing AW at 500 m in Sermilik Trough. Each figure is produced from the monthly average (March 2017) of temperature and velocity from the NG run at (a) 25 m depth and (b) 500 m depth. The depth contours are 100, 250 and 450 m. Note the different colorbars and velocity scales between the two panels.

– Apr., Fig. 5). In September, when the waters on the shelf are warmest, the AW extends all through the water column and onto the shelf (Fig. 5e). During the rest of the year, a cold PW cap is present close to the coast, however its lateral extent appears variable and dependent on the steepness of the isopycnal slope. The density gradients across the shelf are strongly correlated with the daily along-shelf wind stress ($r = 0.78$, $p < 10^{-3}$). Therefore, the isopycnals are compact and relatively flat in the summer months when the winds are weaker. The isopycnals start to steepen in the fall and early winter in response to downwelling-favorable winds. When the isopycnals are steepest, the ratio of cold PW to warm AW is highest. Additionally, the coastal current is strongest in the fall and winter when isopycnals are steepest (Fig. 6), consistent with geostrophy. The upstream transect shows little difference in properties between the NG and WG run (not shown), and therefore, we assume the forcing associated with isopycnal displacement on the shelf is active and equivalent in both runs.

We also examined the coastal current downstream (west) of the fjord. The NG and WG runs diverge and a relatively fresh wedge can be observed close to the coast in the WG run July through September (Sup. Fig. 3). However, in these downstream sections we do not observe substantial differences in temperature or current velocity (Sup. Fig. 3 and 4).

5.3 Fjord Circulation and Properties (No Glacier)

In the NG run, the circulation in the fjord responds to shelf forcing driven in large part by local, along-shelf, winds. To examine the circulation, we focus on a cross-section at SF Line 3 as this location is closest to the mooring SF4 and is representative of circulation away from mixing processes at the head and the mouth of the fjord. We find

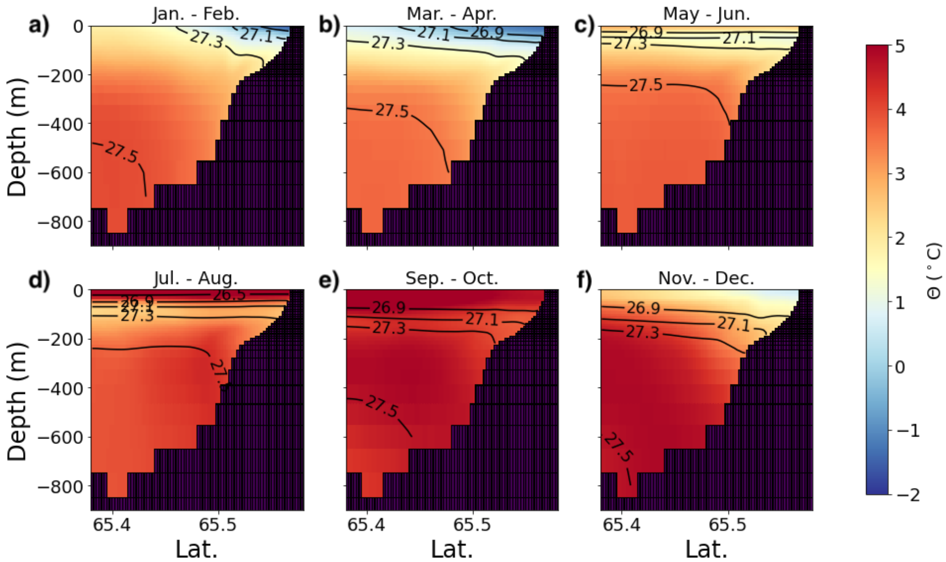

Figure 5. Isopycnals separating surface and trough waters are flat in the summer months and steep in the winter months. Each panel shows two month averages of coastal section temperature (No Glacier run, see Fig. 1 for location). View is facing west and is perpendicular to coastal current. Contours are isopycnals of potential density anomaly (26.5, 26.9, 27.1, 27.3, 27.5).

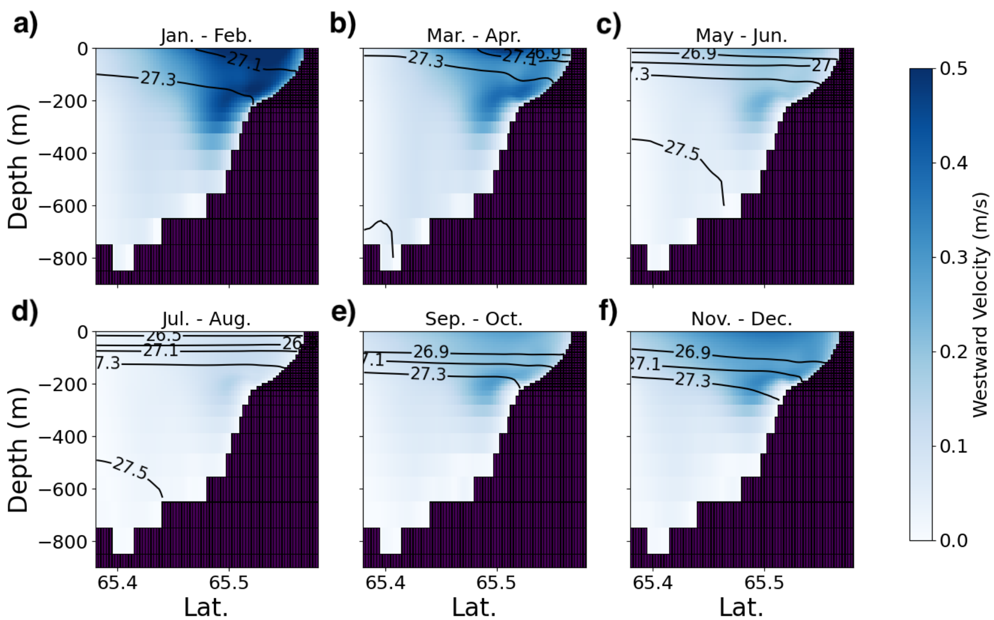

Figure 6. The coastal current is strongest in winter and weaker in summer. Each panel shows two month averages of westward velocity (-U) (No Glacier runs). View is facing west and is perpendicular to coastal current. Contours are isopycnals of potential density anomaly (26.5, 26.9, 27.1, 27.3, 27.5).

that the circulation at the SF Line 3 varies seasonally, exhibits signs of being rotationally-influenced and is characterized by reversals with depth (Fig. 7a–c). The strongest average flow is observed in spring with inflow at depth and outflow around 100 m. By October, the circulation at depth has reversed. The time-varying aspects of this circulation will be examined in greater detail in Section 7.

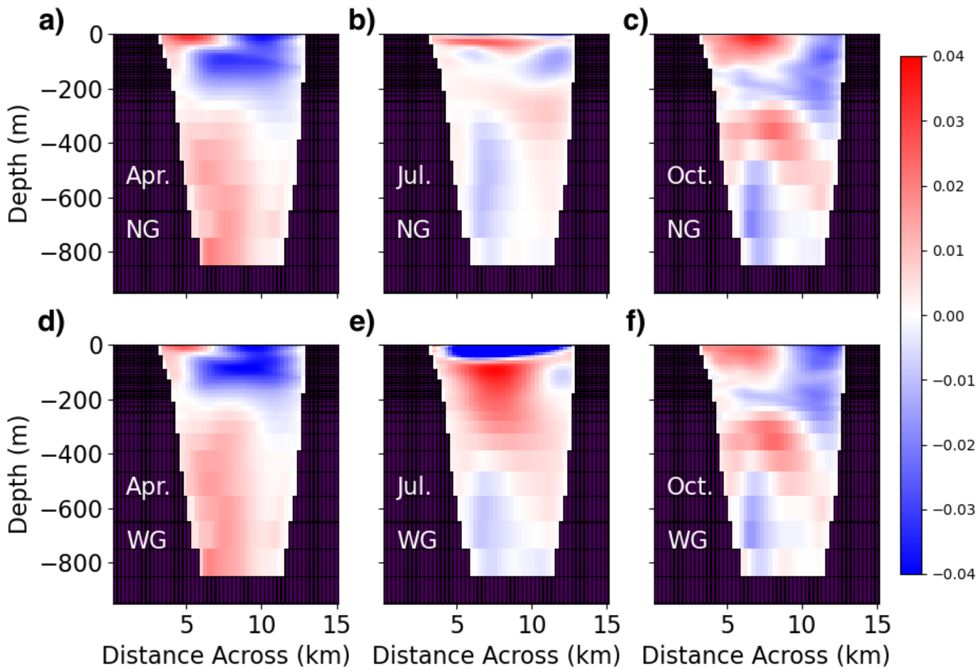

Figure 7. (a–c) monthly averages of velocity at the mouth of the fjord in April, July and October for the NG run. d–f) in April, July and October for the WG run. Positive velocities are flowing into the fjord.

Compared to the shelf section, variability of temperature and density along fjord is weak (Fig. 8a–c). Isopycnals lie flat within the fjord and only have a notable slope in the upper 100 m and approaching topography. The fjord shoals from 900 m at the mouth to 500 m near the branching point (70 km) and increases in depth again as it approaches Helheim glacier (90 km). The isopycnal 27.45 kg/m^3 associated with deep, relatively warm water can be seen to reach its shallowest depth (and maximum thickness) during July, but the warmest waters are present in October.

A width-averaged overturning streamfunction demonstrates the changes in fjord circulation between April and October. The overturning circulation is positive in April with inflow at depth and outflow near the surface (Fig. 9a). In July, the circulation is sluggish and slightly negative (Fig. 9b). By October, the circulation appears three-layered with a fully reversed circulation at depth and a shallower cell in the upper 250 m (Fig. 9c).

In the the absence of glacial forcing (NG run), the mid-fjord properties (red, Fig. 10) mirror the shelf variability (black, Fig. 10) in temperature and salinity (TS) space. WPW is found seasonally near the surface ($\Theta \approx 8$ °C), PW ($\sigma \approx 27.0$ kg/m^3) is found at the temperature minimum, and AW is the saltiest and densest water ($\sigma \approx 27.5$ kg/m^3). We see that in the winter months (Jan. – Apr.) the fjord model properties lie in between PW and AW, and the fjord can be described as a two-layer system (Fig. 10). As the surface warms, a distinctive "U" shape forms from the three water masses present: WPW,

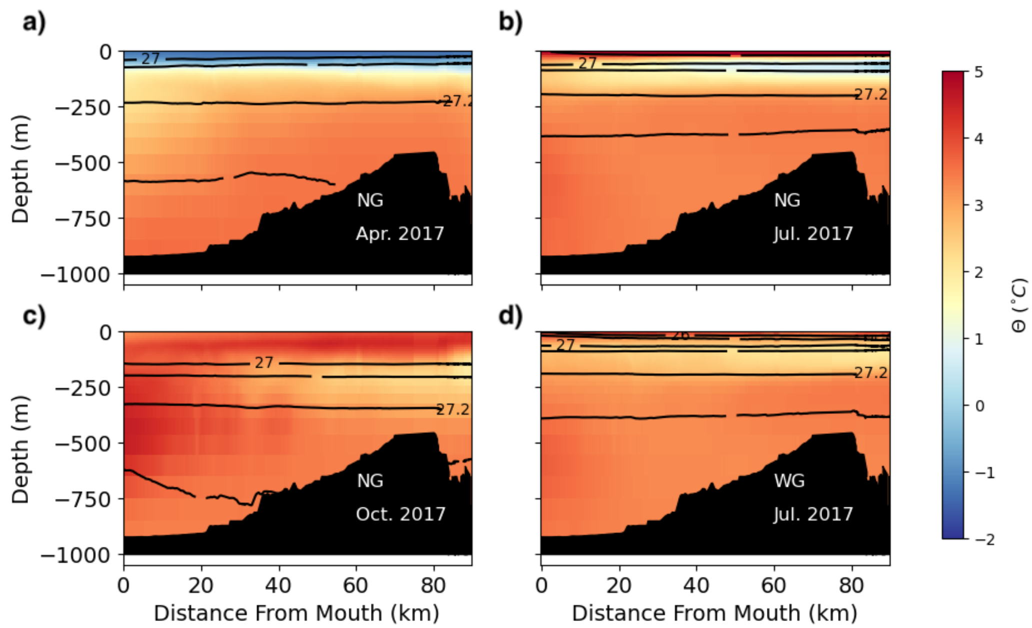

Figure 8. Along-fjord gradients are relatively weak, but properties change seasonally. Width-averaged monthly temperature in April (a) and July (b) and October (c) for the NG run and July (d) for the WG run. The contours are isopycnals of potential density anomaly (26, 27, 27.15, 27.35, 27.45 kg/ m^3).

PW and AW. As the surface cools, the system starts adjusting back towards a two-layer system.

To summarize the results of this section: across-shelf isopycnal gradients are steepest in winter when the winds are strongest, fjord circulation is influenced by rotation but still exhibits vertical shear, and streamfunctions demonstrate significant seasonal variability including reversals in mean fjord circulation.

6 Plume-Driven Circulation

The other model runs includes glacial forcing (WG) with the glacial forcing dominated by the subglacial discharge plume. The inclusion of subglacial discharge plumes alters the fjord circulation and temperature, especially in summer. At SF Line 3, there is substantial difference between the WG and NG runs in July, with a much stronger outflow near the surface and less recirculation in the middle part of the fjord in the WG run (Fig. 7d–f). The non-summer months (Apr. and Oct.) show little difference in velocity magnitude and structure between the two model runs. Taken as a whole, the fjord cross-sections demonstrate that the spatial structure of the circulation is complex and highly variable. In this study, we are primarily interested in overturning (vertical shear) and therefore will be analyzing width-integrated exchange flows.

The July temperature distribution in the fjord is similar in WG and NG except in upper 100 m where it is 2°C warmer than in the NG run (Fig. 8d). This difference can be attributed to subglacial discharge entraining ambient AW and bringing it up to shallower depths via the plume. The overturning steamfunction in the WG run shows the

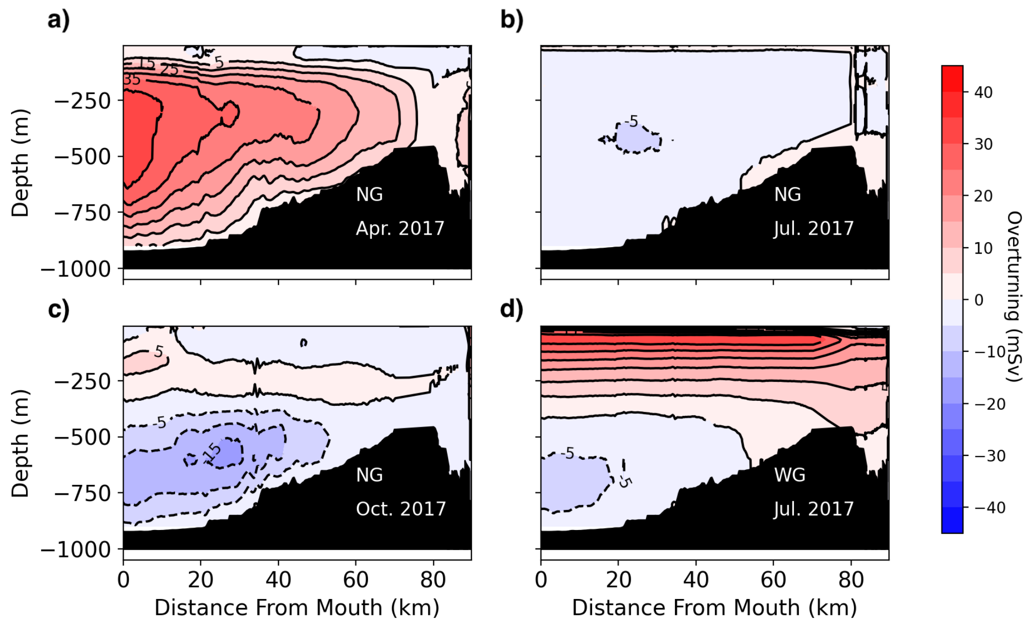

Figure 9. The streamfunction reverses between April and October in the NG run. Width and monthly-averaged overturning streamfunction over April, July and October (NG), and July (WG) in 2015. Counter-clockwise flow is a positive streamfunction.

plume drives strong outflow near the surface (Fig. 9d). Below 400 m, the July WG streamfunction is negative similar to the July NG run.

The TS properties in the WG run reveal the influence of the plume on fjord water properties. The WG run (blue, Fig. 10) starts diverging substantially from the NG run in June due to large amounts of subglacial discharge. This divergence follows the subglacial discharge-mixing line, and the end result is a cooler and fresher surface water mass and the "erasing" of the clear PW signal (temperature minimum). The WG run properties converge back to those of the NG run in October, and therefore we can state that the time period of subglacial discharge influence is June – September. We tested for freshwater storage by calculating the lag between subglacial discharge input and peak freshwater export (Sanchez et al., 2023). We did not observe significant freshwater storage with the peak export averaging a two-week delay over the three years which we attribute to the transit time of water (0.1 m/s) across the fjord.

The summer and winter CTD observations are also included in the TS plots for context. They show that the model surface waters are biased warm during the summer, likely due to a lack of iceberg melt.

7 Exchange Flow Analysis

7.1 Depth Coordinates Exchange-flow Structure

Prior to using TEF, we evaluate the temporal variability of the exchange flow in traditional depth coordinates. The volume transport at SF Line 3 for the NG run is shown in Figure 11a. With three years of data, a picture emerges of seasonal volume transport in the fjord with a reversing circulation below 200 m (Fig. 11a). The volume transport is filtered with a 30-day rolling mean to remove the first-order synoptic variability as-

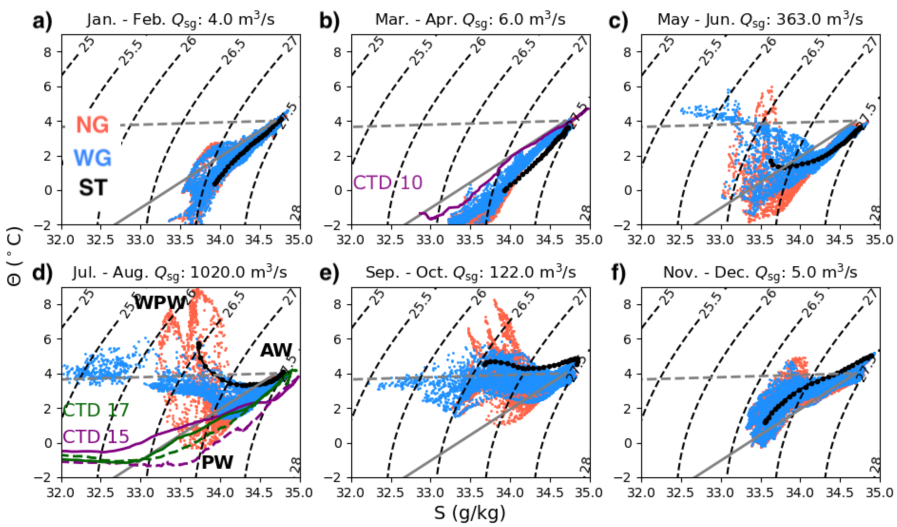

Figure 10. Each panel shows the TS properties over a 2-month period with the spread coming from time (daily) and depth. The blue dots are from the WG run and the red dots are from the NG run. The black line is the TS properties in Sermilik Trough (ST) in the NG run. The gray solid line is the melt-mixing line and the gray dashed line is a subglacial discharge mixing line. The contours are potential density anomaly. Q_{sg} is the two-month average subglacial discharge. The average TS from all CTD profiles collected in Aug. 2015 (33), Jul. 2017 (31), and Mar. 2010 (4) are in purple. Dashed and solid lines separate shelf and fjord profiles, respectively. The water mass locations are labeled in panel d.

sociated with the winds. The volume transport is roughly in two layers below 200 m (Fig. 11). The circulation is inflowing at depth in the spring and reverses to outflowing during the summer. This circulation is interrupted, especially in the upper 200 m, by the cumulative effects of wind events that are not completely filtered out. The seasonal cycle dominates over interannual variability.

The isolated plume-driven transport (the WG run with the NG run subtracted) shows a strong seasonal cycle with an increase in outflow during the summer and a compensating inflow between 200 and 500 m (Fig. 11b). The primary outflow depth appears to rise and fall each summer consistent with a neutral buoyancy depth that is based on the magnitude of subglacial discharge.

Applying TEF to SF line 3 enables us to calculate the seasonal volume transport of the fjord in density space (Fig. 12) and allows direct connection with water mass variability. The composite TEF analysis shows that the NG transport is generally concentrated in the most dense layers. During the first half of the year, the deep flow is positive with inflow at depth and outflow at lighter densities. As seen in depth space (Fig. 11), the flow reverses in the second half of the year. Upon closer inspection, the inflowing density from January to June can be seen to be getting progressively denser filling the fjord with a greater concentration of AW. When the exchange reverses, the outflowing deep water can be seen getting progressively lighter. The WG circulation stands out in the summer and it overtakes the background NG circulation (Fig. 12). The inclusion of the plume alters the total circulation enough to prevent the deep reversal from occurring until later in the fall. The TEF composite profiles also highlight the multi-layered exchange occurring in SF (Fig. 11 and 12). In the winter months, there are multiple zero

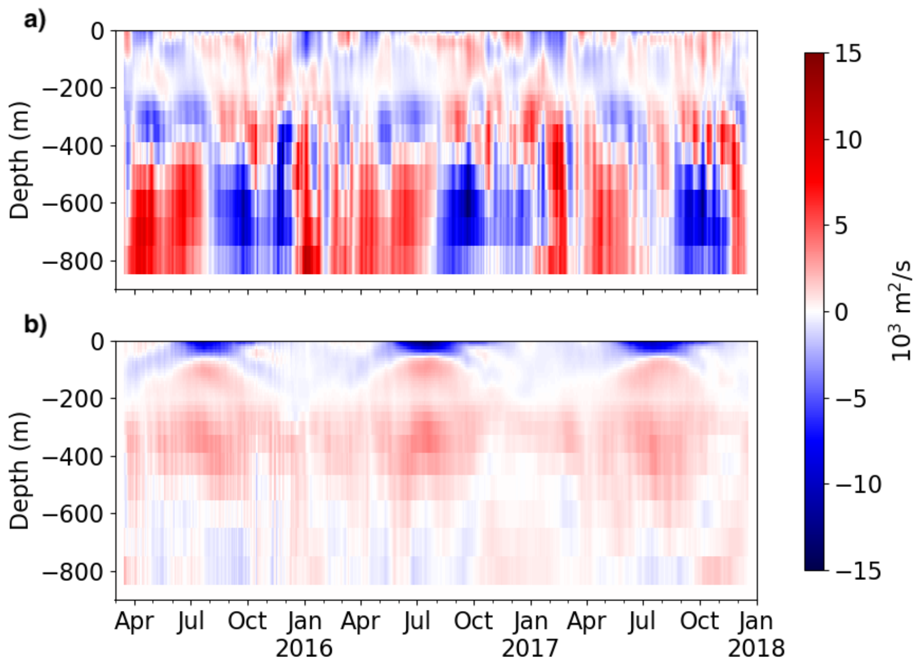

Figure 11. a) 30-day rolling mean volume transport in the NG run at SF line 3 as a function of depth and time. Positive transport is into the fjord. b) The difference between the volume transport in the WG run and the NG run at SF line 3.

crossings separating the outflowing and inflowing cores at 27 kg/m^3 and 27.3 kg/m^3 respectively. The multiple inflows raise questions as to the physical meaning of TEF terms such as S_{in} or S_{out}. With this caution in mind, our analysis of TEF bulk values will assume they are representative of a larger 2-dimensional overturning circulation.

7.2 Exchange Flow Connections with Wind Stress

The exchange flow reversal exports AW (Fig. 10 and 12) and is therefore an important lever in reducing the heat available to melt. We propose that the seasonality of the winds is responsible for the reversal by flattening isopycnals across the shelf during the spring. The mean state of the winds along the shelf is consistently downwelling favorable, such that a relaxation towards no winds acts effectively as upwelling. The changing slope of isopycnals in Sermilik Trough are qualitatively consistent with this picture (Fig. 5).

The relationship between low-frequency wind forcing and the exchange reversal is tested by comparing the time derivative of low-pass along-shelf wind stress (τ_{lp}) and the sign of TEF exchange (Fig. 13). Both of these variables are related to the change in pycnocline depth, if the exchange sign is negative then the fjord is getting lighter (pycnocline deepening). The exchange flow direction is represented through a 15-day low-pass Butterworth filter of $\Delta\sigma = \sigma_{\text{in}} - \sigma_{\text{out}}$ from the NG run at SF Line 3. The goal of this filter is to reduce synoptic forcing since we are interested in the change in exchange flow direction on longer timescales. When $\Delta\sigma > 0$, the exchange flow is positive with inflow at depth. The derivative of the seasonal wind stress is significantly correlated with $\Delta\sigma$ ($r = 0.59$, $p < 10^{-3}$) suggesting that wind variability is consistent with the sign

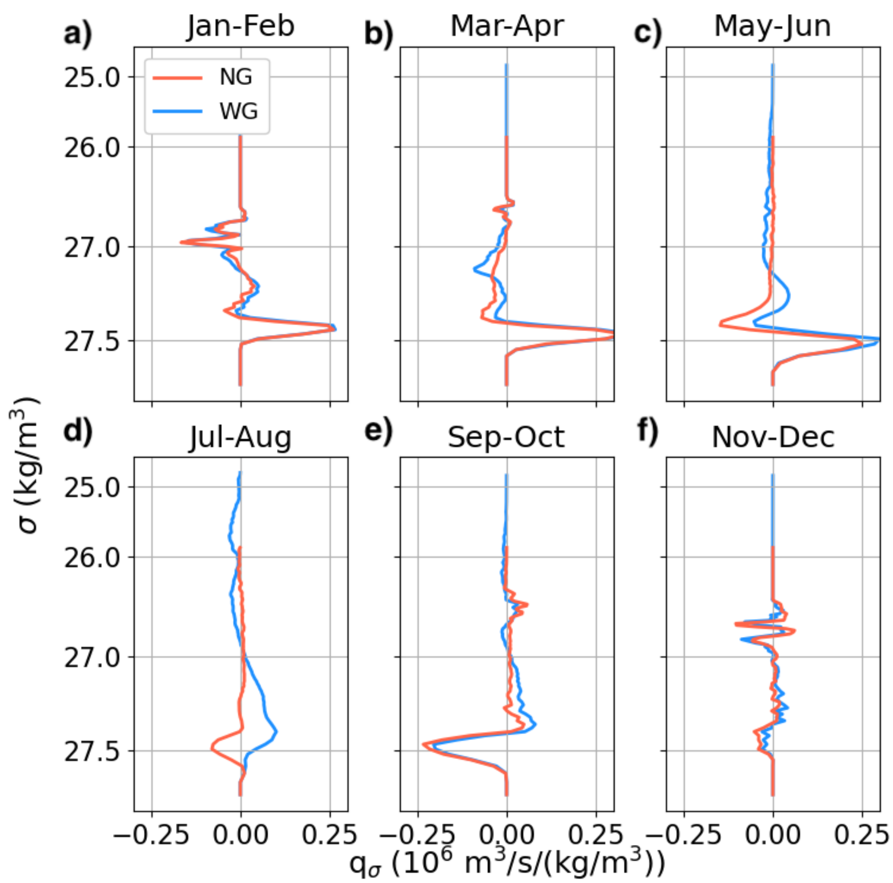

Figure 12. The AW inflow ($\sigma \sim 27.4$ kg / m^3) becomes progressively denser until July and then reverses becoming progressively lighter. Each panel is a three-year average over the two months evaluated at SF Line 3. The x-axis is volume flux per density class. The y-axis is potential density anomaly σ . Note the y-axis is nonlinear so that greater resolution can be given to the deepest densities. Red is from the NG run, and blue is from the WG run. 50 density bins were for used this figure instead of 1000 for clarity.

of the exchange flow. The seasonal variability of wind stress therefore likely plays an important role in setting the amount of AW in SF with relaxing winds leading to a greater concentration of AW.

7.3 Variability of TEF Bulk Properties

We quantify the TEF exchange volume flux as

$$Q_{\mathrm{e}} = \frac{Q_{\mathrm{in}} - Q_{\mathrm{out}}}{2}, \tag{5}$$

where Q_{in} is the TEF inflowing volume flux (calculated in density space) and Q_{out} is the outflowing flux with $Q_{\mathrm{e}} \geq 0$ (MacCready et al., 2018). In the NG run, the cycle of the exchange flux is consistent with the seasonal cycle of wind forcing with the greatest flux occurring during the winter months (max 60 mSv) and weak exchange during the summer (max 10 mSv) (Fig. 14a). The exchange flux in the WG run diverges from the NG

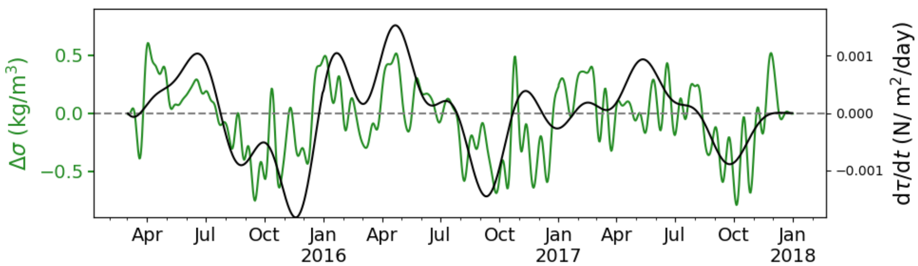

Figure 13. Flow reversals are correlated with changing wind stress. In green (left axis) is the difference between the TEF calculated σ_{in},σ_{out} at SF line 3 smoothed with a 15-day low-pass filter. Positive indicates inflow at depth. The data come from the NG run. The right axis (black) is the derivative of the (90-day low pass) along-shelf wind stress

run during the summer with peak exchange around 40 mSv. Since the plume forcing is strongest in the summer when the shelf-driven circulation is weakest, the exchange exceeds 30 mSv for the majority of the year. In the WG run, the exchange minimum is found in the non-summer months and varies from year to year depending on wind strength. In 2015 and 2016 the minimum occurs in November after the plume has shut off and during a relatively weak period of winds, but in 2017 the minimum occurs in March.

To isolate the plume forcing against the background shelf forcing, we separate the exchange flux into the plume-driven exchange (WG-NG) and shelf-driven exchange (NG). The plume-driven exchange flux peaks in July and the timing coincides with the input of subglacial discharge (Fig. 3b)

We compare the shelf-driven exchange (NG) with CTW theory (Eq. 3, Section 5.1). Forcing other than CTW exists in the NG run, but we use the CTW theory as a first-order approximation of the exchange flow. The exchange flux predicted by variation in pycnocline depth is correlated with the NG exchange flux ($r = 0.48$, $p < 10^{-3}$, Fig. 14c). However this is because both fluxes peak in winter. Individual peaks in the CTW theory do not necessarily align with peaks in the NG flux. The theory suggests minimal impact of CTWs in summer when there is still an exchange on the order of 20 mSV. Clearly, additional factors are influencing the exchange in the NG run, but the comparison indicates that CTW dynamics can be a significant contributor to the background exchange flow.

Subglacial discharge drives a large salt exchange and export of freshwater onto the shelf (Fig. 14d). The salt exchange is defined as $Q_\mathrm{e}\Delta S$ where $\Delta S = S_{in} - S_{out}$, with Q_e calculated using salt coordinates. When $\Delta S > 0$, the exchange flow is positive with inflowing salty water at depth and the export of fresher water above. The plume is the largest seasonal driver of the salt flux with the WG run salt flux peaking during the summer (Fig. 14d). In the absence of subglacial discharge forcing, the exchange salt flux is relatively weak during the summer. The rest of the year the salt flux is variable due to wind forcing, but is generally negative in the fall and positive during the winter when the circulation reverses.

The heat exchange is defined as $Q_\mathrm{e}\Delta\Theta\rho c_w$ where $\Delta\Theta = \Theta_\mathrm{in} - \Theta_\mathrm{out}$, c_w is the specific heat capacity of seawater and Q_e is calculated in temperature coordinates. When $\Delta\Theta > 0$, the exchange flow is positive with inflowing warm water at depth and the export of cooler water above. The heat exchange is dominated by the shelf-driven circulation (Fig. 14e) and therefore fluctuates between positive and negative depending on wind-strength. The addition of subglacial discharge results in a negative heat exchange in the WG run, that is the fjord is exporting heat, but this flux is small in comparison to the larger fluctuations in the winter.

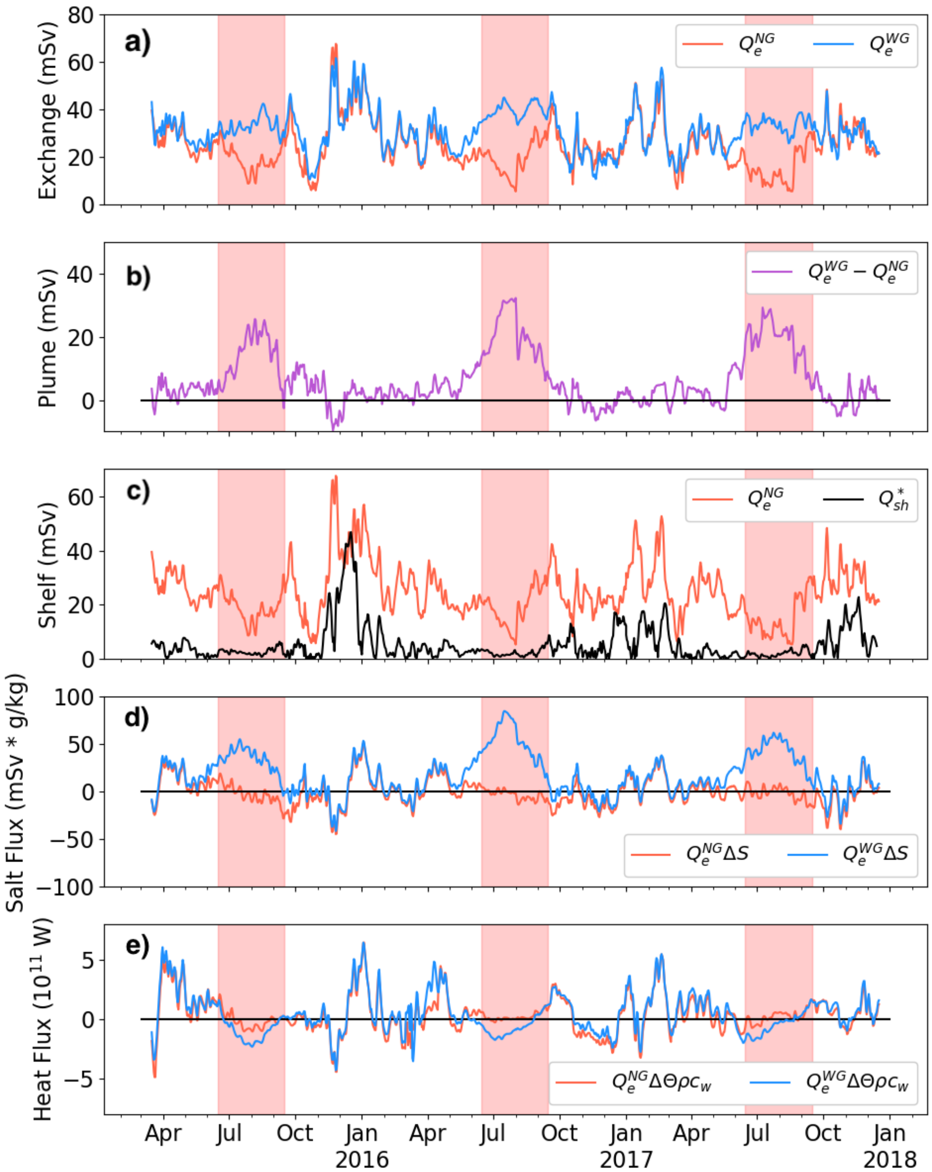

Figure 14. The shelf-driven and plume-driven exchange fluxes have peaks during the winter and summer months, respectively. a) Exchange flux at SF line 3 in the NG and WG run. Units are in mSv (10^3 m^3/s). Red shading indicates summer period (Jun. 15 – Sep. 15). b) The difference between the WG and NG runs at SF line 3. c) Exchange flux estimated from coastal-trapped waves (J18) and the NG run. d) Salt Flux from the exchange flow. The black line separates positive (incoming salt) from negative salt flux. e) Heat flux from the exchange flow. Positive Heat flux would make the fjord warmer.

In summary, the TEF results and shelf-plume forcing comparison indicate that the timing of subglacial discharge results in a strong exchange flow when the shelf-driven circulation (Q_e^{NG}) is relatively weak. The peaks in shelf and plume-driven circulation (Q_e^{WG}-

Q_e^{NG}) are consistent with the timing of subglacial discharge and CTWs lending confidence to our understanding of the drivers of the exchange flow. The exchange salt flux in the WG run consistently peaks in the summer, while both the heat and salt flux in the winter are more variable.

7.4 Along-Fjord Variability of Q_e

Given the different forcing source locations, we expect the shelf-driven circulation and plume-driven circulation to produce different along-fjord variability. The shelf-driven circulation, active in non-summer months, is most intense at the mouth of the fjord and decays with distance (Fig. 15a). In contrast, the plume-driven circulation in summer (Jun. – Aug.) decays only slightly as it flows down the fjord. The bulk TEF properties S_{in} and S_{out} are nearly constant along the length of the fjord (Sup. Fig. 7) suggesting that vertical mixing is weak in the fjord interior.

The flushing time V/Q_e is defined as the volume upfjord of a section divided by the exchange flux and is a scaling for residence time within the fjord. The flushing time when the shelf-driven circulation dominates (Winter, Spring, Autumn) is always larger than the flushing time in summer and only decreases to between 100 – 150 days (Fig. 15b). The plume-driven circulation flushing time is similar to winter near the mouth of the fjord, but drops linearly towards the head resulting in a flushing time of 50 days closer to Helheim Fjord. The contrasting along-fjord slopes suggests the plume-driven circulation is more effective at renewing the fjord than the shelf-driven circulation. For a long fjord such as SF, the magnitude of the shelf-driven circulation has been reduced by 66% 70 km upfjord while the plume-driven circulation is most intense near the terminus where entrainment is high (5 – 10 km). This flushing time is meant to provide a scaling for residence time within the fjord, and we note other residence time scalings such as the freshwater fraction method produce different residence times, but a qualitatively consistent picture.

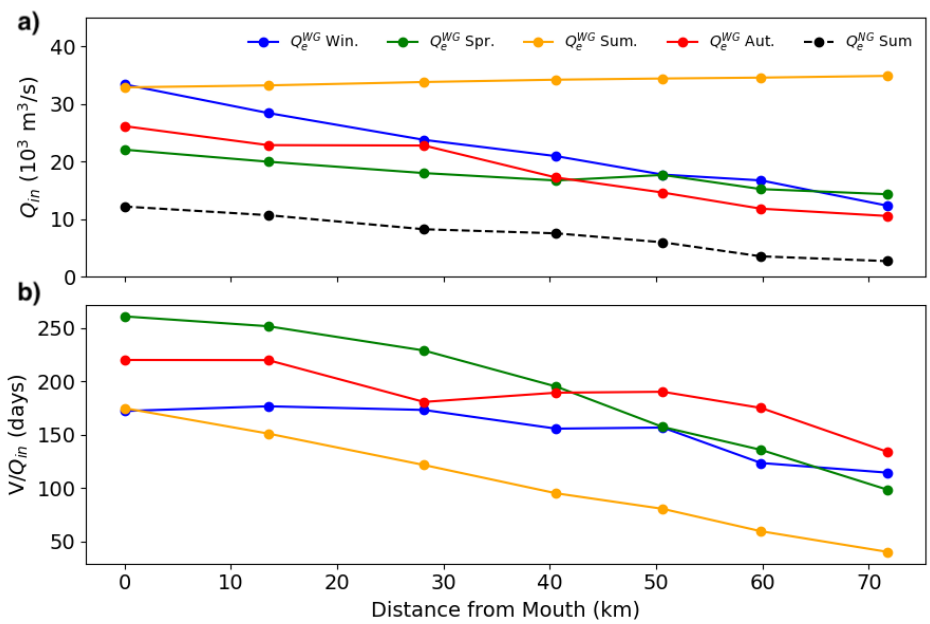

Figure 15. The exchange flux associated with winds decreases from the mouth, while the exchange flux from the plume is constant along the fjord. a) Along-fjord TEF exchange flux in 2016. Seasons are averages. The solid lines are from the WG run and the black dashed line is from the NG run during the summer. b) The fjord volume upstream of the mouth divided by the exchange flux. Win is Winter (Jan. – Feb.), Spr. is Spring (Mar. – May), Sum. is Summer (Jun. – Aug.), Aut. is Autumn (Fall, Sep. — Nov.).

8 Discussion

8.1 Warm-water Seasonality

Identifying the heat content variability of glacial fjords is essential given the sensitivity of submarine melting to warm water. An increase in fjord heat content can be driven by an increase in AW temperature or by an increase in the relative concentration of warm AW to cold PW. We find that the vertically-averaged temperature of the fjord, and thus vertically-averaged thermal forcing, peaks in the fall. The temperature maximum in the fall is a result of both warm warm intruding into the fjord near the surface and seasonally-warmed AW advecting into the fjord at depth (Fig. 8c) and is consistent with observations (Sutherland et al., 2013; Harden et al., 2014). However, we find that the greatest ratio of AW to PW, defined roughly from the height of the 27.3 kg/m^3 isopycnal, occurs in July as a result of relaxing isopycnals. Therefore, these two warming mechanisms have different seasonal patterns. A warming of the Irminger Sea would result in a larger temperature anomaly at depth in fall, while a reduction in along-shelf winds would increase the thickness of the AW layer and result in a larger temperature anomaly in spring or summer. Of course, fjord circulation and its seasonality will modify the amount of oceanic heat that ultimately reaches the glacier. For example, while the temperature remains relatively constant along the fjord, volume transport is not. Consequently, the oceanic heat flux decays if it is shelf-driven but remains nearly constant if it is plume-driven (Fig. 15). The impact of external heat on glaciers will depend on iceberg concentration, the mechanism of fjord heat transport, and processes at the ice-ocean interface, which are still poorly understood.

We would also like to point out that the inclusion of substantial submarine melting (e.g. from icebergs) is likely to change the heat flux interpretation during the summer. In the WG run, the exchange heat flux is negative during the summer as a result of upwelled AW and a shallow outflowing plume (Fig. 8d). If the upper-layer was properly cooled, we would observe a positive heat flux. A steady and positive heat flux would be consistent with observations (Jackson & Straneo, 2016). As the streamfunction shows (Fig. 9d), the plume-driven circulation drives transport between 200 and 500 m all the way towards the glacier, and therefore, increased subglacial discharge should lead to increased heat transport and greater melting of both the terminus and icebergs. Inclusion of melting could then lead to a feedback with an increased buoyancy-driven circulation (Kajanto et al., 2023; Zhao, Stewart, & McWilliams, 2022). To explore this question fully, more realistic melting needs to be included in numerical models (Schulz et al., 2022).

8.2 Relationship Between Glacial Stability and Shelf Forcing

Warmer ocean and atmospheric temperatures have been linked to increased glacial retreat in east Greenland (Straneo et al., 2011; T. R. Cowton et al., 2018). In SF, glacial retreat has also been correlated with the negative phase of the North Atlantic Oscillation (NAO) index (Andresen et al., 2012, 2014), the dominant mode of atmospheric climate variability in the North Atlantic related to pressure differences between Portugal and Iceland. A negative NAO index is associated with increased AW content relative to PW, leading to increased heat transport across the shelf (Christoffersen et al., 2011). The positive phase of the NAO index is correlated with glacial stability despite increased low-pressure systems and storms along the east Greenland coast potentially increasing circulation within fjords (Harden et al., 2011; Andresen et al., 2014). Our model is consistent with this correlation, as we find that under reduced winds (and downwelling), shelf isopycnals flatten and the fjord-shelf exchange promotes an increase in AW. This mechanism has recently been observed on shorter timescales (1-10 days) using satellite observations (Snow et al., n.d.). Therefore, our results extend into the fjords the dynamical connection between large-scale wind variability and heat transport across the shelf

(Christoffersen et al., 2011). We find the seasonality and direction of the along-shelf winds play an important role in setting oceanic thermal forcing of the glacier.

8.3 Implications for Fjord Renewal

While the seasonality of the along-shelf winds play an important role in increasing the heat content in SF, we find that the circulation induced from shelf forcing decays away from the mouth and has a reduced affect closer to the fjord head. In contrast, the plume-driven circulation in summer is capable of driving renewal across the whole length of the fjord. Therefore, we would expect fjord properties (e.g. heat, nutrients) close to the terminus to have the quickest renewal rates in summer when subglacial discharge is strongest. Additionally, near-terminus circulation is an important control of glacial melt rates. In large fjord systems such as Sermilik, the shelf-forced circulation decays limiting the direct effects of storms and shelf winds on submarine melting.

8.4 Fjord Mixing

There appears to be weak mixing in the main channel of Sermilik Fjord. TEF bulk properties of Salinity and Temperature (Sup. Fig. 6 and 7) are nearly constant along the fjord. During the winter, even though CTWs can drive a rapid fluctuation, they might contribute only modestly to mixing. Low dissipation would be consistent with modeling studies focusing on CTWs on Greenland's shelf and fjords (Gelderloos et al., 2021, 2022). During the summer, when the circulation is plume-dominated, the weak mixing indicates that the outgoing flux is primarily set by the subglacial discharge plume parameterization. The addition of icebergs is likely to add additional mixing downfjord and would be consistent with some observations (Muilwijk et al., 2022).

9 Conclusion

Glacial fjords are critical to the climate system by exchanging heat and salt between the ice sheet and open ocean. We analyzed the output from two three-year simulations of a glacial fjord with realistic forcing. One simulation included glacial and shelf forcing (WG) while the other only included shelf forcing (NG), allowing us to identify the relative roles of shelf and plume forcing on shelf-fjord exchange. Using the NG run, we found that the shelf forcing was able to drive significant exchange even in the absence of glacial forcing. Additionally, we found that the sign of the exchange flow is related to the seasonality of the along-shelf wind stress which controls the across-shelf isopycnal gradients. When downwelling winds subside, shelf isopycnals flatten and the fjord fills with warm AW in the summer. In SF, the minimum of the along-shelf wind stress happens to coincide with peak glacial forcing generating two distinct regimes, a shelf-driven circulation in non-summer months with variable heat and salt exchange, and a plume-driven circulation in the summer with a large salt exchange. The plume-driven exchange shows little along-fjord variability and is more effective at renewing tracers than the shelf-driven circulation which peaks at the fjord mouth. Therefore, the direct effect of the shelf-driven circulation on driving melt-rate variability is likely secondary to thermal forcing. Key limitations of this study are a parameterized ice face which produces weak melting outside of the plume and a lack of icebergs which are likely a considerable heat sink in the fjord.

Appendix A Model and Data Comparison

A1 Observational Data

The model runs presented in this paper are some of the first multi-year simulations of a Greenland glacial fjord with realistic atmospheric and oceanic forcing. Evaluation

Table A1. Moored observations and CTDs from 2015 – 2017. Θ is Conservative Temperature, S is absolute salinity, P is pressure, V is velocity.

Label	Instrument	Depth	Deployment Time	Sample Resolution	Variables
CM6	SBE 37 MicroCAT	350 m	August 2013 – August 2016	15 min	Θ,S,P
CM0	SBE 37 MicroCAT	60 m	August 2015 – July 2017	15 min	Θ,S,P
SF4	SBE 37 MicroCAT	400 m	August 2015 – July 2017	15 min	Θ,S,P
SF6	SBE 37 MicroCAT	350 m	August 2015 – July 2017	15 min	Θ,S,P
SF4 ADCP	75 kHz RDI Teledyne Workhorse Long-Ranger ADCP (Upward Facing)	381 – 41 m (10 m bins)	August 2015 – July 2017	30 min	V
OW1 ADCP	75 kHz RDI Teledyne Workhorse Long-Ranger ADCP (Upward Facing)	143 – 18 m (5 m bins)	August 2015 – July 2017	30 min	V
CTD 2015	SBE 25plus MicroCAT	Full Depth	August 2015	1 m	Θ,S,P
CTD 2017	SBE 25plus MicroCAT	Full Depth	July 2017	1 m	Θ,S,P

and comparison of the model against observations is limited to a select number of moorings, although these moorings span different regions of the fjord-shelf system (Fig. 1). We compare the model to three moored Conductivity, Temperature and Depth (CTD) instruments (Table A1) from August 2015 to July 2017 located on the shelf at 350 m and in the fjord at 60 m and 400 m (Fig. 1). We also compare the model output to moored Acoustic Doppler Current Profiler (ADCP) velocity data collected in the fjord and on the shelf (Table A1). We compare the model output to 64 ship-based CTD profiles collected during summer surveys in 2015 and 2017. Lastly, we also include 4 winter XCTD profiles from March 2010 for additional context.

We evaluate the model using the Skill Score (SS, Murphy, 1988) defined as

$$\mathrm{SS} = 1 - \frac{\frac{1}{N}\sum_{i=1}^{i=N}(m_i - o_i)^2}{\frac{1}{N}\sum_{i=1}^{i=N}(o_i - \bar{o})^2} = 1 - \frac{\mathrm{MSE}}{\mathrm{STD_o}}, \tag{A1}$$

where m_i is a model value, o_i is the observation value, the overbar denotes an average, (R)MSE is the (root) mean square error, STD is the standard deviation and there are N paired model and observation points. The SS provides a metric for comparison across different model parameters, such as temperature and salinity, and is a commonly used tool when evaluating realistically forced models (e.g., Sutherland et al., 2011; Ralston et al., 2010; Liu et al., 2009). It can be shown that SS = r^2-VB-MB, where r is the correlation coefficient, VB is the variance bias, and MB is the mean bias (Ralston et al., 2010; Sutherland et al., 2011) and thus the score evaluates the data across multiple dimensions. A SS = 1 indicates perfect agreement between the model and observations, but in general a SS above 0.2 is considered good.

We use r to diagnose the covariance between two variables. The statistical significance of the correlation coefficient is determined using the effective degrees of freedom defined as the e-folding scale of the autocovariance of the observations (Emery & Thomson, 2001; Lindeman et al., 2020).

A2 Model and Observation Comparison

To lend support that the model results are applicable to the real world Sermilik Fjord, we compare the WG model time series to 3 moored CTD instruments. The moored instruments recorded temperature and salinity on the shelf at 350 m and in the fjord at 60 m and 400 m from August 2015 – July 2017. The model boundary conditions were shifted in temperature and salinity to match the mean shelf mooring (CM6). The model appears to do a reasonable job of recreating the seasonal temperature variability in the shallow part of the fjord ($r = 0.85$), but has a significant warm bias and a resulting weak SS. The warm bias in the model PW during the summer was captured by the CTD profiles (Fig. 10), but the model does a better job of capturing the cooler PW temperature in the winter (Fig. A1c). The model is less capable of recreating surface salinity (SS $<$ 0) and misses the large salinity minima which occur in the fall. The deeper moorings, especially the one on the shelf, do a better job of recreating salinity variability and temperature variability capturing both the minima in winter and the maxima in summer. (Table A2, Fig. A1).

We compare the volume transport from the model with the transport calculated from the ADCP (Sup. Fig. 2). Splitting the transport into seasons, the observed transport and standard deviation in the summer months (Jun. – Aug.) is 74 $\pm$ 26 mSv (10^3 m^3/s) and non-summer months (Oct. – May) is 26 $\pm$ 7.7 mSv. The modeled transport is 33 mSv in summer and 36 mSv in the non-summer; both are within 1.6 standard deviations of the observed transport. Although the model transport appears to be underestimating transport in the summer. This underestimate is potentially driven by a lack of iceberg melt which has been shown to increase circulation by at least 10% (Davison et al., 2020).

A3 Summary Statistics

A table of SS, r and MSE are given in Table A2. We don't calculate SS or r scores for the ADCP at SF4 since the observed transport is an estimate and not directly measured. We isolate seasonal from synoptic (1-10 day) forcing by splitting all the data up into two time series: a low-pass time series y_{lp} generated from a 30-day low pass 6th order Butterworth filter and a high-pass time series $y_{\mathrm{hp}} = y - y_{\mathrm{lp}}$ generated from removal of the low-pass series from the original data. Most of the SS are poor, and we can attribute this largely to differences in the MSE. The highest SS are for the deep salinity (SF4 and SF6) where the model was shifted to reduce the mean bias. The skill scores tend to improve when looking at shorter timescales ($<$ 30 days) indicating the model is doing better at capturing wind-driven variability than the larger scale variability, a bias we attribute to lacking iceberg melt.

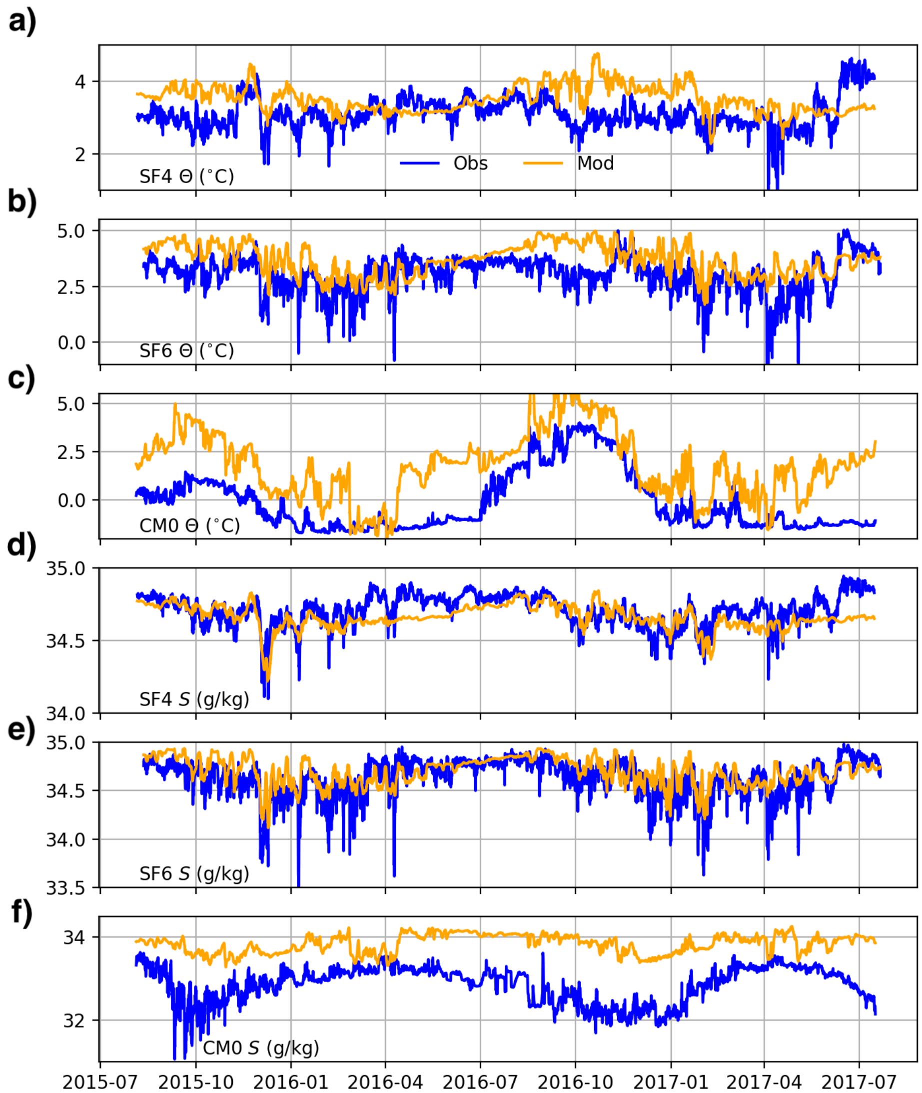

Figure A1. The model output (orange) reproduces shelf observations (blue), but cannot reproduce shallow fjord salinity. a-c) are Conservative Temperature (Θ) at SF4, SF6, and CM0 at 400 m, 350 m, and 60 m respectively. d-f) are Absolute Salinity (S) at SF4, SF6, and CM0.

Table A2. Statistics and skill scores for the mooring temperature, salinity and velocity time series. The first column is the variable and mooring. Columns 2 – 4 are the Skill Score (SS), Mean Square Error (MSE) and correlation coefficient (r) for the low-pass filtered time series, and columns 5 – 7 are statistics for the high-pass filtered time series. Significance is denoted with a star.

Variable	SS_{lp}	MSE_{lp}	r_{lp}	SS_{hp}	MSE_{hp}	r_{hp}
CM0 S	-6.0	1.1	0.42*	-0.13	0.03	0.13
CM0 Θ	-0.95	4.3	0.85*	-2.7	0.26	0.31
SF4 S	0.01	0.01	0.57*	0.12	0.003	0.50*
SF4 Θ	-1.8	0.40	-0.02	-0.33	0.08	0.21
SF6 S	0.33	0.02	0.75*	0.11	0.013	0.48*
SF6 Θ	-0.96	0.83	0.51*	0.05	0.23	0.41*

Open Research Section

We have archived the outputs from the two MITgcm simulations at doi:10.5281/zenodo.8350601. To make file sizes manageable, the outputs have been subset to once per day and the region north of 65.4°N. We are working to make the observational data stored on a public archive and will have this statement revised before publication. We are also working to make code available to reproduce figures from this paper.

Acknowledgments
We acknowledge Margaret Lindeman, Sarah Giddings, and Rebecca Jackson for helpful discussions and suggestions. We thank An Ngyuen for providing ASTE data. RS and FS acknowledge funding from the Heising Simons Foundation.

References

Adcroft, A., Hill, C., Campin, J.-M., Marshall, J., & Heimbach, P. (2004). Overview of the formulation and numerics of the MIT GCM. In *Proceedings of the ecmwf seminar series on numerical methods, recent developments in numerical methods for atmosphere and ocean modelling* (pp. 139–149).

Andresen, C. S., Schmidt, S., Seidenkrantz, M.-S., Straneo, F., Grycel, A., Hass, C. H., ... Kuijpers, A. (2014, August). A 100-year record of changes in water renewal rate in Sermilik fjord and its influence on calving of Helheim glacier, southeast Greenland. *Continental Shelf Research*, *85*, 21–29. doi: 10.1016/j.csr.2014.05.017

Andresen, C. S., Straneo, F., Ribergaard, M. H., Bjørk, A. A., Andersen, T. J., Kuijpers, A., ... Ahlstrøm, A. P. (2012, January). Rapid response of Helheim Glacier in Greenland to climate variability over the past century. *Nature Geoscience*, *5*(1), 37–41. Retrieved 2022-12-19, from `https://www.nature.com/articles/ngeo1349` (Number: 1 Publisher: Nature Publishing Group) doi: 10.1038/ngeo1349

Aure, J., Molvær, J., & Stigebrandt, A. (1996). Observations of inshore water exchange forced by a fluctuating offshore density field. , *33*(1), 112–119. doi: 10.1016/S0025-326X(97)00005-2

Beaird, N., Straneo, F., & Jenkins, W. (2018). Export of Strongly Diluted Greenland Meltwater From a Major Glacial Fjord. *Geophys. Res. Lett.*, *45*, 4163–4170. doi: 10.1029/2018GL077000

Burchard, H., Bolding, K., Feistel, R., Gräwe, U., Klingbeil, K., MacCready, P., ... van der Lee, E. M. (2018, July). The Knudsen theorem and the Total Exchange Flow analysis framework applied to the Baltic Sea. *Progress in Oceanography*, *165*, 268–286. Retrieved 2022-02-23, from `https://www.sciencedirect.com/science/article/pii/S0079661117303774` doi: 10.1016/j.pocean.2018.04.004

Carroll, D., Sutherland, D. A., Curry, B., Nash, J. D., Shroyer, E. L., Catania, G. A., ... Steur, L. d. (2018). Subannual and Seasonal Variability of Atlantic-Origin Waters in Two Adjacent West Greenland Fjords. *J. Geophys. Res. Oceans*, *123*, 6670–6687. doi: 10.1029/2018JC014278

Carroll, D., Sutherland, D. A., Shroyer, E. L., Nash, J. D., Catania, G. A., & Stearns, L. A. (2015). Modeling Turbulent Subglacial Meltwater Plumes: Implications for Fjord-Scale Buoyancy-Driven Circulation. *J. Phys. Oceanogr.*, *45*, 2169–2185. doi: 10.1175/JPO-D-15-0033.1

Carroll, D., Sutherland, D. A., Shroyer, E. L., Nash, J. D., Catania, G. A., & Stearns, L. A. (2017). Subglacial discharge-driven renewal of tidewater glacier fjords. *J. Geophys. Res. Oceans*, *122*, 6611–6629. doi: 10.1002/2017JC012962

Christoffersen, P., Mugford, R. I., Heywood, K. J., Joughin, I., Dowdeswell, J. A., Syvitski, J. P. M., ... Benham, T. J. (2011, September). Warming of waters in an East Greenland fjord prior to glacier retreat: mechanisms and connection to large-scale atmospheric conditions. *The Cryosphere*, *5*(3), 701–714. Retrieved 2020-01-30, from `https://www.the-cryosphere.net/5/701/2011/` doi: https://doi.org/10.5194/tc-5-701-2011

Cowton, T., Slater, D., Sole, A., Goldberg, D., & Nienow, P. (2015). Modeling the impact of glacial runoff on fjord circulation and submarine melt rate using a new subgrid-scale parameterization for glacial plumes. , *120*(2), 796–812. doi: 10.1002/2014JC010324

Cowton, T. R., Sole, A. J., Nienow, P. W., Slater, D. A., & Christoffersen, P. (2018, July). Linear response of east Greenland's tidewater glaciers to ocean/atmosphere warming. *Proceedings of the National Academy of Sciences*, *115*(31), 7907–7912. (Publisher: Proceedings of the National Academy of Sciences) doi: 10.1073/pnas.1801769115

Davison, B. J., Cowton, T. R., Cottier, F. R., & Sole, A. J. (2020, November). Iceberg melting substantially modifies oceanic heat flux towards a major Greenlandic tidewater glacier. *Nat. Commun.*, *11*, 5983. doi: 10.1038/s41467-020-19805-7

Emery, W. J., & Thomson, R. E. (2001). *Data analysis methods in physical oceanography (revised second edition)* (Revised Second Edition ed.). Amsterdam: Elsevier Science. doi: https://doi.org/10.1016/B978-044450756-3/50007-1

Enderlin, E. M., Howat, I. M., Jeong, S., Noh, M.-J., Angelen, J. H. v., & Broeke, M. R. v. d. (2014). An improved mass budget for the Greenland ice sheet. *Geophys. Res. Lett.*, *41*, 866–872. doi: 10.1002/2013GL059010

Ezhova, E., Cenedese, C., & Brandt, L. (2017, October). Dynamics of a Turbulent Buoyant Plume in a Stratified Fluid: An Idealized Model of Subglacial Discharge in Greenland Fjords. *J. Phys. Oceanogr.*, *47*, 2611–2630. doi: 10.1175/JPO-D-16-0259.1

Fraser, N. J., & Inall, M. E. (2018). Influence of barrier wind forcing on heat delivery toward the Greenland ice sheet. *J. Geophys. Res. Oceans*, *123*, 2513–2538. doi: 10.1002/2017JC013464

Fraser, N. J., Inall, M. E., Magaldi, M. G., Haine, T. W. N., & Jones, S. C. (2018). Wintertime fjord-shelf interaction and ice sheet melting in southeast greenland. , *123*(12), 9156–9177. doi: 10.1029/2018JC014435

Gelderloos, R., Haine, T. W. N., & Almansi, M. (2021, March). Coastal Trapped Waves and Other Subinertial Variability along the Southeast Greenland Coast in a Realistic Numerical Simulation. *Journal of Physical Oceanography*, *51*(3), 861–877. Retrieved 2022-02-28, from `https://journals.ametsoc.org/view/journals/phoc/51/3/JPO-D-20-0239.1.xml` (Publisher: American Meteorological Society Section: Journal of Physical Oceanography) doi: 10.1175/JPO-D-20-0239.1

Gelderloos, R., Haine, T. W. N., & Almansi, M. (2022). Subinertial Variability in Four Southeast Greenland Fjords in Realistic Numerical Simulations. *Journal of Geophysical Research: Oceans*, *127*(11), e2022JC018820. Retrieved 2023-01-13, from `https://onlinelibrary.wiley.com/doi/abs/10.1029/2022JC018820` (_eprint: https://onlinelibrary.wiley.com/doi/pdf/10.1029/2022JC018820) doi: 10.1029/2022JC018820

Gelderloos, R., Haine, T. W. N., Koszalka, I. M., & Magaldi, M. G. (2017, July). Seasonal Variability in Warm-Water Inflow toward Kangerdlugssuaq Fjord. *Journal of Physical Oceanography*, *47*(7), 1685–1699. Retrieved 2023-01-13, from `https://journals.ametsoc.org/view/journals/phoc/47/7/jpo-d-16-0202.1.xml` (Publisher: American Meteorological Society Section: Journal of Physical Oceanography) doi: 10.1175/JPO-D-16-0202.1

Gladish, C. V., Holland, D. M., & Lee, C. M. (2014). Oceanic boundary conditions for jakobshavn glacier. part II: Provenance and sources of variability of disko bay and ilulissat icefjord waters, 1990–2011. , *45*(1), 33–63. doi: 10.1175/JPO-D-14-0045.1

Gladish, C. V., Holland, D. M., Rosing-Asvid, A., Behrens, J. W., & Boje, J. (2014). Oceanic boundary conditions for Jakobshavn Glacier. Part I: Variability and renewal of Ilulissat Icefjord Waters, 2001–14. *J. Phys. Oceanogr.*, *45*, 3–32. doi: 10.1175/JPO-D-14-0044.1

Griffies, S. M., & Hallberg, R. W. (2000, August). Biharmonic Friction with a Smagorinsky-Like Viscosity for Use in Large-Scale Eddy-Permitting Ocean Models. *Monthly Weather Review*, *128*(8), 2935–2946. Retrieved 2023-08-30, from `https://journals.ametsoc.org/view/journals/mwre/128/8/1520-0493_2000_128_2935_bfwasl_2.0.co_2.xml` (Publisher: American Meteorological Society Section: Monthly Weather Review) doi: 10.1175/1520-0493(2000)128⟨2935:BFWASL⟩2.0.CO;2

Hager, A. O., Sutherland, D. A., Amundson, J. M., Jackson, R. H., Kienholz, C., Motyka, R. J., & Nash, J. D. (2022). Subglacial discharge reflux and buoyancy forcing drive seasonality in a silled glacial fjord. *J. Geophys. Res. Oceans*, *127*. doi: 10.1029/2021JC018355

Harden, B. E., Renfrew, I. A., & Petersen, G. N. (2011). A climatology of wintertime barrier winds off southeast greenland. , *24*(17), 4701–4717. doi: 10.1175/2011JCLI4113.1

Harden, B. E., Straneo, F., & Sutherland, D. A. (2014). Moored observations of synoptic and seasonal variability in the East Greenland Coastal Current. *J. Geophys. Res. Oceans*, *119*, 8838–8857. doi: 10.1002/2014JC010134

Hersbach, H., Bell, B., Berrisford, P., Hirahara, S., Horányi, A., Muñoz-Sabater, J., ... Thépaut, J.-N. (2020). The ERA5 global reanalysis. *Q. J. R. Meteorol. Soc.*, *146*, 1999-2049. doi: 10.1002/qj.3803

Holland, D. M., Thomas, R. H., de Young, B., Ribergaard, M. H., & Lyberth, B. (2008, October). Acceleration of Jakobshavn Isbræ triggered by warm subsurface ocean waters. *Nat. Geosci.*, *1*, 659-664. doi: 10.1038/ngeo316

Hopwood, M. J., Carroll, D., Dunse, T., Hodson, A., Holding, J. M., Iriarte, J. L., ... Meire, L. (2020, April). Review article: How does glacier discharge affect marine biogeochemistry and primary production in the Arctic? *Cryosphere*, *14*, 1347–1383. doi: 10.5194/tc-14-1347-2020

Howat, I. M., Joughin, I., Tulaczyk, S., & Gogineni, S. (2005). Rapid retreat and acceleration of Helheim Glacier, east Greenland. *Geophysical Research Letters*, *32*(22). Retrieved 2023-01-13, from `https://onlinelibrary.wiley.com/doi/abs/10.1029/2005GL024737` (_eprint: https://onlinelibrary.wiley.com/doi/pdf/10.1029/2005GL024737) doi: 10.1029/2005GL024737

Hughes, K. G. (2022). Pathways, Form Drag, and Turbulence in Simulations of an Ocean Flowing Through an Ice Mélange. *Journal of Geophysical Research: Oceans*, *127*(6), e2021JC018228. (_eprint: https://onlinelibrary.wiley.com/doi/pdf/10.1029/2021JC018228) doi: 10.1029/2021JC018228

Hughes, K. G., Klymak, J. M., Williams, W. J., & Melling, H. (2018). Tidally Modulated Internal Hydraulic Flow and Energetics in the Central Canadian Arctic Archipelago. *Journal of Geophysical Research: Oceans*, *123*(8), 5210–5229. doi: https://doi.org/10.1029/2018JC013770

Inall, M. E., Nilsen, F., Cottier, F. R., & Daae, R. (2015). Shelf/fjord exchange driven by coastal-trapped waves in the arctic. , *120*(12), 8283–8303. doi: 10.1002/2015JC011277

Jackett, D. R., & Mcdougall, T. J. (1995). Minimal Adjustment of Hydrographic Profiles to Achieve Static Stability. *Journal of Atmospheric and Oceanic Technology*, *12*(2), 381–389. doi: 10.1175/1520-0426(1995)012⟨0381:MAOHPT⟩2.0.CO;2

Jackson, R. H., Lentz, S. J., & Straneo, F. (2018). The Dynamics of Shelf Forcing in Greenlandic Fjords. *J. Phys. Oceanogr.*, *48*, 2799–2827. doi: 10.1175/JPO-D-18-0057.1

Jackson, R. H., Motyka, R. J., Amundson, J. M., Abib, N., Sutherland, D. A., Nash, J. D., & Kienholz, C. (2022). The relationship between submarine melt and subglacial discharge from observations at a tidewater glacier. *J. Geophys. Res. Oceans*, *127*, e2021JC018204. doi: 10.1029/2021JC018204

Jackson, R. H., Nash, J. D., Kienholz, C., Sutherland, D. A., Amundson, J. M., ka, R. J., ... Pettit, E. C. (2020). Meltwater intrusions reveal mechanisms for rapid submarine melt at a tidewater glacier. *Geophys. Res. Lett.*, *47*, e2019GL085335. doi: 10.1029/2019GL085335

Jackson, R. H., & Straneo, F. (2016). Heat, Salt, and Freshwater Budgets for a Glacial Fjord in Greenland. *J. Phys. Oceanogr.*, *46*, 2735–2768. doi: 10.1175/JPO-D-15-0134.1

Jackson, R. H., Straneo, F., & Sutherland, D. A. (2014). Externally forced fluctuations in ocean temperature at Greenland glaciers in non-summer months. *Nat. Geosci.*, *7*, 503–508. doi: 10.1038/ngeo2186

Jenkins, A. (2011). Convection-Driven Melting near the Grounding Lines of Ice Shelves and Tidewater Glaciers. *J. Phys. Oceanogr.*, *41*, 2279–2294. doi: 10.1175/JPO-D-11-03.1

Kajanto, K., Straneo, F., & Nisancioglu, K. (2023, January). Impact of icebergs on the seasonal submarine melt of Sermeq Kujalleq. *The Cryosphere*, *17*(1), 371–390. Retrieved 2023-09-15, from `https://tc.copernicus.org/articles/17/371/2023/` (Publisher: Copernicus GmbH) doi: 10.5194/tc-17-371-2023

Khazendar, A., Fenty, I. G., Carroll, D., Gardner, A., Lee, C. M., Fukumori, I., ... Willis, J. (2019). Interruption of two decades of Jakobshavn Isbrae acceleration and thinning as regional ocean cools. *Nat. Geosci.*, *12*, 277–283. doi: 10.1038/s41561-019-0329-3

Kimura, S., Holland, P. R., Jenkins, A., & Piggott, M. (2014, December). The Effect of Meltwater Plumes on the Melting of a Vertical Glacier Face. *Journal of Physical Oceanography*, *44*(12), 3099–3117. Retrieved 2023-01-13, from `https://journals.ametsoc.org/view/journals/phoc/44/12/jpo-d-13-0219.1.xml` (Publisher: American Meteorological Society Section: Journal of Physical Oceanography) doi: 10.1175/JPO-D-13-0219.1

Klinck, J. M., O'Brien, J. J., & Svendsen, H. (1981, December). A Simple Model of Fjord and Coastal Circulation Interaction. *Journal of Physical Oceanography*, *11*(12), 1612–1626. (Publisher: American Meteorological Society Section: Journal of Physical Oceanography) doi: 10.1175/1520-0485(1981)011⟨1612:ASMOFA⟩2.0.CO;2

Large, W. G., McWilliams, J. C., & Doney, S. C. (1994). Oceanic vertical mixing: A review and a model with a nonlocal boundary layer parameterization. *Rev. Geophys.*, *32*, 363-403. doi: 10.1029/94RG01872

Lindeman, M. R., Straneo, F., Wilson, N. J., Toole, J. M., Krishfield, R. A., Beaird, N. L., ... Schaffer, J. (2020). Ocean Circulation and Variability Beneath Nioghalvfjerdsbræ (79 North Glacier) Ice Tongue. *J. Geophys. Res. Oceans*, *125*, e2020JC016091. doi: 10.1029/2020JC016091

Liu, Y., MacCready, P., Hickey, B. M., Dever, E. P., Kosro, P. M., & Banas, N. S. (2009). Evaluation of a coastal ocean circulation model for the Columbia River plume in summer 2004. *Journal of Geophysical Research: Oceans*, *114*(C2). Retrieved 2022-11-18, from `https://onlinelibrary.wiley.com/doi/abs/10.1029/2008JC004929` (_eprint: https://onlinelibrary.wiley.com/doi/pdf/10.1029/2008JC004929) doi: 10.1029/2008JC004929

Lorenz, M., Klingbeil, K., & Burchard, H. (2020). Numerical Study of the Exchange Flow of the Persian Gulf Using an Extended

Total Exchange Flow Analysis Framework. *Journal of Geophysical Research: Oceans*, *125*(2), e2019JC015527. (_eprint: https://agupubs.onlinelibrary.wiley.com/doi/pdf/10.1029/2019JC015527) doi: 10.1029/2019JC015527

Lorenz, M., Klingbeil, K., MacCready, P., & Burchard, H. (2019, May). Numerical issues of the Total Exchange Flow (TEF) analysis framework for quantifying estuarine circulation. *Ocean Science*, *15*(3), 601–614. Retrieved 2022-10-18, from `https://os.copernicus.org/articles/15/601/2019/` (Publisher: Copernicus GmbH) doi: 10.5194/os-15-601-2019

Luckman, A., Murray, T., de Lange, R., & Hanna, E. (2006). Rapid and synchronous ice-dynamic changes in East Greenland. *Geophysical Research Letters*, *33*(3). Retrieved 2023-01-13, from `https://onlinelibrary.wiley.com/doi/abs/10.1029/2005GL025428` (_eprint: https://onlinelibrary.wiley.com/doi/pdf/10.1029/2005GL025428) doi: 10.1029/2005GL025428

MacCready, P. (2011, June). Calculating Estuarine Exchange Flow Using Isohaline Coordinates. *Journal of Physical Oceanography*, *41*(6), 1116–1124. Retrieved 2023-01-14, from `https://journals.ametsoc.org/view/journals/phoc/41/6/2011jpo4517.1.xml` (Publisher: American Meteorological Society Section: Journal of Physical Oceanography) doi: 10.1175/2011JPO4517.1

MacCready, P., & Geyer, W. R. (2010). Advances in Estuarine Physics. *Annu. Rev. Mar. Sci.*, *2*, 35–58. doi: 10.1146/annurev-marine-120308-081015

MacCready, P., Geyer, W. R., & Burchard, H. (2018, June). Estuarine Exchange Flow Is Related to Mixing through the Salinity Variance Budget. *Journal of Physical Oceanography*, *48*(6), 1375–1384. Retrieved 2023-01-14, from `https://journals.ametsoc.org/view/journals/phoc/48/6/jpo-d-17-0266.1.xml` (Publisher: American Meteorological Society Section: Journal of Physical Oceanography) doi: 10.1175/JPO-D-17-0266.1

Mankoff, K. D., Solgaard, A., Colgan, W., Ahlstrøm, A. P., Khan, S. A., & Fausto, R. S. (2020, June). Greenland Ice Sheet solid ice discharge from 1986 through March 2020. *Earth System Science Data*, *12*(2), 1367–1383. Retrieved 2023-01-13, from `https://essd.copernicus.org/articles/12/1367/2020/` (Publisher: Copernicus GmbH) doi: 10.5194/essd-12-1367-2020

Mankoff, K. D., Straneo, F., Cenedese, C., Das, S. B., Richards, C. G., & Singh, H. (2016). Structure and dynamics of a subglacial discharge plume in a greenlandic fjord. *J. Geophys. Res.: Oceans*, *121*, 8670–8688. doi: 10.1002/2016JC011764

Marshall, J., Adcroft, A., Hill, C., Perelman, L., & Heisey, C. (1997). A finite-volume, incompressible Navier Stokes model for studies of the ocean on parallel computers. *J. Geophys. Res.*, *102*, 5753–5766. doi: 10.1029/96JC02775

Moffat, C. (2014). Wind-driven modulation of warm water supply to a proglacial fjord, jorge montt glacier, patagonia. , *41*(11), 3943–3950. doi: 10.1002/2014GL060071

Moon, T., Sutherland, D. A., Carroll, D., Felikson, D., Kehrl, L., & Straneo, F. (2018, January). Subsurface iceberg melt key to Greenland fjord freshwater budget. *Nat. Geosci.*, *11*, 49–54. doi: 10.1038/s41561-017-0018-z

Morlighem, M., Williams, C. N., Rignot, E., An, L., Arndt, J. E., Bamber, J. L., ... Zinglersen, K. B. (2017). BedMachine v3: Complete bed topography and ocean bathymetry mapping of Greenland from multibeam echo sounding combined with mass conservation. *Geophys. Res. Lett.*, *44*, 11051-11061. doi: 10.1002/2017GL074954

Mortensen, J., Bendtsen, J., Lennert, K., & Rysgaard, S. (2014). Seasonal variability of the circulation system in a west Greenland tidewater outlet glacier fjord, Godthåbsfjord (64°N). *J. Geophys. Res. Earth Surf.*, *119*, 2591–2603. doi: 10.1002/2014JF003267

Mortensen, J., Lennert, K., Bendtsen, J., & Rysgaard, S. (2011). Heat sources for glacial melt in a sub-arctic fjord (godthåbsfjord) in contact with the greenland ice sheet. , *116*. doi: 10.1029/2010JC006528

Mortensen, J., Rysgaard, S., Arendt, K. E., Juul-Pedersen, T., Søgaard, D. H., Bendtsen, J., & Meire, L. (2018). Local Coastal Water Masses Control Heat Levels in a West Greenland Tidewater Outlet Glacier Fjord. *J. Geophys. Res. Oceans*, *123*. doi: 10.1029/2018JC014549

Mouginot, J., Rignot, E., Bjørk, A. A., van den Broeke, M., Millan, R., Morlighem, M., ... Wood, M. (2019). Forty-six years of Greenland Ice Sheet mass balance from 1972 to 2018. *Proc. Natl. Acad. Sci.*, *116*, 9239-44. doi: https://doi.org/10.1073/pnas.1904242116

Muilwijk, M., Straneo, F., Slater, D. A., Smedsrud, L. H., Holte, J., Wood, M., ... Harden, B. (2022, March). Export of Ice Sheet Meltwater from Upernavik Fjord, West Greenland. *J. Phys. Oceanogr.*, *52*, 363–382. doi: 10.1175/JPO-D-21-0084.1

Murphy, A. H. (1988, December). Skill Scores Based on the Mean Square Error and Their Relationships to the Correlation Coefficient. *Monthly Weather Review*, *116*(12), 2417–2424. Retrieved 2023-09-06, from `https://journals.ametsoc.org/view/journals/mwre/116/12/1520-0493_1988_116_2417_ssbotm_2_0_co_2.xml` (Publisher: American Meteorological Society Section: Monthly Weather Review) doi: 10.1175/1520-0493(1988)116⟨2417:SSBOTM⟩2.0.CO;2

Nguyen, A. T., Pillar, H., Ocaña, V., Bigdeli, A., Smith, T. A., & Heimbach, P. (2021). The Arctic Subpolar Gyre sTate Estimate: Description and assessment of a data-constrained, dynamically consistent ocean-sea ice estimate for 2002–2017. *J. Adv. Model. Earth Syst.*, *13*, e2020MS002398. doi: 10.1029/2020MS002398

Ralston, D. K., Geyer, W. R., & Lerczak, J. A. (2010). Structure, variability, and salt flux in a strongly forced salt wedge estuary. *Journal of Geophysical Research: Oceans*, *115*(C6). Retrieved 2023-08-24, from `https://onlinelibrary.wiley.com/doi/abs/10.1029/2009JC005806` (_eprint: https://onlinelibrary.wiley.com/doi/pdf/10.1029/2009JC005806) doi: 10.1029/2009JC005806

Rysgaard, S., Vang, T., Stjernholm, M., Rasmussen, B., Windelin, A., & Kiilsholm, S. (2003, August). Physical Conditions, Carbon Transport, and Climate Change Impacts in a Northeast Greenland Fjord. *Arctic, Antarctic, and Alpine Research*, *35*(3), 301–312. (Publisher: Taylor & Francis _eprint: https://www.tandfonline.com/doi/pdf/10.1657/1523-0430%282003%29035%5B0301%3APCCTAC%5D2.0.CO%3B2) doi: 10.1657/1523-0430(2003)035[0301:PCCTAC]2.0.CO;2

Sanchez, R., Slater, D., & Straneo, F. (2023). Delayed Freshwater Export from a Greenland tidewater glacial fjord. *Journal of Physical Oceanography*, *-1*(aop). doi: 10.1175/JPO-D-22-0137.1

Sanchez, R., Straneo, F., & Andres, M. (2021, September). Using Acoustic Travel Time to Monitor the Heat Variability of Glacial Fjords. *Journal of Atmospheric and Oceanic Technology*, *38*(9), 1535–1550. Retrieved 2022-02-15, from `https://journals.ametsoc.org/view/journals/atot/38/9/JTECH-D-20-0176.1.xml` (Publisher: American Meteorological Society Section: Journal of Atmospheric and Oceanic Technology) doi: 10.1175/JTECH-D-20-0176.1

Schaffer, J., Kanzow, T., von Appen, W.-J., von Albedyll, L., Arndt, J. E., & Roberts, D. H. (2020). Bathymetry constrains ocean heat supply to greenland's largest glacier tongue. , *13*(3), 227–231. doi: 10.1038/s41561-019-0529-x

Schulz, K., Nguyen, A. T., & Pillar, H. R. (2022). An improved and observationally-constrained melt rate parameterization for vertical ice fronts of marine terminating glaciers. *Geophys. Res. Lett.*, *49*, e2022GL100654. doi: 10.1029/2022GL100654

Sciascia, R., Straneo, F., Cenedese, C., & Heimbach, P. (2013). Seasonal variability of submarine melt rate and circulation in an East Greenland fjord. *J. Geophys. Res. Oceans*, *118*, 2492-2506. doi: 10.1002/jgrc.20142

Shroyer, E. L., Padman, L., Samelson, R. M., Münchow, A., & Stearns, L. A. (2017, April). Seasonal control of Petermann Gletscher ice-shelf melt by the ocean's response to sea-ice cover in Nares Strait. *Journal of Glaciology*, *63*(238), 324–330. (Publisher: Cambridge University Press) doi: 10.1017/jog.2016.140

Slater, D. A., Carroll, D., Oliver, H., Hopwood, M. J., Straneo, F., Wood, M., ... Morlighem, M. (2022). Characteristic depths, fluxes, and timescales for Greenland's tidewater glacier fjords from subglacial discharge-driven upwelling during summer. *Geophys. Res. Lett.*, *49*, e2021GL097081. doi: 10.1029/2021GL097081

Slater, D. A., Felikson, D., Straneo, F., Goelzer, H., Little, C. M., Morlighem, M., ... Nowicki, S. (2020). Twenty-first century ocean forcing of the Greenland ice sheet for modelling of sea level contribution. *The Cryosphere*, *14*, 985-1008. doi: 10.5194/tc-14-985-2020

Slater, D. A., & Straneo, F. (2022, October). Submarine melting of glaciers in Greenland amplified by atmospheric warming. *Nature Geoscience*, 1–6. Retrieved 2022-10-04, from `https://www.nature.com/articles/s41561-022-01035-9` (Publisher: Nature Publishing Group) doi: 10.1038/s41561-022-01035-9

Slater, D. A., Straneo, F., Das, S. B., Richards, C. G., Wagner, T. J. W., & Nienow, P. W. (2018). Localized plumes drive front-wide ocean melting of a greenlandic tidewater glacier. *Geophys. Res. Lett.*, *45*, 12,350–12,358. doi: 10.1029/2018GL080763

Snow, T., Straneo, F., Holte, J., Grigsby, S., Abdalati, W., & Scambos, T. (2021). More than Skin Deep: Sea Surface Temperature as a Means of Inferring Atlantic Water Variability on the Southeast Greenland Continental Shelf Near Helheim Glacier. *Journal of Geophysical Research: Oceans*, *126*(4), e2020JC016509. Retrieved 2021-04-30, from `https://agupubs.onlinelibrary.wiley.com/doi/abs/10.1029/2020JC016509` (_eprint: https://agupubs.onlinelibrary.wiley.com/doi/pdf/10.1029/2020JC016509) doi: https://doi.org/10.1029/2020JC016509

Snow, T., Zhang, W., Schreiber, E., Siegfried, M., Abdalati, W., & Scambos, T. (n.d.). Alongshore winds force warm Atlantic Water toward Helheim Glacier in southeast Greenland. *Journal of Geophysical Research: Oceans*, *n/a*(n/a), e2023JC019953. Retrieved 2023-09-14, from `https://onlinelibrary.wiley.com/doi/abs/10.1029/2023JC019953` (_eprint: https://onlinelibrary.wiley.com/doi/pdf/10.1029/2023JC019953) doi: 10.1029/2023JC019953

Straneo, F., & Cenedese, C. (2015). The dynamics of greenland's glacial fjords and their role in climate. *Annu. Rev. Mar. Sci.*, *7*, 89–112. doi: 10.1146/annurev-marine-010213-135133

Straneo, F., Curry, R. G., Sutherland, D. A., Hamilton, G. S., Cenedese, C., Våge, K., & Stearns, L. A. (2011). Impact of fjord dynamics and glacial runoff on the circulation near Helheim Glacier. *Nat. Geosci.*, *4*, 322–327. doi: 10.1038/ngeo1109

Straneo, F., Hamilton, G. S., Sutherland, D. A., Stearns, L. A., Davidson, F., Hammill, M. O., ... Rosing-Asvid, A. (2010). Rapid circulation of warm subtropical waters in a major glacial fjord in east Greenland. *Nat. Geosci.*, *3*, 182–186. doi: 10.1038/ngeo764

Straneo, F., & Heimbach, P. (2013). North Atlantic warming and the retreat of Greenland's outlet glaciers. *Nature*, *504*, 36–43. doi: 10.1038/nature12854

Straneo, F., Sutherland, D. A., Stearns, L., Catania, G., Heimbach, P., Moon, T., ... Meire, L. (2019). The case for a sustained Greenland Ice Sheet-Ocean observing system (GrIOOS). *Front. Mar. Sci.*, *6*. doi: 10.3389/fmars.2019.00138

Stuart-Lee, A. E., Mortensen, J., Kaaden, A.-S. v. d., & Meire, L. (2021). Seasonal Hydrography of Ameralik: A Southwest Greenland Fjord Impacted by a Land-Terminating Glacier. *J.Geophys. Res. Oceans*, *126*, e2021JC017552. doi: 10.1029/2021JC017552

Sundfjord, A., Albretsen, J., Kasajima, Y., Skogseth, R., Kohler, J., Nuth, C., ... Torsvik, T. (2017). Effects of glacier runoff and wind on surface layer dynamics and Atlantic Water exchange in Kongsfjorden, Svalbard; a model study. *Estuarine, Coastal and Shelf Science*, *187*, 260–272. doi: 10.1016/j.ecss.2017.01.015

Sutherland, D. A., MacCready, P., Banas, N. S., & Smedstad, L. F. (2011, June). A Model Study of the Salish Sea Estuarine Circulation. *Journal of Physical Oceanography*, *41*(6), 1125–1143. Retrieved 2023-09-06, from https://journals.ametsoc.org/view/journals/phoc/41/6/2011jpo4540.1.xml (Publisher: American Meteorological Society Section: Journal of Physical Oceanography) doi: 10.1175/2011JPO4540.1

Sutherland, D. A., Straneo, F., Stenson, G. B., Davidson, F. J. M., Hammill, M. O., & Rosing-Asvid, A. (2013). Atlantic water variability on the SE greenland continental shelf and its relationship to SST and bathymetry. , *118*(2), 847–855. doi: 10.1029/2012JC008354

Wood, M., Rignot, E., Fenty, I., An, L., Bjørk, A., van den Broeke, M., ... Zhang, H. (2021). Ocean forcing drives glacier retreat in Greenland. *Sci. Adv.*, *7*, eaba7282. doi: 10.1126/sciadv.aba7282

Wood, M., Rignot, E., Fenty, I., Menemenlis, D., Millan, R., Morlighem, M., ... Seroussi, H. (2018). Ocean-Induced Melt Triggers Glacier Retreat in Northwest Greenland. *Geophysical Research Letters*, *45*(16), 8334–8342. Retrieved 2021-09-08, from https://agupubs.onlinelibrary.wiley.com/doi/abs/10.1029/2018GL078024 (_eprint: https://agupubs.onlinelibrary.wiley.com/doi/pdf/10.1029/2018GL078024) doi: 10.1029/2018GL078024

Xu, Y., Rignot, E., Menemenlis, D., & Koppes, M. (2012). Numerical experiments on subaqueous melting of Greenland tidewater glaciers in response to ocean warming and enhanced subglacial discharge. *Ann. Glaciol.*, *53*, 229-234. doi: 10.3189/2012AoG60A139

Zhao, K. X., Stewart, A. L., & McWilliams, J. C. (2021, April). Geometric Constraints on Glacial Fjord–Shelf Exchange. *J. Phys. Oceanogr.*, *51*, 1223–1246. doi: 10.1175/JPO-D-20-0091.1

Zhao, K. X., Stewart, A. L., & McWilliams, J. C. (2022). Linking Overturning, Recirculation, and Melt in Glacial Fjords. *Geophys. Res. Lett.*, *49*. doi: 10.1029/2021GL095706

Zhao, K. X., Stewart, A. L., McWilliams, J. C., Fenty, I. G., & Rignot, E. J. (2022, November). Standing Eddies in Glacial Fjords and their Role in Fjord Circulation and Melt. *Journal of Physical Oceanography*, *-1*(aop). Retrieved 2023-01-13, from https://journals.ametsoc.org/view/journals/phoc/aop/JPO-D-22-0085.1/JPO-D-22-0085.1.xml (Publisher: American Meteorological Society Section: Journal of Physical Oceanography) doi: 10.1175/JPO-D-22-0085.1

Figure 1.

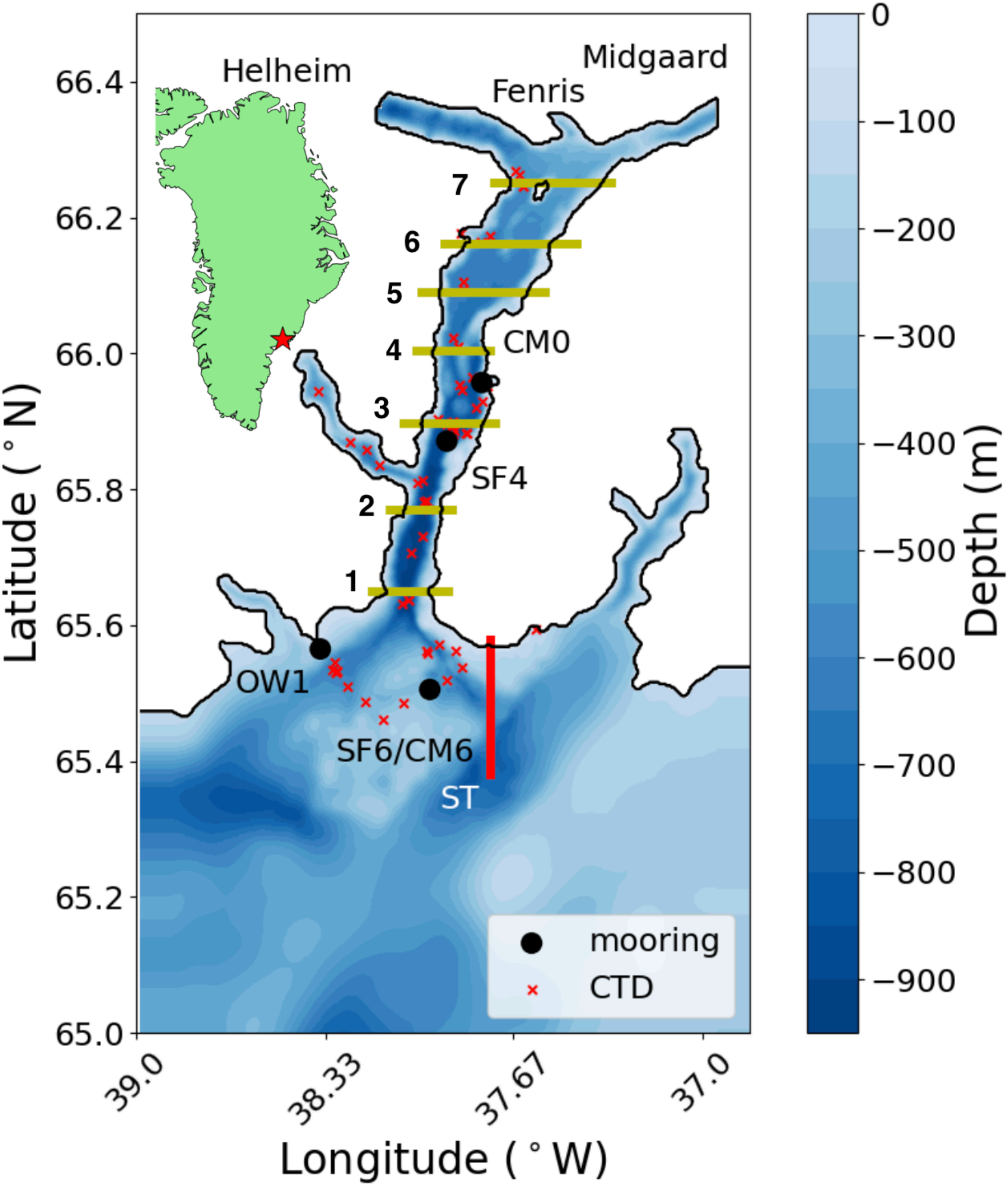

Helheim
Midgaard
Fenris
7
6
5
4
3
2
1
CM0
SF4
OW1
SF6/CM6
ST
mooring
CTD
Latitude (°N)
Longitude (°W)
Depth (m)
66.4
66.2
66.0
65.8
65.6
65.4
65.2
65.0
39.0
38.33
37.67
37.0
0
−100
−200
−300
−400
−500
−600
−700
−800
−900

Figure 2.

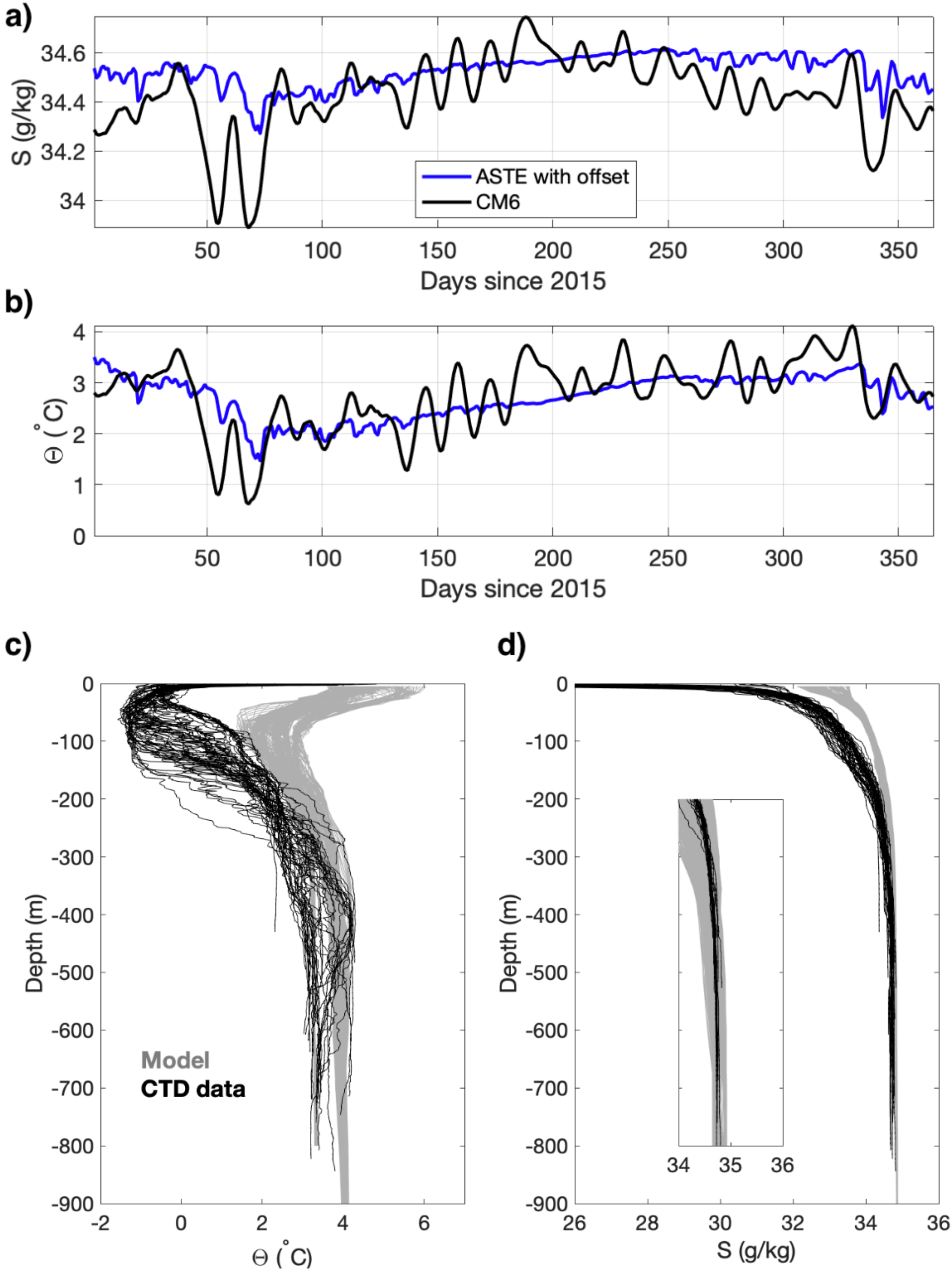

a)
S (g/kg)
ASTE with offset
CM6
Days since 2015
b)
Θ (˚C)
Days since 2015
c)
Depth (m)
Model
CTD data
Θ (˚C)
d)
Depth (m)
S (g/kg)

Figure 3.

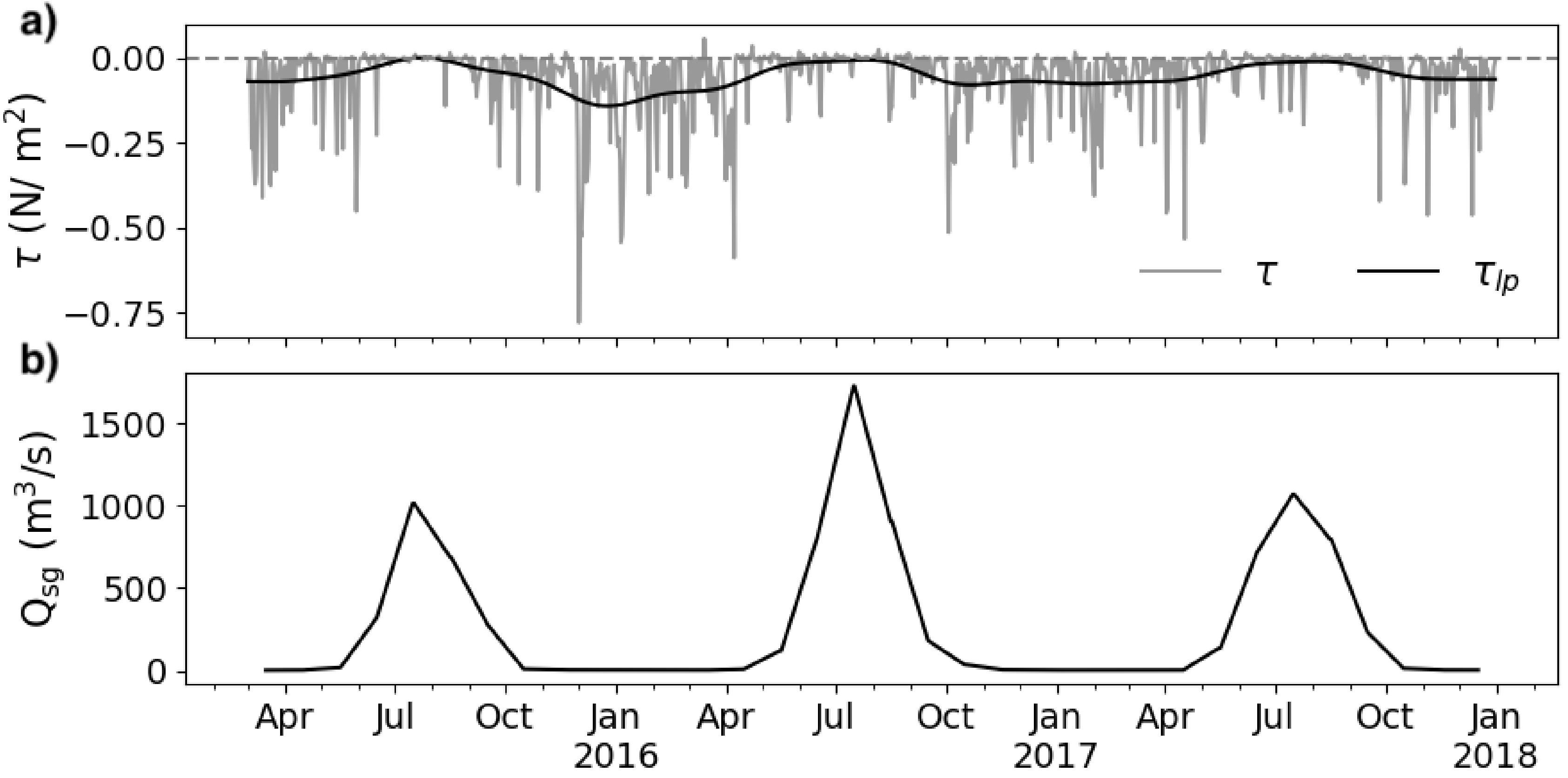
a)
0.00
−0.25
−0.50
−0.75
τ (N/ m2)
τ
τlp
b)
1500
1000
500
0
Qsg (m3/s)
Apr
Jul
Oct
Jan
2016
Apr
Jul
Oct
Jan
2017
Apr
Jul
Oct
Jan
2018

Figure 4.

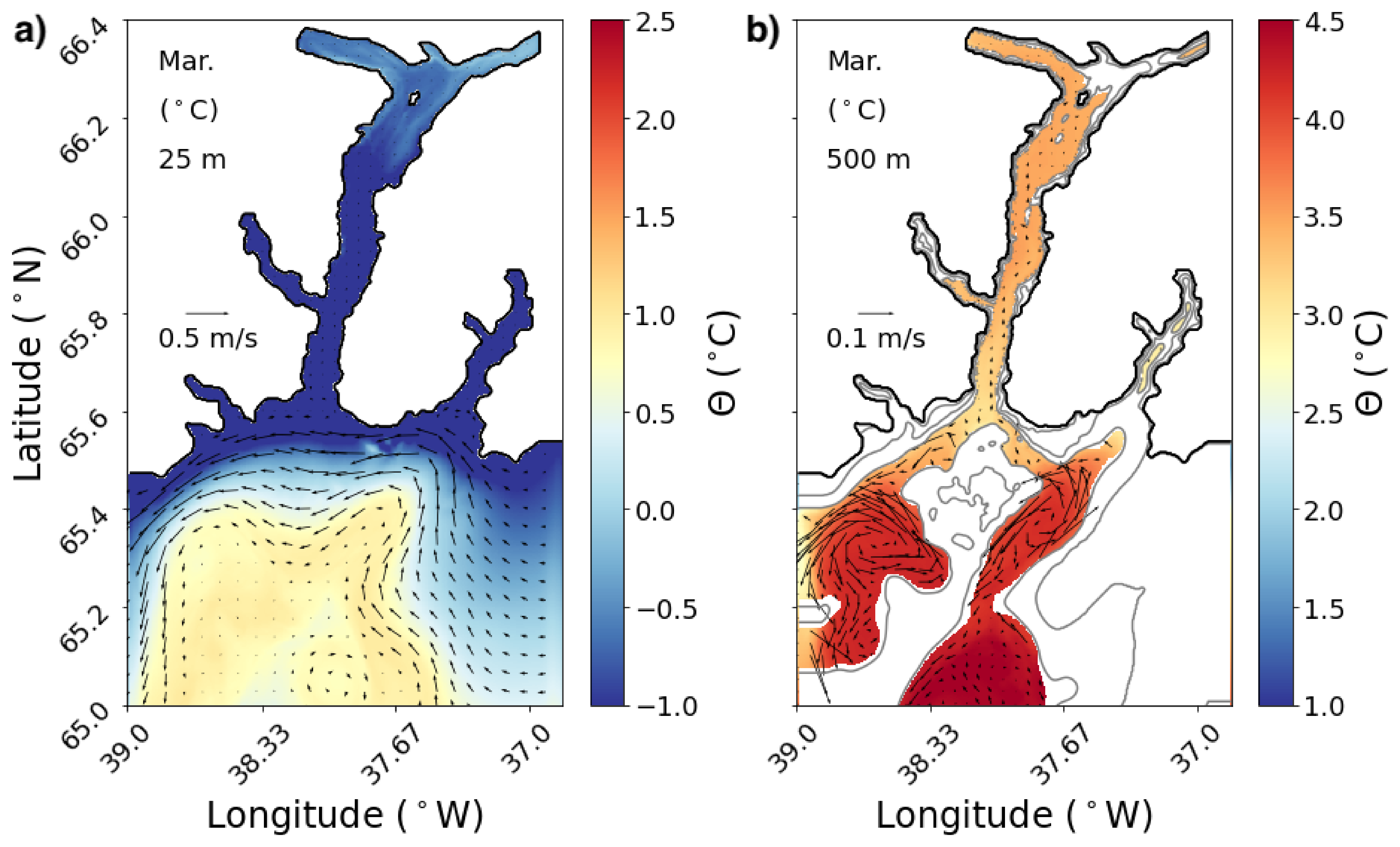

a)
Mar.
(°C)
25 m
0.5 m/s
Latitude (°N)
Longitude (°W)
Θ (°C)
b)
Mar.
(°C)
500 m
0.1 m/s
Longitude (°W)
Θ (°C)

Figure 5.

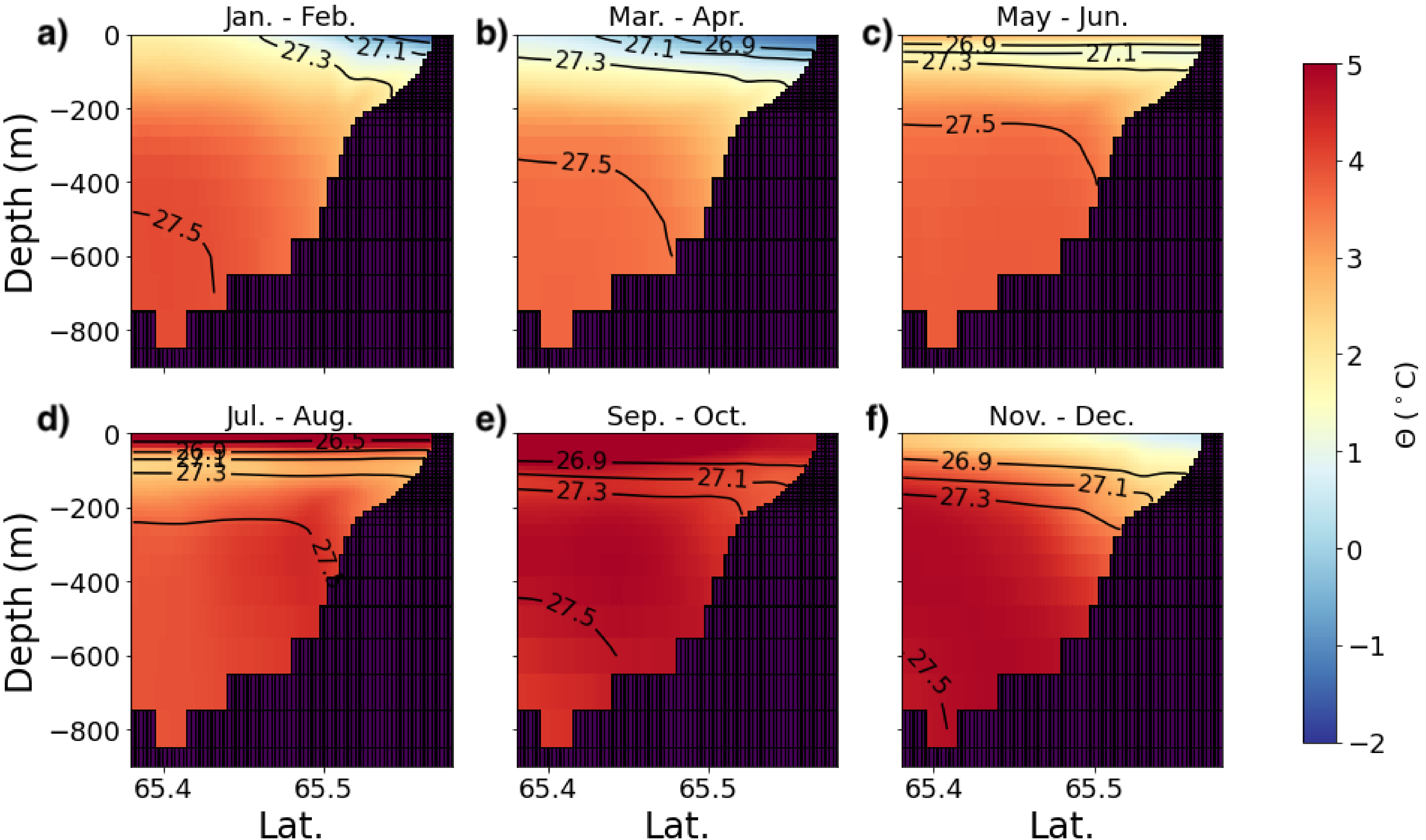
a)
Jan. - Feb.
b)
Mar. - Apr.
c)
May - Jun.
d)
Jul. - Aug.
e)
Sep. - Oct.
f)
Nov. - Dec.
Depth (m)
0
−200
−400
−600
−800
27.1
27.3
27.5
26.9
26.5
65.4
65.5
Lat.
Θ (°C)
5
4
3
2
1
0
−1
−2

Figure 6.

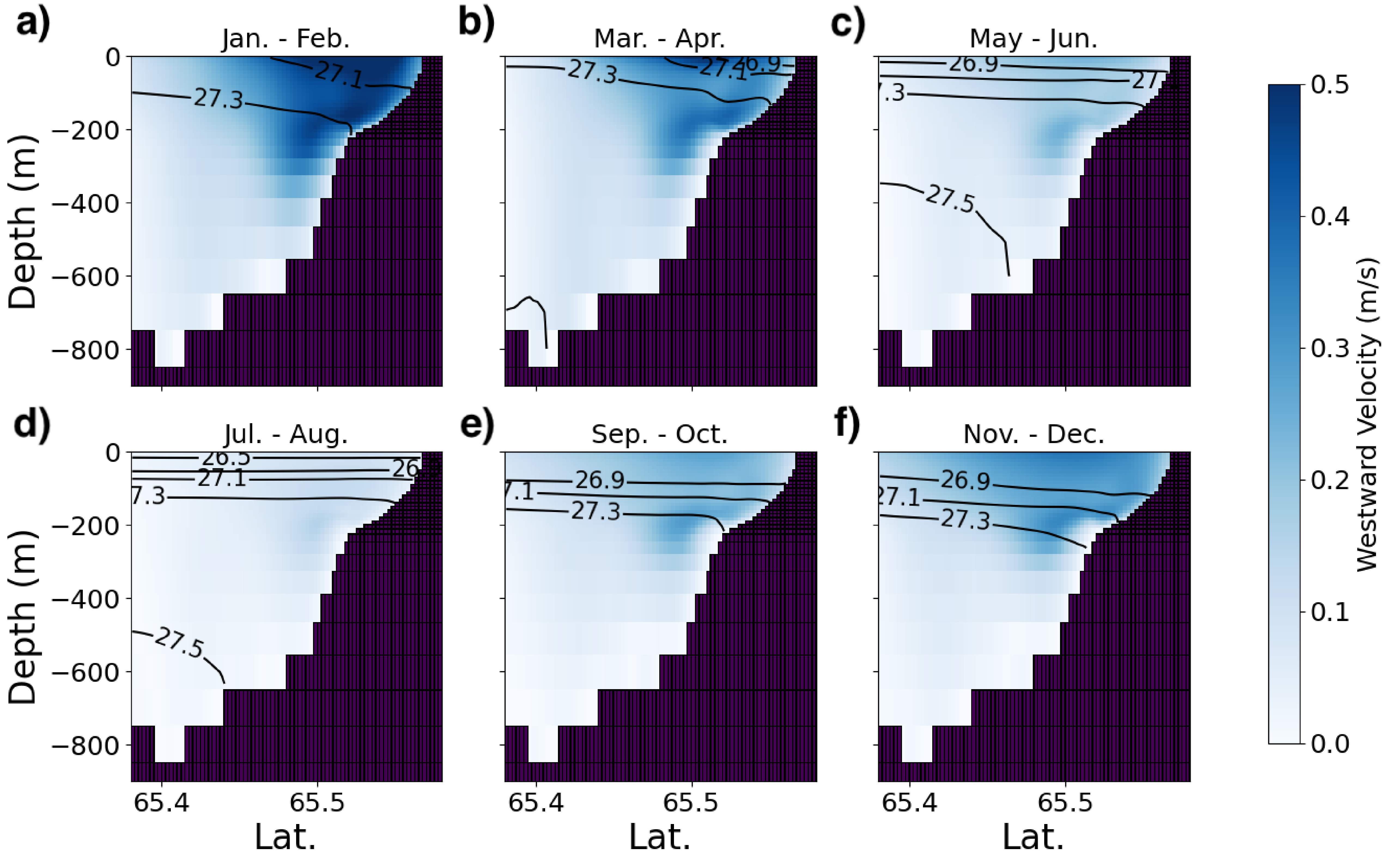

a)
Jan. - Feb.
b)
Mar. - Apr.
c)
May - Jun.
d)
Jul. - Aug.
e)
Sep. - Oct.
f)
Nov. - Dec.
Depth (m)
Lat.
Westward Velocity (m/s)

Figure 7.

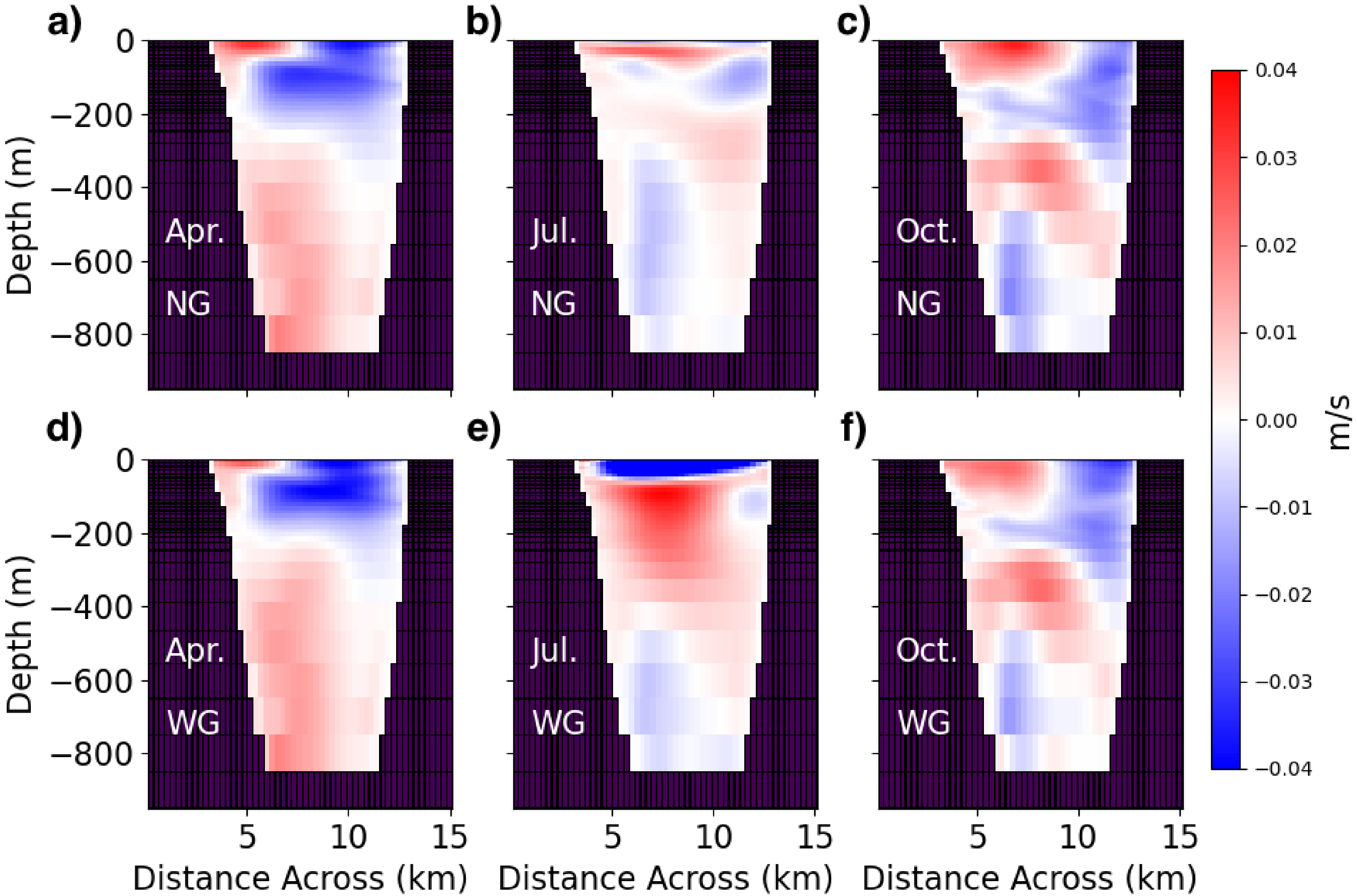

a)
b)
c)
d)
e)
f)
0
−200
−400
−600
−800
Depth (m)
Apr.
NG
Jul.
NG
Oct.
NG
Apr.
WG
Jul.
WG
Oct.
WG
5
10
15
Distance Across (km)
0.04
0.03
0.02
0.01
0.00
−0.01
−0.02
−0.03
−0.04
m/s

Figure 8.

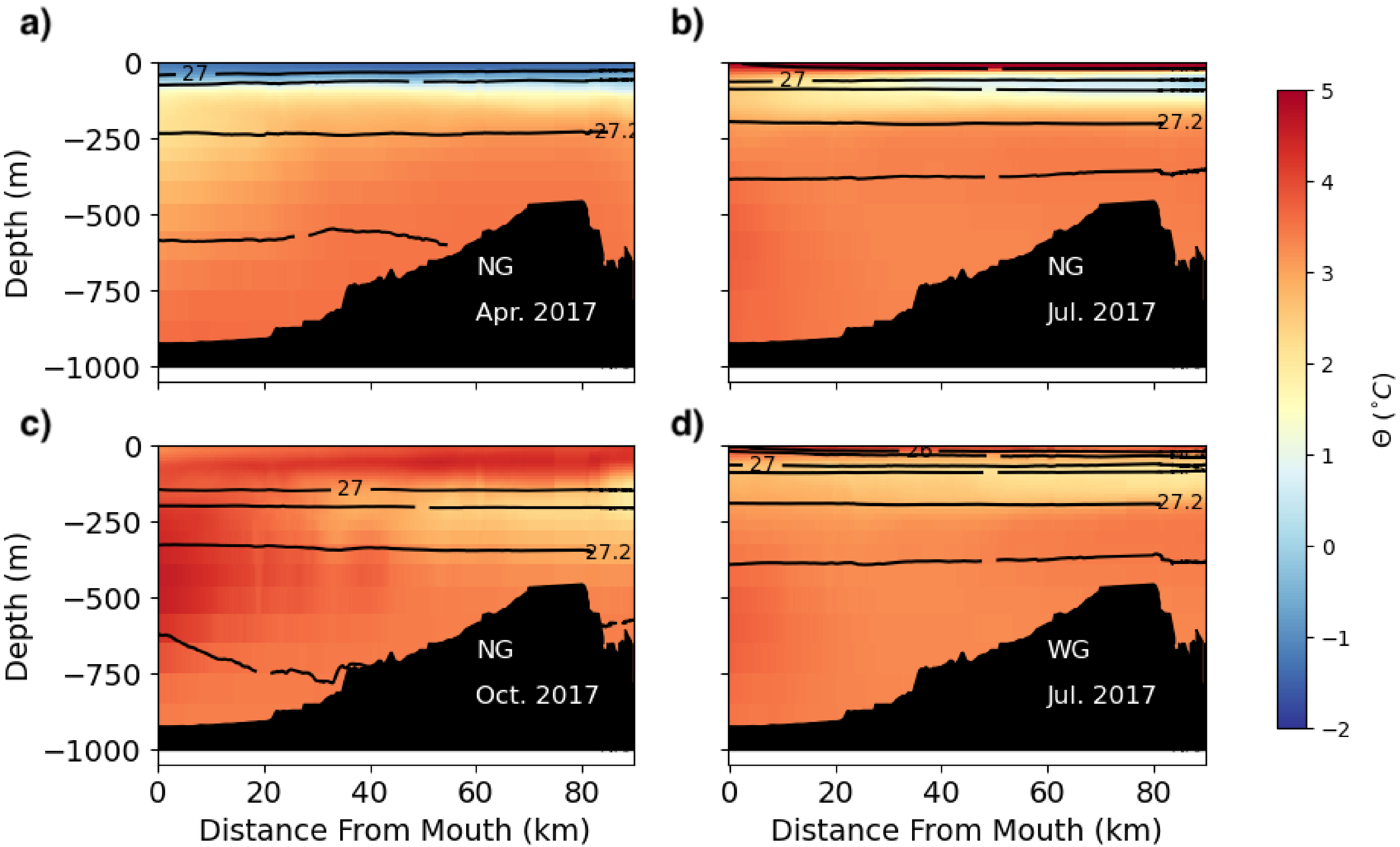

a)
b)
c)
d)
0
−250
−500
−750
−1000
Depth (m)
27
27.2
NG
Apr. 2017
Jul. 2017
Oct. 2017
WG
0
20
40
60
80
Distance From Mouth (km)
Θ (°C)
5
4
3
2
1
0
−1
−2

Figure 9.

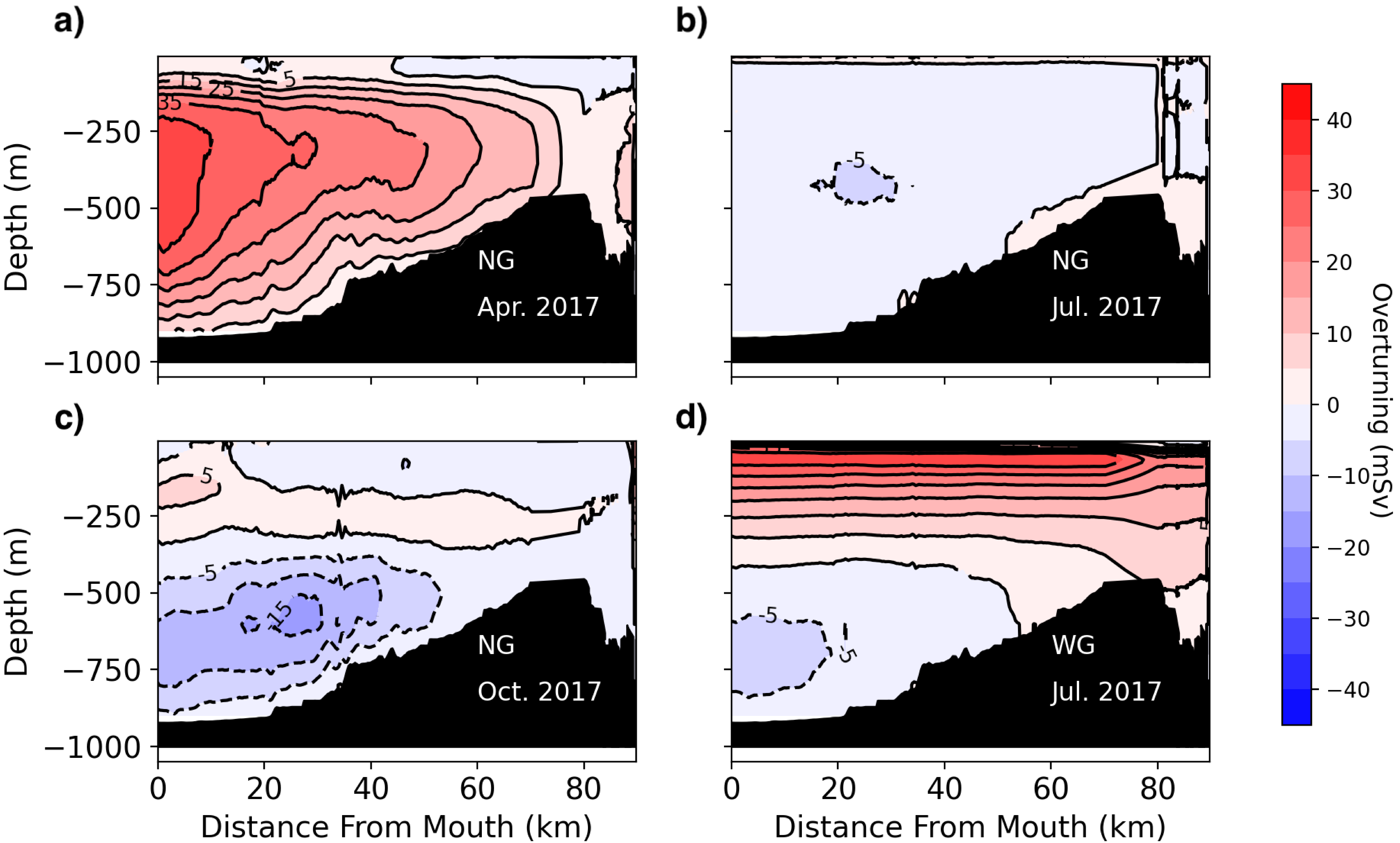

a)
b)
c)
d)
Depth (m)
−250
−500
−750
−1000
NG
Apr. 2017
NG
Jul. 2017
NG
Oct. 2017
WG
Jul. 2017
15
25
35
5
-5
-15
0
20
40
60
80
Distance From Mouth (km)
Overturning (mSv)
40
30
20
10
0
−10
−20
−30
−40

Figure 10.

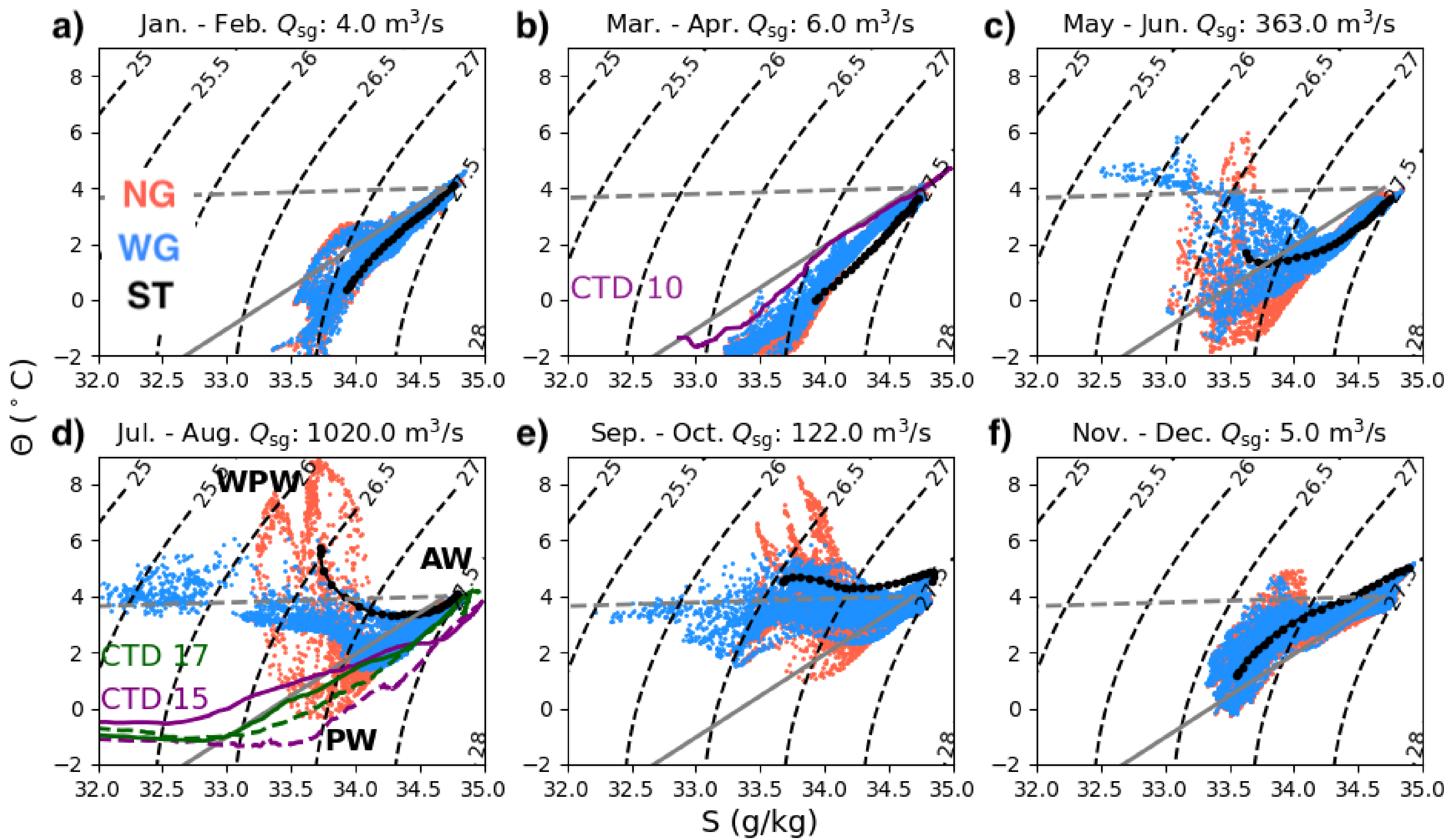

a) Jan. - Feb. Q_{sg}: 4.0 m^3/s
b) Mar. - Apr. Q_{sg}: 6.0 m^3/s
c) May - Jun. Q_{sg}: 363.0 m^3/s
d) Jul. - Aug. Q_{sg}: 1020.0 m^3/s
e) Sep. - Oct. Q_{sg}: 122.0 m^3/s
f) Nov. - Dec. Q_{sg}: 5.0 m^3/s
NG
WG
ST
CTD 10
CTD 17
CTD 15
WPW
AW
PW
Θ ($^\circ$C)
S (g/kg)

Figure 11.

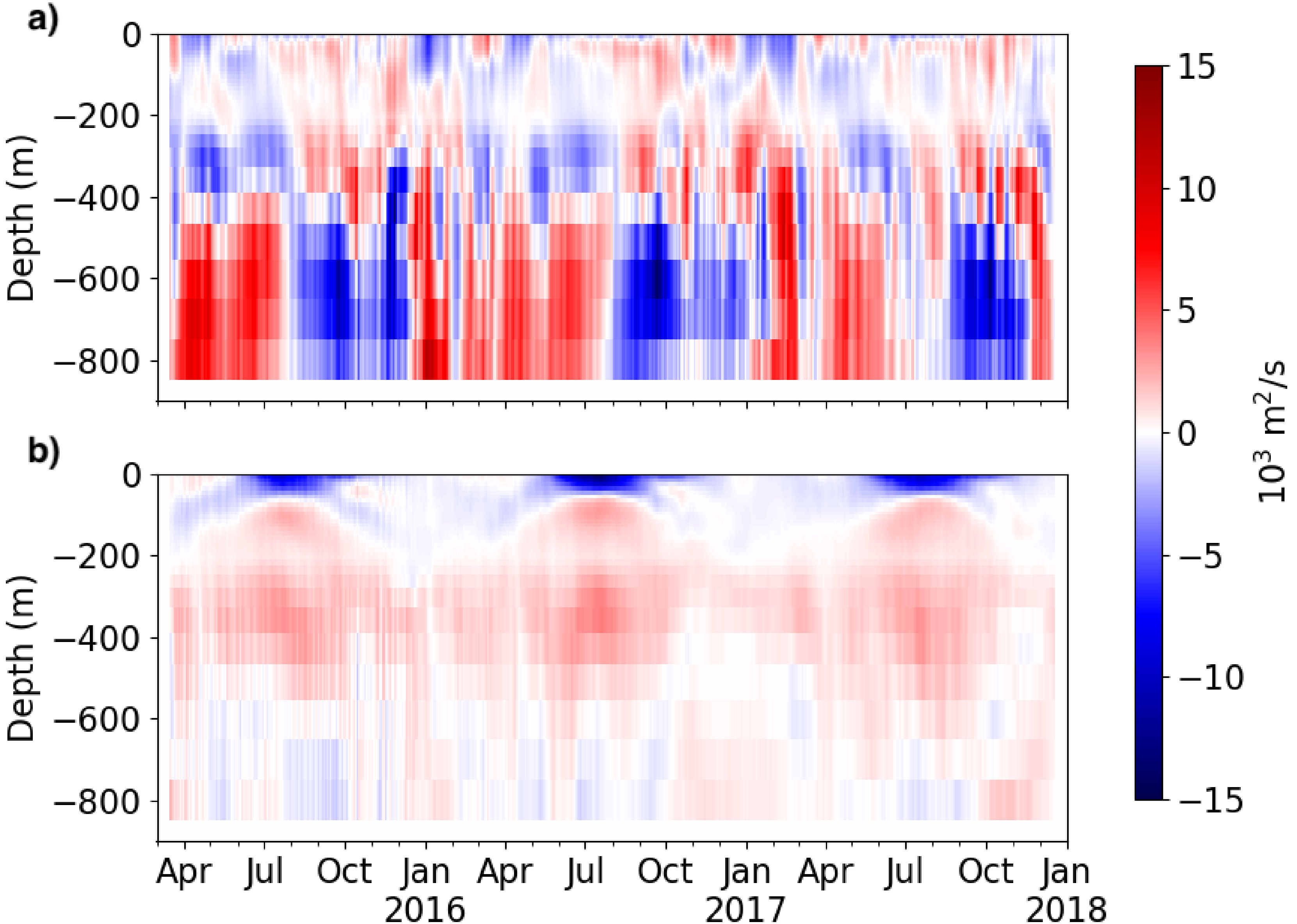
a)
b)
0
−200
−400
−600
−800
Depth (m)
Apr
Jul
Oct
Jan
2016
2017
2018
15
10
5
0
−5
−10
−15
10^3 m^2/s

Figure 12.

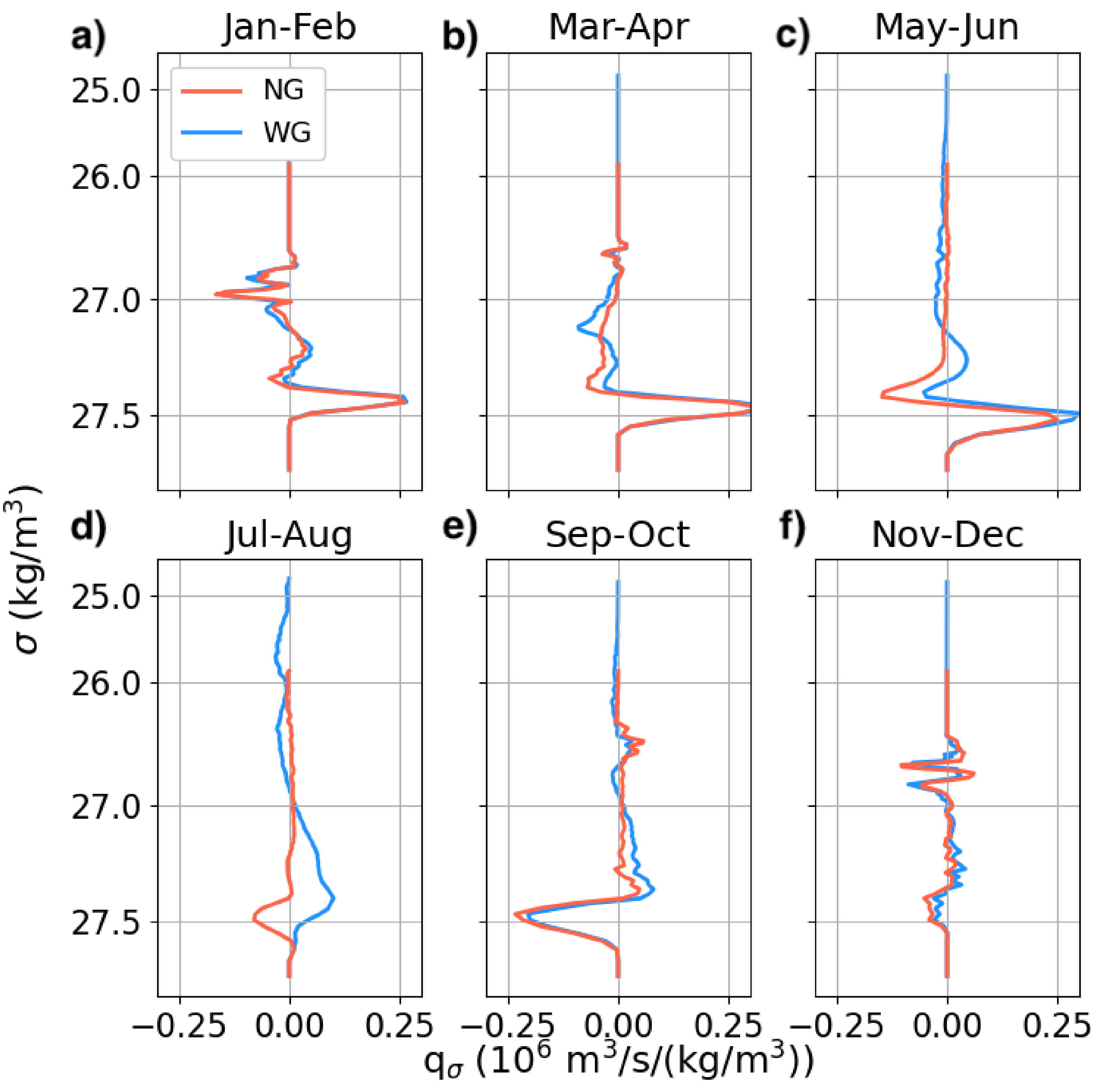

a)
Jan-Feb
b)
Mar-Apr
c)
May-Jun
d)
Jul-Aug
e)
Sep-Oct
f)
Nov-Dec
NG
WG
25.0
26.0
27.0
27.5
σ (kg/m³)
−0.25
0.00
0.25
q_σ (10⁶ m³/s/(kg/m³))

Figure 13.

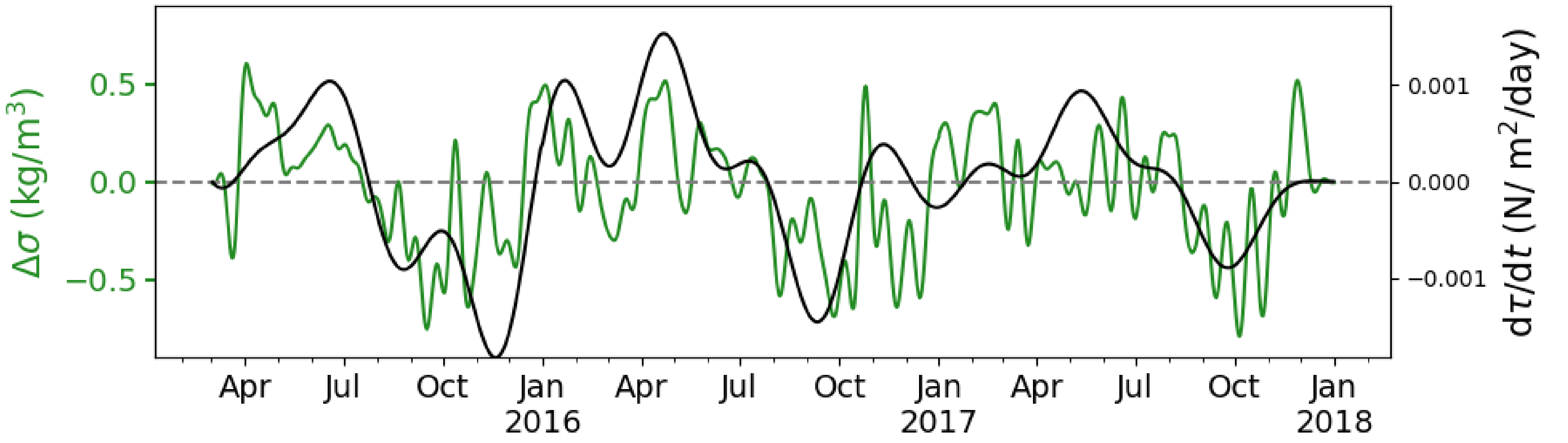

Δσ (kg/m³)
0.5
0.0
−0.5
dτ/dt (N/ m²/day)
0.001
0.000
−0.001
Apr
Jul
Oct
Jan
2016
Apr
Jul
Oct
Jan
2017
Apr
Jul
Oct
Jan
2018

Figure 14.

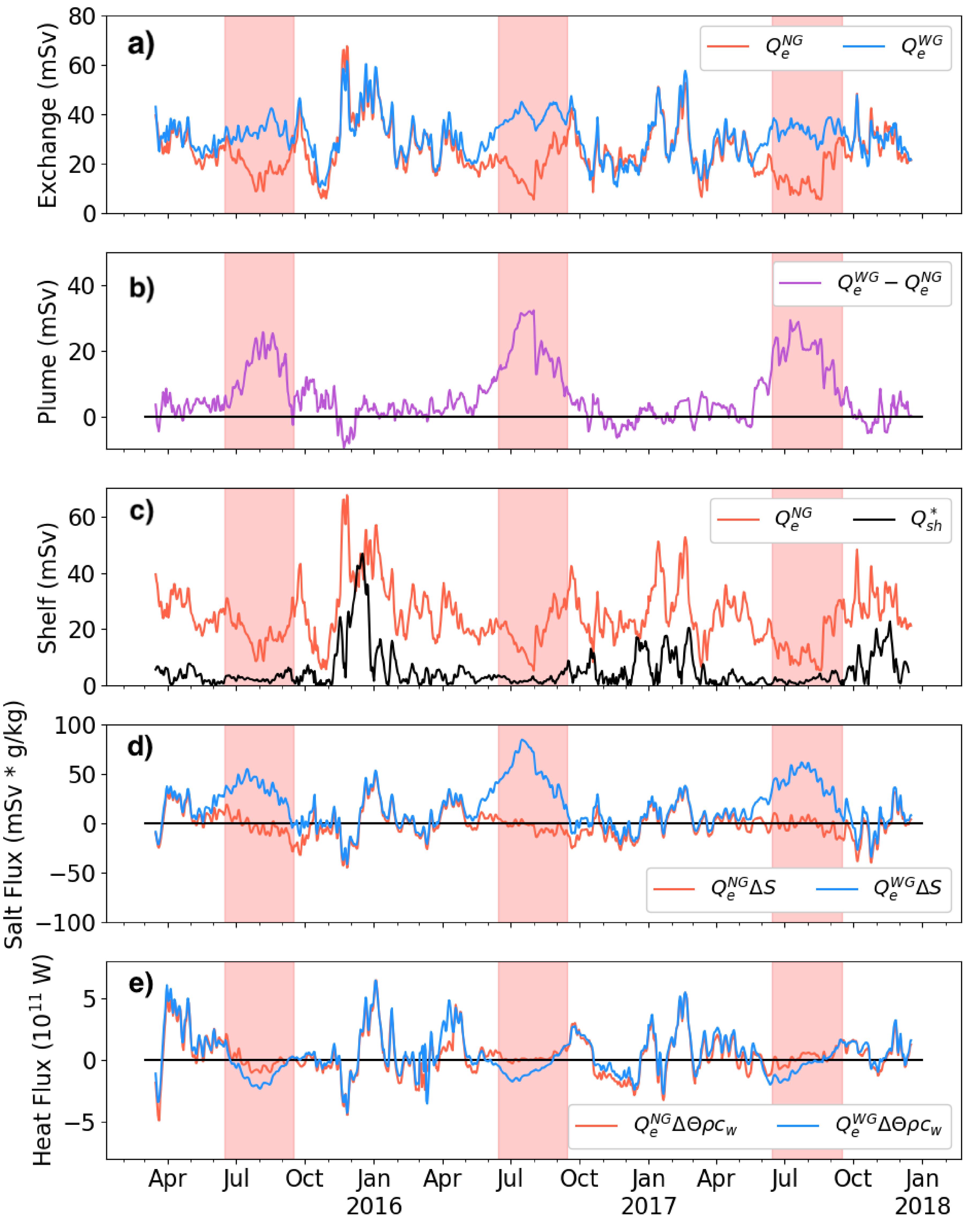

a)
Exchange (mSv)
Q_e^{NG}
Q_e^{WG}
b)
Plume (mSv)
$Q_e^{WG} - Q_e^{NG}$
c)
Shelf (mSv)
Q_e^{NG}
Q_{sh}^{*}
d)
Salt Flux (mSv * g/kg)
$Q_e^{NG}\Delta S$
$Q_e^{WG}\Delta S$
e)
Heat Flux (10^{11} W)
$Q_e^{NG}\Delta\Theta\rho c_w$
$Q_e^{WG}\Delta\Theta\rho c_w$
Apr Jul Oct Jan Apr Jul Oct Jan Apr Jul Oct Jan
2016
2017
2018

Figure 15.

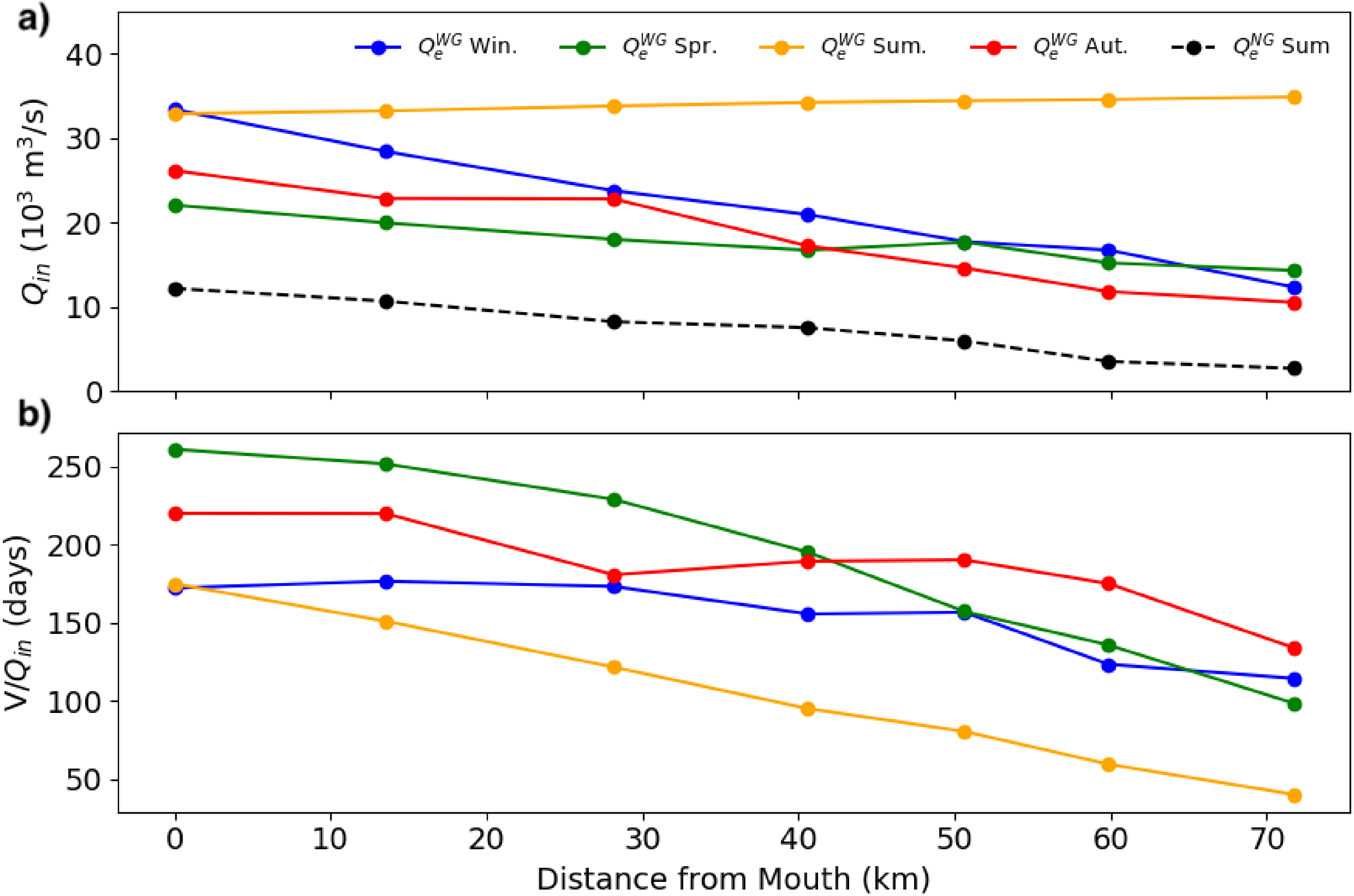
a)
Q_e^{WG} Win.
Q_e^{WG} Spr.
Q_e^{WG} Sum.
Q_e^{WG} Aut.
Q_e^{NG} Sum
Q_{in} (10^3 m^3/s)
0
10
20
30
40
b)
V/Q_{in} (days)
50
100
150
200
250
0
10
20
30
40
50
60
70
Distance from Mouth (km)

Appendix Figure 1.

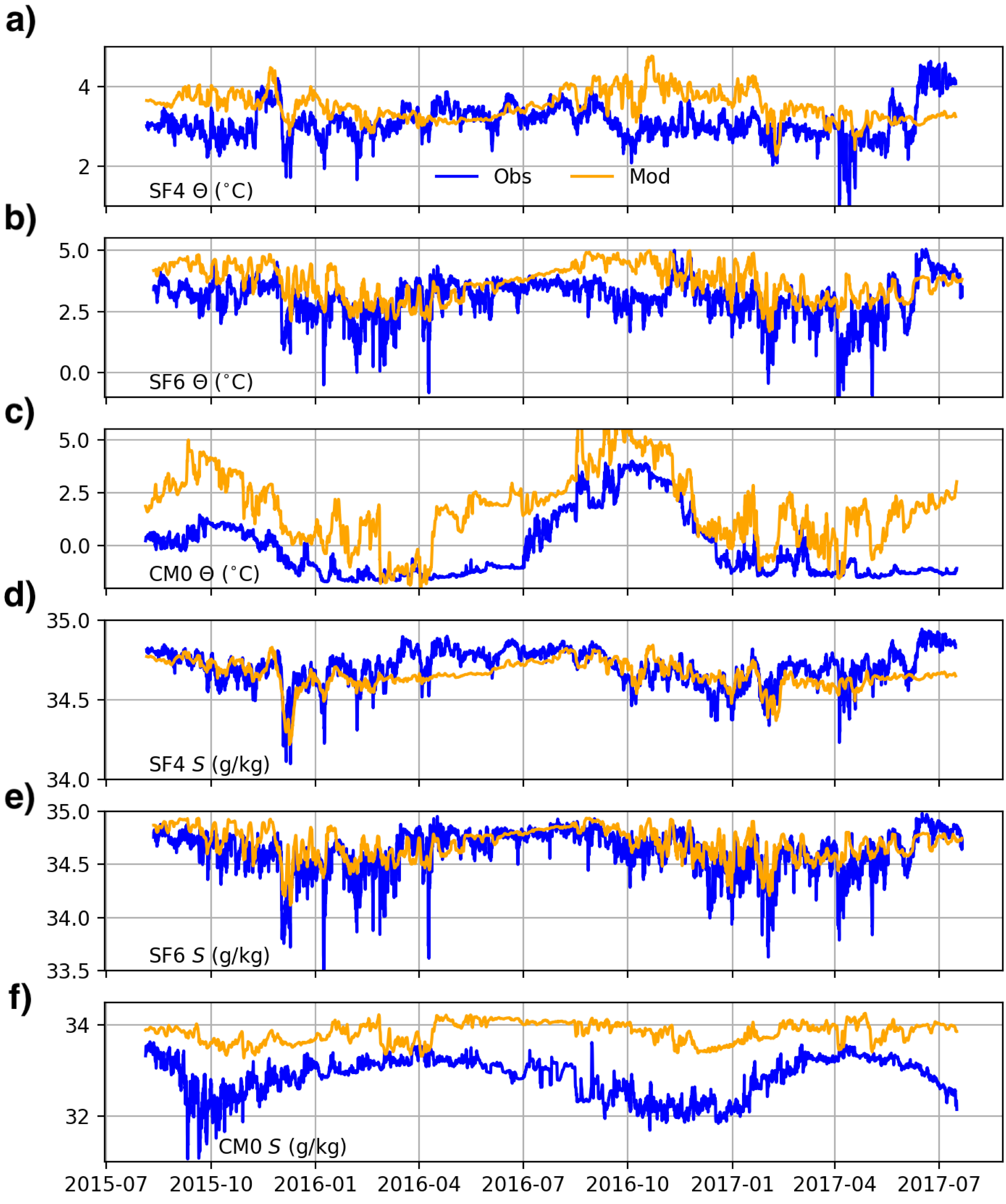

a)
b)
c)
d)
e)
f)
SF4 Θ (°C)
Obs
Mod
SF6 Θ (°C)
CM0 Θ (°C)
SF4 S (g/kg)
SF6 S (g/kg)
CM0 S (g/kg)
4
2
5.0
2.5
0.0
35.0
34.5
34.0
33.5
34
32
2015-07
2015-10
2016-01
2016-04
2016-07
2016-10
2017-01
2017-04
2017-07

Supporting Information for "Relative roles of plume and coastal forcing on exchange flow variability of a glacial fjord"

Robert Sanchez[1], Fiammetta Straneo[1], Kenneth Hughes[2], Philip Barbour[2],

Emily Shroyer[2,3]

[1]Scripps Institution of Oceanography, UC San Diego, San Diego, CA, USA

[2]College of Earth, Ocean, and Atmospheric Sciences, Oregon State University, Corvallis, OR, USA

[3]Office of Naval Research

Contents of this file

1. Text S1 to S3
2. Figures S1 to S9
3. Tables S1

Text S1. Comparison against Profiles.

We compare the model output to CTD profiles collected in August 2015 and July 2017 and categorize the profiles as shelf (N=24) and fjord (N=48) profiles. Figure 2 of the main text shows all the profiles collected in summer. When all profiles are averaged together, we see the model (solid, Fig. S1a) does a reasonable job of capturing the observed (dashed, Fig S1a) mean temperature at depth. However, this mean is expected to be captured because the ASTE boundary conditions were shifted to be in line with the observations at 350 m. It also recreates the basic vertical structure of temperature with a warm AW mass at depth, a cold PW mass around 100 m, and a WPW mass near the surface. We also include the average of XCTD profiles taken in March 2010 and compare it to the mean model output at SF4 in March 2016. The winter profiles are from a different year and so a direct comparison is limited, but the model pycnocline appears significantly shallower than in observations and is generally saltier. Unfortunately, in all seasons, the model overestimates the temperature of the PW resulting in a warm bias. Reasons for this bias potentially include the lack of icebergs in the fjord, lack of sea ice along the coast and a warm bias from the ASTE boundary conditions. The model also overestimates the salinity above 300 m resulting in weaker stratification in the model than in reality (Fig. S1b). In both the temperature and salinity fields, the differences between the model and observations are much larger than the differences between the fjord and the shelf.

Velocity and volume transport from the model are compared to ADCP data from the middle of fjord (SF4) and the shelf (OW1). At SF4, we break the velocity record into a summer (June 1 – August 31) and winter (October 1 – May 1) time series similar to Jackson and Straneo (2016). The seasonal mean (from two years) along-fjord velocity structure from the observations compares poorly to the model output (Sup. Fig. S1c,d) due to the challenges in recreating realistic fjord stratification. During the summer, the model outflow is at the surface while the observations show outlfow centered around 100 m. This mismatch can largely be explained by plume dynamics as the model stratification is much weaker than the observations (Sup. Fig. S1b) resulting in a plume that reaches close to the surface rather than finding a deeper neutral buoyancy (De Andrés et al., 2020). The primary inflow which compensates the outflow is therefore also shallower in the model.

Kajanto, Straneo, and Nisancioglu (2022) showed that with icebergs the stratification increased and the plume was deeper. Additionally, iceberg drag might contribute to a deeper neutral buoyancy depth. In the winter, the profiles also have a mismatch that can potentially be explained by fjord stratification. In the observations, the fjord has a sharp pycnocline around 200 m (sup. Fig. S1b) while the model lacks this pycnocline. This difference in pycnocline structure and depth results in a concentrated baroclinic flow centered around 200 m in the observations and a diffuse baroclinic flow centered closer to 350 m in the model.

Text S2. ADCP Transport.

We estimate volume transport from the ADCP using 3 methods of extrapolation: surface extrapolation using constant shear from the top three bins, surface extrapolation using a constant value, and bottom extrapolation using a linear shear down to zero (Jackson & Straneo, 2016). For each method, the part of the water column not extrapolated is filled with a constant value to ensure no net transport. We multiply this velocity profile by the fjord width and use two different estimates of fjord width resulting in 6 transport estimates that we use to define uncertainty. We apply a 30-day rolling mean to velocities prior to calculating incoming volume transport. The ADCP-derived incoming volume transport is the same magnitude as the modeled transport, but has a larger volume flux during the summer than the model and a smaller flux in the winter (Sup. Fig. S2). While the instantaneous velocities in the winter can be much higher than in the summer, averaging removes most of the oscillatory signal resulting in weaker average velocities (Sup. Fig. S1).

We also compare the 30-day rolling mean model velocity in the western end of Sermilik Trough with the 30-day rolling mean velocity recorded at OW1 focusing on the depth 120 m where data was cleanest (Sup. Fig. S2). The along-shelf modeled velocity was significantly larger than the observed velocity reaching velocities around 0.3 m/s in the model compared to 0.1 m/s by the ADCP. However, both are flowing westward with a mean negative velocity, consistent with the presence of an equatorward coastal current, and both are minimized in the summer when winds and coastal current freshening are weakest. It could be that the disagreement is poor because the mooring with the ADCP is located on a slightly different part of the shelf than where we sample in the model. Additionally, if we are not recreating the position of the coastal current correctly it could result in a large difference between the observed and modeled velocity.

Text S3. Discussion of CTW parameters.

A majority of the parameters used in the CTW Eq. 3 of the main text are straightforward to determine, but the baroclinic wave speed c and the pycnocline amplitude η both require user discretion. c is calculated as the zero-crossing of the first normal mode using density profiles from the mouth of the fjord, but it varies across the mouth by ± 0.15 m/s and the depth of the of the pycnocline can vary as well between ± 60 m at a single timestep. We use cross-section averages to determine c as most of this variability is due to differences in fjord depth which can lower the pycnocline height.

We used two different methods to determine η. The first was simply to the take the depth of the pycnocline determined from the normal-mode analysis and then remove the mean. The second method, described in the main text, used the cross-section average density fluctuations divided by the stratification. Both methods produced similar amplitudes on timescales longer than 15-days (Fig. S8), but the method based on stratification produced a larger response on shorter timescales. We believe the normal-mode method, while useful for determining the pycnocline depth, might underestimate pycnocline fluctuations on shorter timescales since it responds to rapid changes in density structure by finding a new zero crossing rather than tracking the previous pycnocline as it fluctuates.

We evaluate how much CTWs contribute to the high-frequency variability by comparing the estimate from CTW theory against a 15-day high-pass filter of incoming volume flux (Fig. S9). The seasonality of the two volume fluxes are consistent with peaks in winter months and are a similar magnitude. However, there is still substantial higher-frequency variability in the summer in the model and we cannot attribute much of this to CTWs. The standard deviation of the model is 46 mSv and of the theory is 30 mSv. Therefore, we can say that CTW theory is either underestimating the magnitude of the circulation or additional high-frequency variability is a significant component of the incoming volume flux. Model animations (not shown) suggest eddies could potentially play a role.

References

De Andrés, E., Slater, D. A., Straneo, F., Otero, J., Das, S., & Navarro, F. (2020). Surface emergence of glacial plumes determined by fjord stratification. *Cryosphere Discuss.*, 1–41. doi: 10.5194/tc-2019-264

Jackson, R. H., & Straneo, F. (2016). Heat, Salt, and Freshwater Budgets for a Glacial Fjord in Greenland. *J. Phys. Oceanogr.*, *46*, 2735–2768. doi: 10.1175/JPO-D-15-0134.1

Kajanto, K., Straneo, F., & Nisancioglu, K. (2022). Impact of icebergs on the seasonal submarine melt of Sermeq Kujalleq. *The Cryosphere Discuss.*, 1-26. doi: 10.5194/tc-2022-136

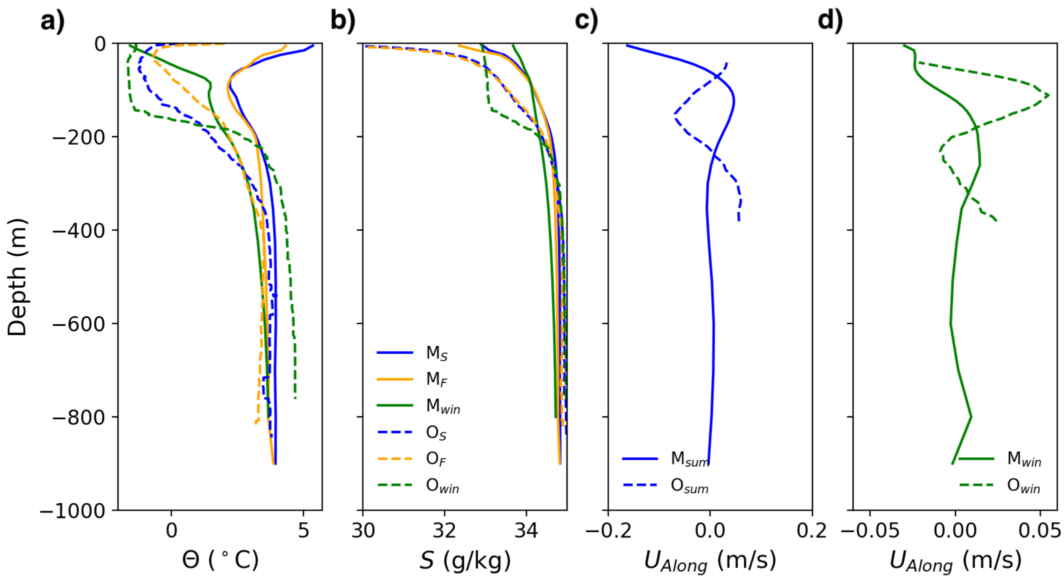

Figure S1. Profile comparison of model and observations. a) the spatially-averaged CTD temperature profiles versus depth for both the model (solid) and observations (dashed) in the fjord (yellow, N=48), on the shelf (blue, N=24), and in the winter (green, N=4). b) same but for absolute salinity. c) The average along-fjord velocity at SF4 during the summer (June 1 – August 31). The solid line is the model and the dashed line comes from the SF4 ADCP. d) same as c but for the winter (October 1 – May 1.)

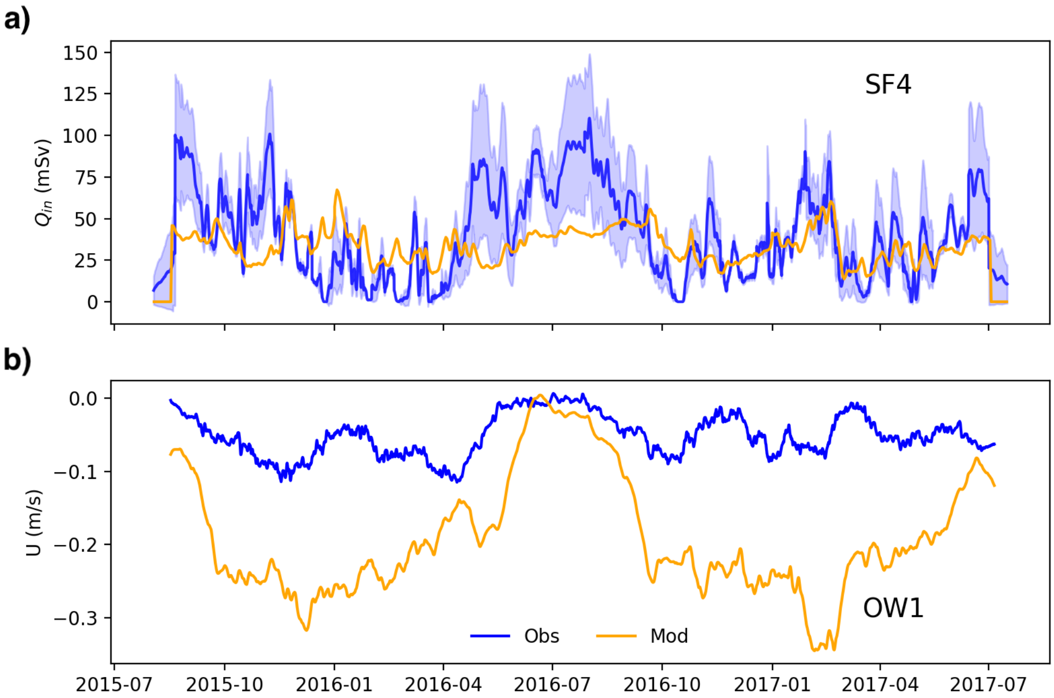

Figure S2. Velocity comparison of model and observations. a) The incoming volume transport calculated from the ADCP at SF4 (blue) and model output (orange). b) The along-shelf velocity averaged over 110 – 130 m from the ADCP at SF6 and the model. All velocities have had a 30-day rolling mean applied.

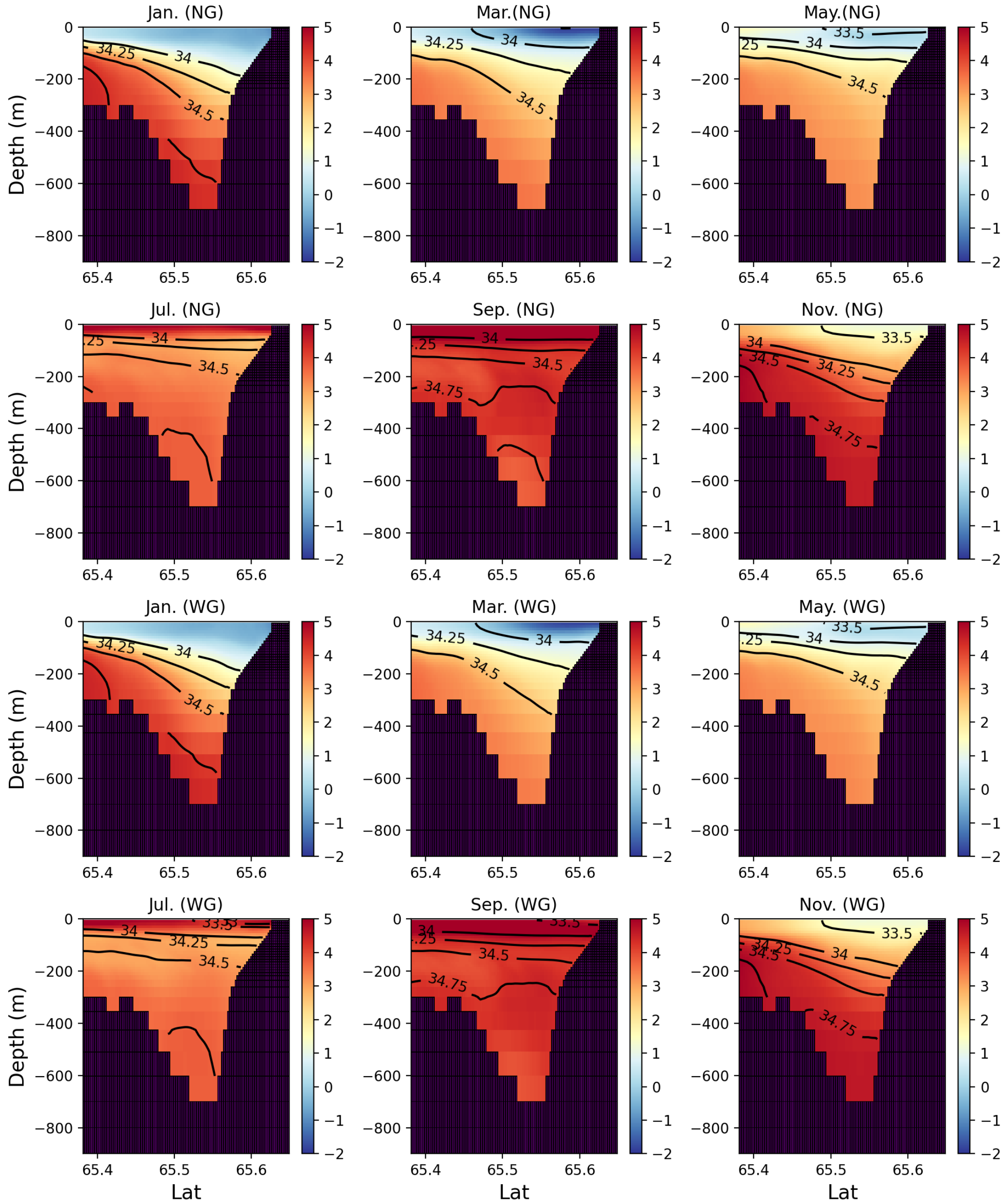

Figure S3. Monthly-average shelf temperature transect downstream (west) of the fjord. Contours are isohalines (32,32.5,33,33.5,34,34.25, 34.5,34.75,35) g/kg. The top six panels are from the NG run, the bottom six are from the WG run.

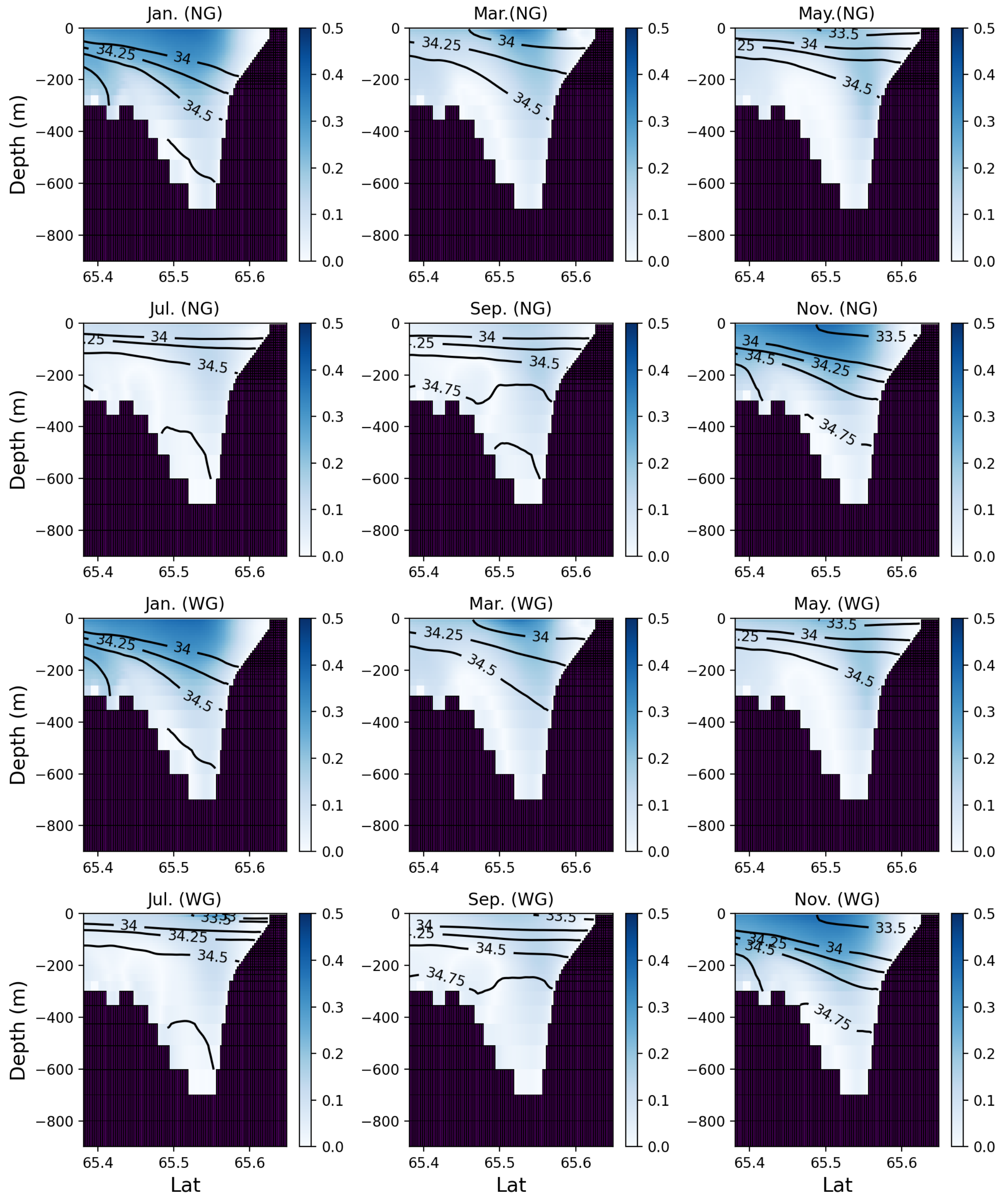

Figure S4. Monthly-average shelf velocity transect downstream (west) of the fjord. Positive velocity is oriented west. Contours are isohalines (32,32.5,33,33.5,34,34.25, 34.5,34.75,35) g/kg. The top six panels are from the NG run, the bottom six are from the WG run.

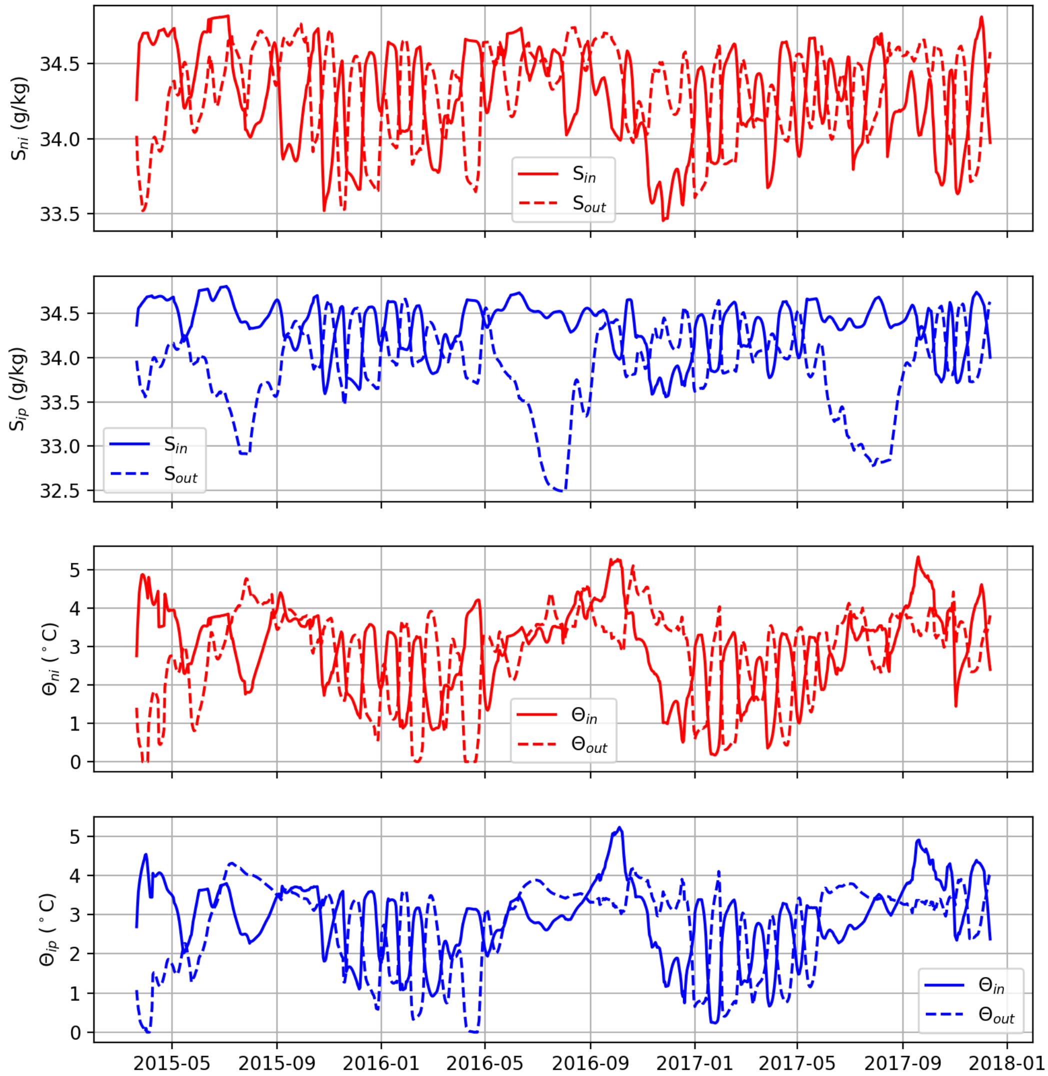

Figure S5. Additional Time Series of TEF bulk values. a) The TEF Salinity time series for the NG run. b) The TEF Salinity time series for the WG run. c) The TEF temperature time series for the NG Run. d) The TEF temperature series for the WG run. These values were used in the calculation of ΔS and $\Delta\Theta$ in Fig. 14 main text

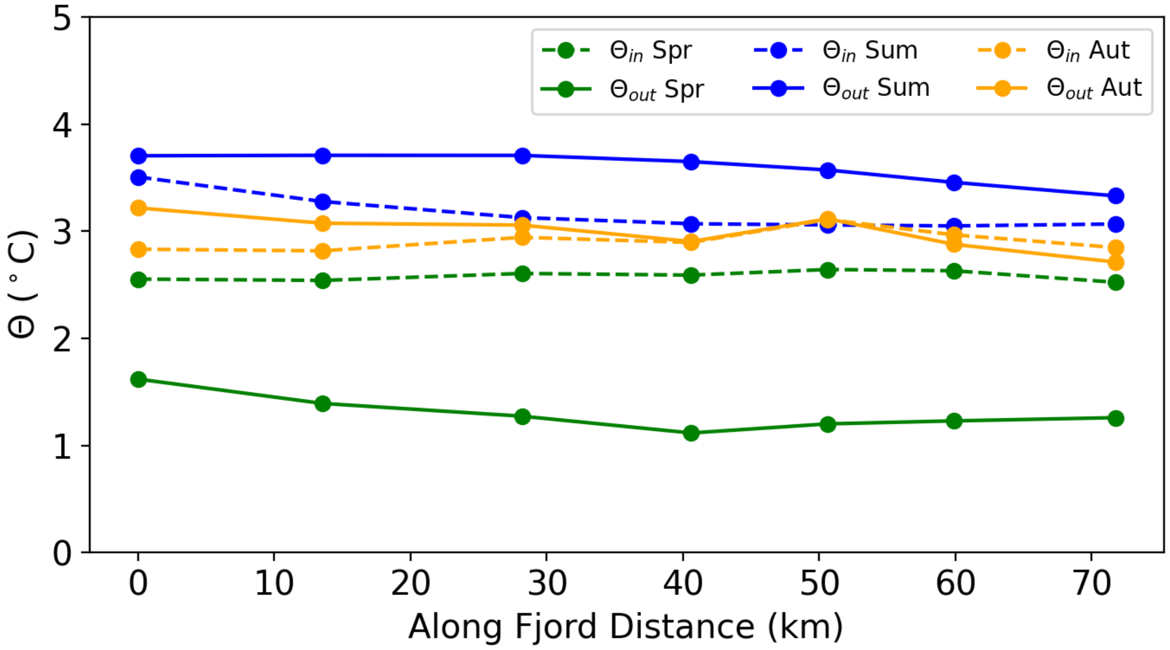

Figure S6. **TEF along fjord** Θ_{in}. Seasons are three month averages. The x-axis is distance from the mouth. Compare to Fig. 15 main text

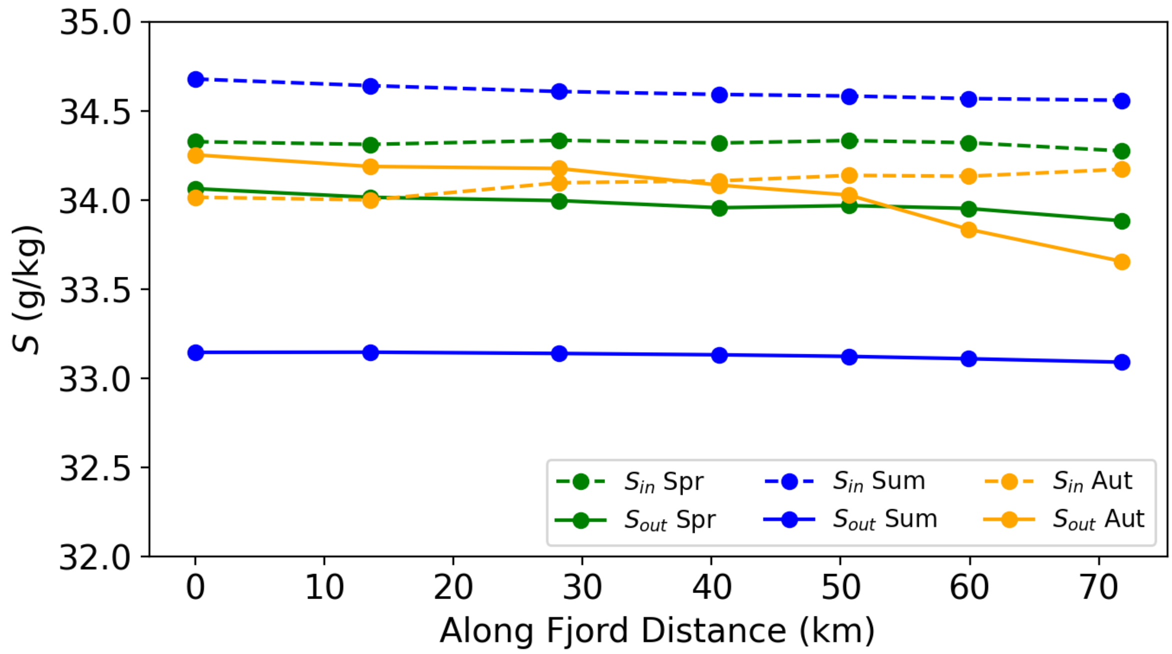

Figure S7. TEF along fjord S_{in}. Seasons are three month averages. The x-axis is distance from the mouth. Compare to Fig. 15 main text

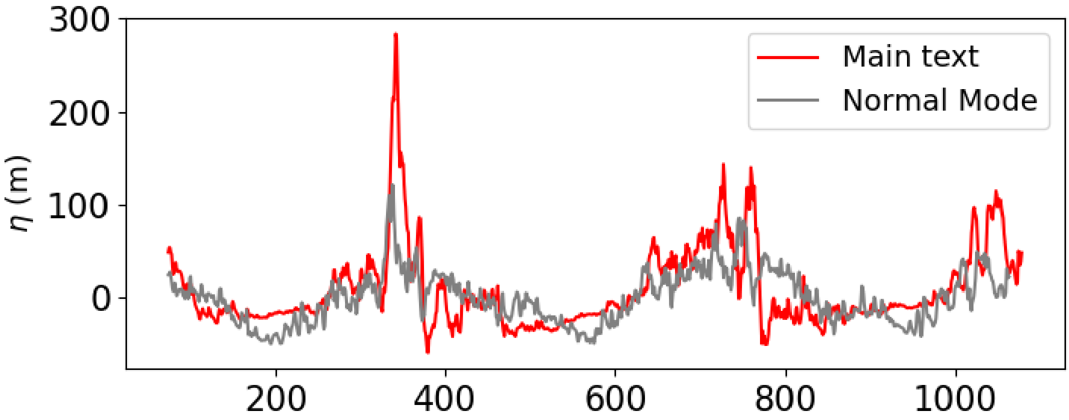

Figure S8. Comparison of the pycnocline amplitude based on different methods. The pycnocline amplitude based on the normal mode method (gray) and the method used in the main text (red). The main text method is the density anomaly divided by the mean stratification.

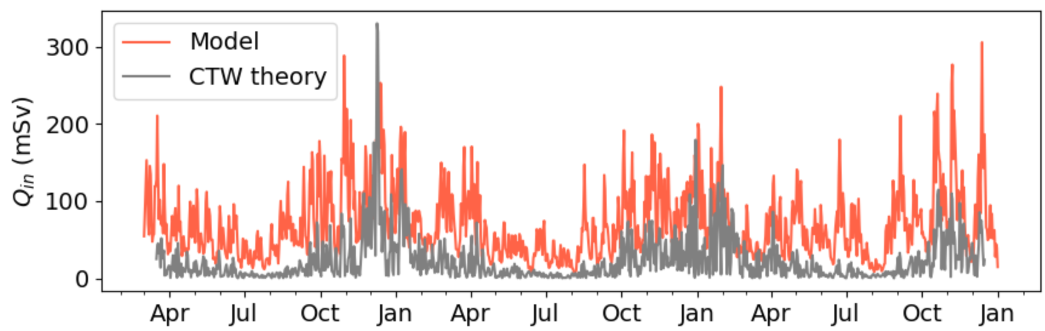

Figure S9. Incoming volume flux comparison against theory. The incoming volume flux from the model (red) and the predicted flux from CTW theory (gray). The incoming flux has been high-pass filtered to 15 days.

Table S1. Statistics and skill scores for the summer CTD data. The first column is the variable and includes the model skill in vertically-averaged salinity and temperature ($\overline{S}, \overline{\Theta}$), and the skill for the model and observations for the vertical stratification (N_S, N_Θ). Significance is denoted with a star. A skill score < 0.2 is considered poor.

Variable	SS	MSE	r
$\overline{S}$	0.26	0.49	0.97*
$\overline{\Theta}$	< 0	4.1	-0.13
N_S	< 0	0.93	0.65*
N_Θ	< 0	11.23	-0.08